ACOUSTIC CORRELATION SPECTROSCOPY OF STRONGLY SCATTERING MEDIA

BY

IAN P. JONES

A Thesis
Submitted to the Faculty of Graduate Studies
in Partial Fulfillment of the Requirements
for the degree of

MASTER OF SCIENCE

Department of Physics
University of Manitoba
Winnipeg Manitoba

© copyright by Ian P. Jones, July 1996

National Library
of Canada

Acquisitions and
Bibliographic Services Branch

395 Wellington Street
Ottawa, Ontario
K1A 0N4

Bibliothèque nationale
du Canada

Direction des acquisitions et
des services bibliographiques

395, rue Wellington
Ottawa (Ontario)
K1A 0N4

Your file *Votre référence*

Our file *Notre référence*

The author has granted an irrevocable non-exclusive licence allowing the National Library of Canada to reproduce, loan, distribute or sell copies of his/her thesis by any means and in any form or format, making this thesis available to interested persons.

L'auteur a accordé une licence irrévocable et non exclusive permettant à la Bibliothèque nationale du Canada de reproduire, prêter, distribuer ou vendre des copies de sa thèse de quelque manière et sous quelque forme que ce soit pour mettre des exemplaires de cette thèse à la disposition des personnes intéressées.

The author retains ownership of the copyright in his/her thesis. Neither the thesis nor substantial extracts from it may be printed or otherwise reproduced without his/her permission.

L'auteur conserve la propriété du droit d'auteur qui protège sa thèse. Ni la thèse ni des extraits substantiels de celle-ci ne doivent être imprimés ou autrement reproduits sans son autorisation.

ISBN 0-612-16174-9

Canada

Name _____

Dissertation Abstracts International and *Masters Abstracts International* are arranged by broad, general subject categories. Please select the one subject which most nearly describes the content of your dissertation or thesis. Enter the corresponding four-digit code in the spaces provided.

Acoustics
SUBJECT TERM

0986
SUBJECT CODE

UMI

Subject Categories

THE HUMANITIES AND SOCIAL SCIENCES

COMMUNICATIONS AND THE ARTS
Architecture 0729
Art History 0377
Cinema 0900
Dance 0378
Fine Arts 0357
Information Science 0723
Journalism 0391
Library Science 0399
Mass Communications 0708
Music 0413
Speech Communication 0459
Theater 0465

EDUCATION
General 0515
Administration 0514
Adult and Continuing 0516
Agricultural 0517
Art 0273
Bilingual and Multicultural 0282
Business 0688
Community College 0275
Curriculum and Instruction 0727
Early Childhood 0518
Elementary 0524
Finance 0277
Guidance and Counseling 0519
Health 0680
Higher 0745
History of 0520
Home Economics 0278
Industrial 0521
Language and Literature 0279
Mathematics 0280
Music 0522
Philosophy of 0998
Physical 0523
Psychology 0525
Reading 0535
Religious 0527
Sciences 0714
Secondary 0533
Social Sciences 0534
Sociology of 0340
Special 0529
Teacher Training 0530
Technology 0710
Tests and Measurements 0288
Vocational 0747

LANGUAGE, LITERATURE AND LINGUISTICS
Language
- General 0679
- Ancient 0289
- Linguistics 0290
- Modern 0291

Literature
- General 0401
- Classical 0294
- Comparative 0295
- Medieval 0297
- Modern 0298
- African 0316
- American 0591
- Asian 0305
- Canadian (English) 0352
- Canadian (French) 0355
- English 0593
- Germanic 0311
- Latin American 0312
- Middle Eastern 0315
- Romance 0313
- Slavic and East European 0314

PHILOSOPHY, RELIGION AND THEOLOGY
Philosophy 0422
Religion
- General 0318
- Biblical Studies 0321
- Clergy 0319
- History of 0320
- Philosophy of 0322

Theology 0469

SOCIAL SCIENCES
American Studies 0323
Anthropology
- Archaeology 0324
- Cultural 0326
- Physical 0327

Business Administration
- General 0310
- Accounting 0272
- Banking 0770
- Management 0454
- Marketing 0338

Canadian Studies 0385
Economics
- General 0501
- Agricultural 0503
- Commerce-Business 0505
- Finance 0508
- History 0509
- Labor 0510
- Theory 0511

Folklore 0358
Geography 0366
Gerontology 0351
History
- General 0578
- Ancient 0579
- Medieval 0581
- Modern 0582
- Black 0328
- African 0331
- Asia, Australia and Oceania 0332
- Canadian 0334
- European 0335
- Latin American 0336
- Middle Eastern 0333
- United States 0337

History of Science 0585
Law 0398
Political Science
- General 0615
- International Law and Relations 0616
- Public Administration 0617

Recreation 0814
Social Work 0452
Sociology
- General 0626
- Criminology and Penology ... 0627
- Demography 0938
- Ethnic and Racial Studies 0631
- Individual and Family Studies 0628
- Industrial and Labor Relations 0629
- Public and Social Welfare 0630
- Social Structure and Development 0700
- Theory and Methods 0344

Transportation 0709
Urban and Regional Planning 0999
Women's Studies 0453

THE SCIENCES AND ENGINEERING

BIOLOGICAL SCIENCES
Agriculture
- General 0473
- Agronomy 0285
- Animal Culture and Nutrition 0475
- Animal Pathology 0476
- Food Science and Technology 0359
- Forestry and Wildlife 0478
- Plant Culture 0479
- Plant Pathology 0480
- Plant Physiology 0817
- Range Management 0777
- Wood Technology 0746

Biology
- General 0306
- Anatomy 0287
- Biostatistics 0308
- Botany 0309
- Cell 0379
- Ecology 0329
- Entomology 0353
- Genetics 0369
- Limnology 0793
- Microbiology 0410
- Molecular 0307
- Neuroscience 0317
- Oceanography 0416
- Physiology 0433
- Radiation 0821
- Veterinary Science 0778
- Zoology 0472

Biophysics
- General 0786
- Medical 0760

EARTH SCIENCES
Biogeochemistry 0425
Geochemistry 0996
Geodesy 0370
Geology 0372
Geophysics 0373
Hydrology 0388
Mineralogy 0411
Paleobotany 0345
Paleoecology 0426
Paleontology 0418
Paleozoology 0985
Palynology 0427
Physical Geography 0368
Physical Oceanography 0415

HEALTH AND ENVIRONMENTAL SCIENCES
Environmental Sciences 0768
Health Sciences
- General 0566
- Audiology 0300
- Chemotherapy 0992
- Dentistry 0567
- Education 0350
- Hospital Management 0769
- Human Development 0758
- Immunology 0982
- Medicine and Surgery 0564
- Mental Health 0347
- Nursing 0569
- Nutrition 0570
- Obstetrics and Gynecology .. 0380
- Occupational Health and Therapy 0354
- Ophthalmology 0381
- Pathology 0571
- Pharmacology 0419
- Pharmacy 0572
- Physical Therapy 0382
- Public Health 0573
- Radiology 0574
- Recreation 0575
- Speech Pathology 0460
- Toxicology 0383

Home Economics 0386

PHYSICAL SCIENCES
Pure Sciences
Chemistry
- General 0485
- Agricultural 0749
- Analytical 0486
- Biochemistry 0487
- Inorganic 0488
- Nuclear 0738
- Organic 0490
- Pharmaceutical 0491
- Physical 0494
- Polymer 0495
- Radiation 0754

Mathematics 0405
Physics
- General 0605
- Acoustics 0986
- Astronomy and Astrophysics 0606
- Atmospheric Science 0608
- Atomic 0748
- Electronics and Electricity 0607
- Elementary Particles and High Energy 0798
- Fluid and Plasma 0759
- Molecular 0609
- Nuclear 0610
- Optics 0752
- Radiation 0756
- Solid State 0611

Statistics 0463

Applied Sciences
Applied Mechanics 0346
Computer Science 0984
Engineering
- General 0537
- Aerospace 0538
- Agricultural 0539
- Automotive 0540
- Biomedical 0541
- Chemical 0542
- Civil 0543
- Electronics and Electrical 0544
- Heat and Thermodynamics ... 0348
- Hydraulic 0545
- Industrial 0546
- Marine 0547
- Materials Science 0794
- Mechanical 0548
- Metallurgy 0743
- Mining 0551
- Nuclear 0552
- Packaging 0549
- Petroleum 0765
- Sanitary and Municipal 0554
- System Science 0790

Geotechnology 0428
Operations Research 0796
Plastics Technology 0795
Textile Technology 0994

PSYCHOLOGY
General 0621
Behavioral 0384
Clinical 0622
Developmental 0620
Experimental 0623
Industrial 0624
Personality 0625
Physiological 0989
Psychobiology 0349
Psychometrics 0632
Social 0451

THE UNIVERSITY OF MANITOBA

FACULTY OF GRADUATE STUDIES

COPYRIGHT PERMISSION

ACOUSTIC CORRELATION SPECTROSCOPY OF STRONGLY SCATTERING MEDIA

BY

IAN P. JONES

A Thesis/Practicum submitted to the Faculty of Graduate Studies of the University of Manitoba in partial fulfillment of the requirements for the degree of

MASTER OF SCIENCE

Ian P. Jones © 1996

Permission has been granted to the LIBRARY OF THE UNIVERSITY OF MANITOBA to lend or sell copies of this thesis/practicum, to the NATIONAL LIBRARY OF CANADA to microfilm this thesis/practicum and to lend or sell copies of the film, and to UNIVERSITY MICROFILMS INC. to publish an abstract of this thesis/practicum..

This reproduction or copy of this thesis has been made available by authority of the copyright owner solely for the purpose of private study and research, and may only be reproduced and copied as permitted by copyright laws or with express written authorization from the copyright owner.

Abstract

This thesis describes the use of correlation spectroscopy to study the propagation of sound though strongly scattering materials, and demonstrates the feasibility of a novel acoustic probe for studying the dynamics of such materials. Although extensively used in light scattering, the measurement and use of correlation functions in acoustic experiments has generally been overlooked, and has not been applied to materials in which the acoustic waves are scattered many times within the medium. We use this approach to investigate some fundamental issues of how sound propagates through this type of material and to show how dynamic information in the material can be measured in the presence of strong multiple scattering even though traditional acoustic imaging is no longer possible.

We first report our measurements and analysis of frequency correlations, which is a powerful method used to understand multiple scattering and diffusion in strongly disordered media. A new method is described for measuring the frequency correlation function that exploits the ability of sound scattering experiments to measure both the amplitude and phase of the detected signals. Comparison of our data with theory gives new information on the evolution from ballistic to diffusive propagation in strongly scattering media and gives additional information on the fundamental parameters that describe the diffusive transport of sound.

Next we study spatial correlations in strongly scattering media. We measure the average speckle size in the near field and confirm the validity of our experimental technique for accurately measuring the scattered sound field at ultrasonic frequencies.

Finally, we describe the development of a new ultrasonic technique, which we call Diffusing Acoustic Wave Spectroscopy, for probing the dynamics of particulate suspensions that scatter acoustic waves very strongly. By exploiting the diffusion approximation to describe the propagation of the multiply scattered sound, as is done in the analogous optical technique of Diffusing Wave Spectroscopy, the motion of the scattering particles is determined from the autocorrelation function of the temporal fluctuations of the scattered ultrasonic waves. We have used this technique to measure the temporal evolution of the mean square displacement of glass beads suspended in a fluidized bed.

ACKNOWLEDGMENTS

This work would not have been accomplished without the unending help, support, and patience of many people.

I would like to thank my wife Marion Frantz for the love and support that kept me focused. I would also thank Professor John Page for showing infinite amounts of patience and for supplying the help and knowledge that allowed me to begin, write, and complete this thesis. A large debt of gratitude is owed to Gilles Roy, whose unique method of solving problems allowed the experiments to be carried out as quickly and efficiently as possible. Lastly, thanks go to Scott Elson, Brian Eves, and Andrea Sklaruk for putting up with me.

TABLE OF CONTENTS

List of Figures vi

1. Introduction 1

1.1 History 1

1.2 Background 2

1.3 Outline of Thesis 5

1.4 References 7

2. Theory 8

2.1 Frequency Correlation Functions 9

2.1.1 Plane Wave Correlation Function 9
2.1.2 Point Source Correlation Function 17

2.2 Spatial Correlation Function 18

2.2.1 First-Order Statistics 18
2.2.2 Second-Order Statistics 19

2.3 Temporal Autocorrelation Function 23

2.3.1 Stochastic Motion 29
2.3.2 Deterministic Motion 29

2.4 References 31

3. Apparatus and Procedure 33

3.1 Frequency Correlation Study 34

3.1.1 Aquarium 36
3.1.2 Transducers 39
3.1.3 Hydrophone 43
3.1.4 Sample Preparation 44
3.1.5 Translation Stages 46
3.1.6 Matec 6600 rf Pulse Generator 47
3.1.7 Oscilloscope 47
3.1.8 Stanford Delay Generator 48
3.1.9 Filters 48

3.2 Spatial Correlation Study 49

3.3 Temporal Autocorrelation Study (DAWS) 50

3.3.1 Acquisition Methods 51
3.3.2 Overview of Apparatus 52
3.3.3 Fluidized Bed 55
3.3.4 Aquarium 59
3.3.5 Boxcar Integrator 60
3.3.6 Oscilloscope 61

3.4 References 62

4. Experimental Data and Analysis 63

4.1 Frequency Correlation Study 64

4.1.1 Point Source Geometry 70
4.1.2 Plane Wave Geometry 78

4.2 Spatial Correlation Study 93

4.2.1 Background 93
4.2.2 Measurements and Analysis 108

4.3 Temporal Autocorrelation Study 109

4.3.1 Full Waveform Measurements 125
4.3.2 Boxcar Integrator 156
4.3.3 Continuous Wave 159
4.3.4 Comparison of Acquisition Methods 161

4.2 References 162

5. Conclusions 162

5.1 Frequency Correlation Study 162

5.2 Spatial Correlation Study 164

5.3 Temporal Correlation Study 166

6. Appendices

6.1 Appendix 1 169

6.2 Appendix 2 171

7. Bibliography 172

List of Figures

1. Introduction

Figure 1.1. Speckle pattern. 4

2. Theory

Figure 2.1. Geometry of sample. 12

Figure 2.2. Geometry for derivation of spatial autocorrelation function. 21

Figure 2.3. Scattering diagram for DAWS theory. 24

3. Apparatus and Procedure

Figure 3.1. Frequency correlation apparatus. 35

Figure 3.2. Aquarium in plane wave configuration. 37

Figure 3.3. Aquarium in point source configuration. 38

Figure 3.4. Cross section of transducer. 39

Figure 3.5. Detail of active element of transducer. 41

Figure 3.6. Sound field of transducer. 42

Figure 3.7. Sample used in frequency correlation study. 44

Figure 3.8. Temporal correlation apparatus. 53

Figure 3.9. Apparatus modification for cw generation. 54

Figure 3.10. Fluidized bed. 56

Figure 3.11. Diffuser. 57

Figure 3.12. Aquarium for DAWS study. 59

4. Analysis

Figure 4.1. Input pulses and signal transmitted through the sample. 66

Figure 4.2. FFTs of input pulse and transmitted signal, 3.24 mm sample. 68

Figure 4.3. FFTs of input pulse and transmitted signal, 10.17 mm sample. 69

Figure 4.4. Correlation functions for five sample thicknesses. 71

Figure 4.5. Diffusion profile and its FFT, the frequency correlation function. 72
Figure 4.6. 2–3 MHz plane wave correlation functions and theory. 73
Figure 4.7. 1–2 MHz correlation functions and theory. 75
Figure 4.8. 3–4 MHz correlation functions and theory. 76
Figure 4.9. 1.2–3.8 MHz correlation functions and theory. 77
Figure 4.10. 2–3 MHz point source correlation functions. 79
Figure 4.11. 2–3 MHz point source correlation functions, and theory. 81
Figure 4.12. 2–3 MHz point source correlation functions and fit curves. 83
Figure 4.13. Comparison plot of correlation functions with FFT of diffusion profile. 85
Figure 4.14. Comparison of diffusion profiles for two sample thicknesses, plane wave input. 87
Figure 4.15. Comparison of diffusion profiles for two sample thicknesses, plane wave input. 88
Figure 4.16. Comparison of point source and plane wave diffusion profiles. 90
Figure 4.17. Distribution of pathlengths through sample from different input sources. 91
Figure 4.18. Transmitted, phase, amplitude, and field. 95
Figure 4.19. Spatial correlation function, for three frequencies. 98
Figure 4.20. Spatial correlation functions, for two thicknesses. 100
Figure 4.21. Correlations from multiple scans of the sample. 102
Figure 4.22. Detail of sound detection geometry in experiment. 101
Figure 4.23. Fitting results, spatial correlations. 104
Figure 4.24. Comparison of field and intensity correlations. 106
Figure 4.25. Test of Siegert Relation 107
Figure 4.26. Sequential field snapshots. 110
Figure 4.27. Snapshots of field, with greater time between snapshots. 112
Figure 4.28. Sequential amplitude snapshots. 113
Figure 4.29. Snapshots of amplitude, with greater time between snapshots 114

Figure 4.30. Sequential phase snapshots. 116
Figure 4. 31. Snapshots of phase, with greater time between snapshots 117
Figure 4.32. Field vs. time at different sampling times. 118
Figure 4.33. Amplitude vs. time at different sampling times 119
Figure 4.34. Phase vs. time at different sampling times. 120
Figure 4.35. Phase, amplitude, and field at central sampling time. 121
Figure 4.36. Field and intensity correlation functions. 123
Figure 4.37. Test of Siegert relation. 124
Figure 4.38. Field vs. time at different bead densities. 126
Figure 4.39. Temporal correlation functions, at three bead densities. 128
Figure 4.40. Sampling times in diffusion profile. 129
Figure 4.41. Temporal correlation functions, at three sampling times. 130
Figure 4.42. Temporal correlation functions, at three mixture viscosities. 132
Figure 4.43. Noisy data from boxcar integrator. 133
Figure 4.44. Correlation function from noisy data. 135
Figure 4.45. Approaches used to correct noisy data. 136
Figure 4.46. Ballistic wave and reference pulse. 138
Figure 4.47. FFTs of reference and ballistic signals. 140
Figure 4.48. Timing diagrams used for group velocity. 141
Figure 4.49. Theoretical phase velocity curve. 145
Figure 4.50. Theoretical group velocity curve. 146
Figure 4.51. Fit to obtain diffusion constant. 148
Figure 4.52. Mean square displacement at two sampling times. 150
Figure 4.53. Mean square displacement at three volume fractions. 151
Figure 4.54. Mean square displacement at three solution viscosities. 153
Figure 4.55. Velocity variance at three viscosities. 155
Figure 4.56. Continuous wave data. 157
Figure 4.57. Field correlation function from cw data. 158
Figure 4.58 Comparison of acquisition methods. 160

1. INTRODUCTION

Although sound plays a fundamental part of our everyday lives, our comprehension of its interaction with matter has generally been limited to regimes where scattering is relatively weak. Recent developments are enabling us to begin to understand how a sound wave propagates through a multiply scattering medium and to use this understanding to develop new probes of these types of systems.

Sound is a classical wave and, as such, is an example of a broad class of waves; this class also includes electromagnetic radiation. The propagation of all classical waves obey the same physical laws, thus we are able to build on the foundations established by researchers studying the interaction of photons and matter in this study of correlations in the acoustic propagation of sound through strongly scattering, disordered media.

1.1 History

Initial investigations of electromagnetic wave propagation in strongly scattering media began before the turn of this century with Lord Rayleigh [1]. Since that time, research has largely been focused on work in the single scattering regime, with considerable research having been done in the area of quasi–elastic–light–scattering (*QELS*). This again is limited to the weak scattering limit, but significant inroads into the multiple or strongly scattering regime have been made with the realization that the propagation of light can be modeled as a random walk through the media [2]. This enables photon transport in strongly scattering materials to be

described as a diffusive process [3], subject to the condition that the sample size L is much greater than the transport mean free path l [4]. This model has proved very successful in describing such diverse behavior as correlations of the transmitted intensity with variations in incident frequency [5], angle of the sample [6], or positions of the scatterers [7,8]. This last development has been the basis for an extension of *QELS* to the strong scattering regime, called Diffusing Wave Spectroscopy, (*DWS*) [8,9]. A study of these types of correlations, using sound as the classical wave, is the focus of this thesis.

1.2 Background

The work discussed in the previous section dealt with the scattering of electromagnetic waves with matter but the underlying physics of wave propagation is common to all types of classical waves. Therefore the knowledge gained from these studies of electromagnetic waves can also be extended to acoustic waves, and this could lead to many practical applications. Traditionally measurements of the attenuation and velocity of sound have been used as sensitive probes of the material through which the sound propagates. These probes, however, have for the most part been limited to materials where little or no scattering is present. Many materials of interest scatter sound strongly, providing a practical impetus for extending the use of the diffusion approximation, developed for light in such media, to the propagation of sound waves. Recently, multiply scattered sound has been shown to obey the diffusion approximation [10]. We use this result as a starting point and continue to

explore the application of the diffusion approximation to the study of sound propagation in multiply scattering media.

Before going on to an outline of the work contained in this thesis, we give definitions of two terms frequently encountered in this study: speckle pattern and multiple scattering.

An acoustic speckle pattern, Fig. 1.1, refers to the fluctuations in intensity of sound generated by transmission of ultrasonic waves through a disordered scattering medium. This is analogous to the more common speckle pattern associated with studies of laser light. A speckle is a complex interference pattern of the *elastically* scattered wave [11], with structure dependent upon the randomness of the medium. A speckle pattern is a sample specific property and as such is a representation of all scattering centres in the medium even though they may appear to be randomly distributed.

When we refer to a multiply scattering medium, we are specifying a situation where the sample thickness L is much greater than the scattering mean free path l. This is in contrast to the opposite case where the sample thickness is of the same magnitude as l and an incident wave will suffer a single, or no, elastic scattering event before leaving the medium. This weak scattering limit is called the *Born regime* [11]. In the *multiply scattering regime*, however, the incident wave is scattered many times before emerging.

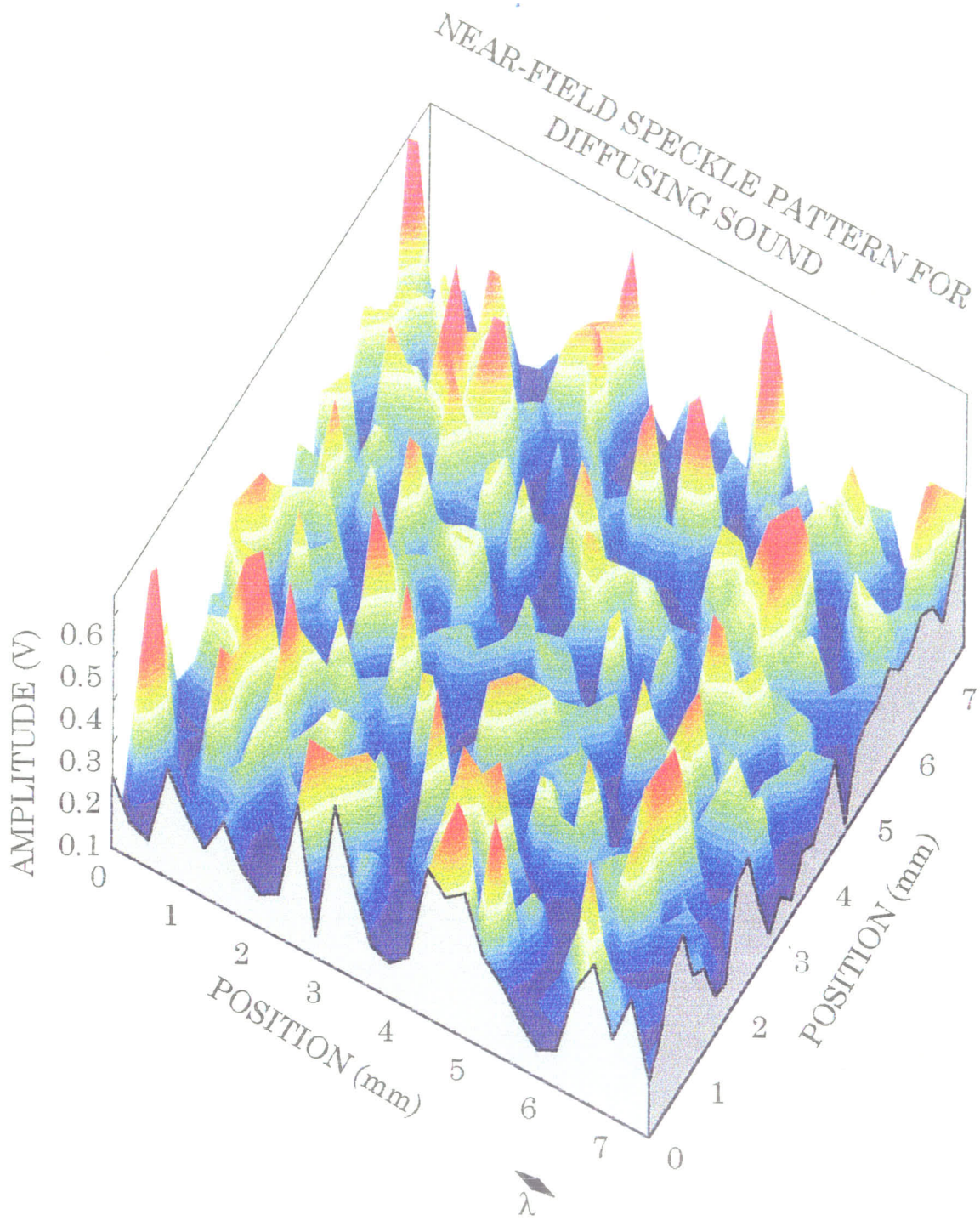

Figure 1.1. Speckle pattern for sound transmitted through glass beads in water.

1.3 Outline of Thesis

Our purpose is to investigate various correlations in sound intensity and field transmitted through a disordered medium. In essence we are analyzing acoustic speckle patterns. The correlations in which we are interested are those arising from the frequency fluctuations of the transmitted sound waves (*frequency correlation*), the spatial fluctuations (*spatial correlation*), and the temporal fluctuations (*temporal correlation*). In the first two cases the scatterers are static, but in the third case we are interested in the fluctuations of transmitted sound arising from motion of the scatterers.

This effectively separates the experiments into three main parts, each part dealing with a specific correlation function. The thesis is organized into five sections, introduction {section 1} , theory {section 2}, apparatus & procedure {section 3}, results & analysis {section 4}, and conclusions {section 5}. Each of these sections is subdivided into three parts, each part dealing with a specific correlation function.

We first discuss the theory specific to the analysis of each of the three correlation functions beginning with frequency correlations {2.1}, then spatial correlations {2.2}, and ending with the temporal correlation theory {2.3}.

Next a description of the apparatus and procedure used to acquire data for each correlation study is presented. This section also begins with the frequency correlation study {3.1} and the experimental procedure used. We then describe the procedure used in the spatial correlation study {3.2}, followed by that used in the temporal correlation study {3.3}.

Analysis of the data along with the results of each study are then presented; again we follow our format with the frequency correlation study results in section 4.1, the spatial correlations results in section 4.2, and the temporal correlations results are found in section 4.3.

1.4 References

[1] J.W. Strutt (Lord Rayleigh), *Phil. Mag.* **10**, (1880) 73.

[2] R. Pnini and B. Shapiro, *Phys. Rev.* **B39**, (1989) 6986.

[3] A. Ishimaru, *Wave Propagation and scattering in Random Media* (Academic, New York, 1978) **V.1**.

[4] A.Z. Genack, in *Scattering and Localization of Classical Waves in Random Media,* edited by Ping Sheng. (World Scientific, Singapore, 1990).

[5] J. M. Drake and A.Z. Genack, *Phys. Rev. Lett.* **55**, (1985), 2696.

[6] J.X. Zhu, D.J. Pine, and D.A. Weitz, *Phys. Rev. A* **44**, (1991) 3948.

[7] G. Maret and P.E. Wolf, *Z. Phys. B* **65**, (1989), 409.

[8] D.J. Pine, D.A. Weitz, P.M. Chaikin, and E. Herbolzheimer, *Phys. Rev. Lett.* **60**, (1988), 1134.

[9] X.L. Wu, D.J. Pine, P.M. Chaikin, J.S. Huang, and D.A. Weitz, *J. Opt. Soc. Am. B* **7** (1990), 15.

[10] J.H. Page, H.P. Schriemer, A.E. Bailey, and D.A. Weitz, *Phys. Rev. E* **52**, (1995), 3106.

[11] S. Feng, in *Scattering and Localization of Classical Waves in Random Media,* edited by Ping Sheng. (World Scientific, Singapore, 1990).

2. THEORY

The theoretical expressions governing the three types of correlations are developed in this chapter. We begin with the frequency correlation functions for two cases that are commonly considered. The first gives the correlation function {2.1.1} of multiply scattered sound when a plane wave is incident on the medium. The second frequency correlation function {2.1.2} deals with the case where the incident sound has been generated by a point source. We then present the theoretical results for the spatial correlation function, in section 2.2. Finally, the derivation of the temporal correlation function {2.3} is then considered.

2.1 Frequency Correlation Functions

2.1.1 Plane Wave Correlation Function

The propagation of sound waves through a multiply scattering medium has been shown to be described by the diffusion equation, [1],

$$\frac{\partial U}{\partial t} - D\nabla^2 U = f(t,x,y,z) \tag{1}$$

where U is the sound energy density, $D = v_E l^*/3$ is the diffusion coefficient for sound, and $f(t,x,y,z)$ is the diffusing sound source term. Here, v_E, the energy velocity, is the speed at which acoustic energy is transported through the medium, and l^*, the transport mean free path, is the distance sound travels in the medium before scattering randomizes its direction. In this approximation, sound propagating through the medium follows a distribution of paths determined by a succession of random scatterings.

We examine the transmission of sound through a slab-like arrangement of static scatterers. The detected sound field is the sum of contributions from waves having traveled many distinct scattering paths. The field emerging from the sample is

$$F = \sum_{\alpha} F_\alpha e^{i\phi_\alpha}, \tag{2}$$

where the index α denotes a scattering path of length s_α, and where the phase $\phi_\alpha = 2\pi s_\alpha/\lambda + \phi'_\alpha$ [2] includes a term ϕ'_α accounting for random phase shift due to

scattering along path α. This phase shift is uniformly distributed between $\pm \pi$ radians if restricted to a range of 2π. The intensity of the scattered sound, I, is

$$I = \sum_{\alpha,\beta} F_\alpha e^{i\phi_\alpha} F_\beta e^{-i\phi_\beta}. \tag{3}$$

Recalling that the frequency, ν, and wavelength, λ, of sound are related by the velocity v, as $v = \lambda\nu$, we write the ensemble averaged correlation function for the fields of two frequencies, ν and $\nu' = \nu + \Delta\nu$, as

$$\left\langle F_\alpha(\nu) F_\beta(\nu') \right\rangle = \left\langle \sum_{\alpha,\beta} F_\alpha F_\beta e^{i2\pi s_\alpha \nu/v} e^{-i2\pi s_\beta \nu'/v} e^{\left(\phi'_\alpha - \phi'_\beta\right)} \right\rangle. \tag{4}$$

Due to the random distribution of the scatterers the relative phases of fields from different paths are not correlated and will average to zero. The only non zero terms are those with $\phi'_\alpha - \phi'_\beta = 0$, which only happens if $\alpha = \beta$.

We now define the normalized field autocorrelation function as:

$$g_1(\Delta\nu) \equiv \frac{\sum_\alpha \left\langle F_\alpha(\nu) F_\alpha(\nu') \right\rangle}{\left\langle I(\nu) \right\rangle}. \tag{5}$$

The correlation function is found by calculating the contribution of a single path, then summing the contributions of all paths, weighting each contribution with the probability of taking that path. The probability distribution for the paths is related to the average flux of sound waves emerging from the sample at the detection point. This flux is found using the diffusion equation when appropriate boundary conditions are invoked to account for reflections at the sample interfaces.

These boundary conditions have been determined for light diffusing through a slab of scatterers [3] and the results are directly applicable to sound waves diffusing through the same geometry. For a slab of thickness L, (Fig. 2.1), the conditions are

$$U - C\frac{\partial U}{\partial z} = 0 \qquad \text{at } z = 0, \tag{6}$$

$$U + C\frac{\partial U}{\partial z} = 0 \qquad \text{at } z = L, \tag{7}$$

where

$$C \equiv \frac{2l^*}{3}\frac{1+R}{1-R} \tag{8}$$

and where R is the reflection coefficient, defined as the ratio of the incoming to the outgoing flux at the boundaries. These same authors also determine that the transmitted flux from the sample at the point of detection is

$$J_+ = \frac{Uv}{4} - \frac{D}{2}\frac{\partial U}{\partial z}. \tag{9}$$

To calculate the probability distributions we use the coordinate system shown in Fig. 2.1. Sound is incident from the $-z$ direction on a slab of thickness L.

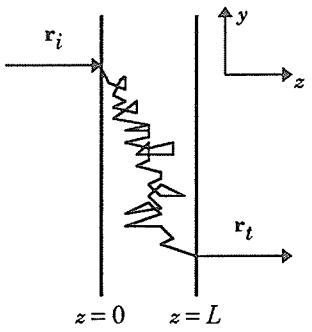

Figure 2.1 Geometry of sample

A diffusing path, of length s, is shown for sound striking the sample at point $\vec{r}_i = (x_i, y_i, 0)$ and emerging at position $\vec{r}_t = (x_t, y_t, L)$. Let $p(s, \vec{r}_i, \vec{r}_t)$ be the probability of sound following a path with length s and endpoints $\vec{r}_i$ and $\vec{r}_t$. Since the field at the detection point contains contributions from waves traveling paths that began at any point on the incident face, the field correlation function is determined by integrating over all paths and all incident points:

$$\begin{aligned} g_1(\Delta\nu) &\equiv \frac{\langle F_\alpha(\nu) F_\alpha(\nu') \rangle}{\langle F_\alpha(\nu) F_\alpha(\nu) \rangle} \\ &\cong \int ds\, dx_i\, dy_i\; p(s, \vec{r}_i, \vec{r}_t)\, e^{-i2\pi \Delta\nu s/v}\, e^{-s/l_a} \\ &= \int ds\, dx_i\, dy_i\; p(s, \vec{r}_i, \vec{r}_t)\, e^{-i2\pi \Delta\nu s l^*/3D - s/l_a}, \end{aligned} \tag{10}$$

where the exponential term, e^{-s/l_a}, accounts for absorption and l_a is called the absorption length.

To determine $p(s, \vec{r}_i, \vec{r}_t)$, we find the flux emerging from the sample at $\vec{r}_t$ at time t by solving the diffusion equation for an instantaneous pulse of sound of unit strength at point $P(x_i, y_i, z_o)$ and time $t = 0$. The initial conditions are then

$$f(t,x,y,z) = \delta(t)\delta(x - x_i)\delta(y - y_i)\delta(z - z_o), \tag{11}$$

and we expect that $z_o \cong l^*$. The flux is found by solving the diffusion equation for U and then calculating J_+ using Eq. (9). We assume U can be written as the product of three independent terms

$$U(x,y,z,t) = X(x,t)Y(y,t)Z(z,t). \tag{12}$$

We determine the X and Y dependence by finding a solution to the one dimensional diffusion equation for an infinite medium, i.e.

$$\frac{\partial X}{\partial t} - D\nabla^2 X = \delta(x - x_i)\delta(t) \tag{13}$$

for X, and

$$\frac{\partial Y}{\partial t} - D\nabla^2 Y = \delta(y - y_i)\delta(t) \tag{14}$$

for Y. The solution to the diffusion equation, corresponding to a point source of sound at initial time $t = 0$, located at a point $x = x_i$, is called the *fundamental solution* [4]. For our situation, this is

$$X(x,t) = \frac{1}{\sqrt{4\pi D t}} e^{-\frac{(x - x_i)^2}{4Dt}} \tag{15}$$

for X, and

$$Y(y,t) = \frac{1}{\sqrt{4\pi D t}} e^{-\frac{(y-y_i)^2}{4Dt}} \tag{16}$$

for Y.

The final term, $Z(z,t)$, is the solution to the one dimensional diffusion equation for Z

$$\frac{\partial Z}{\partial t} - D\nabla^2 Z = \delta(z - z_o)\delta(t), \tag{17}$$

with the boundary conditions

$$Z - C\frac{\partial Z}{\partial z} = 0 \qquad \text{at } z = 0, \tag{18}$$

$$Z + C\frac{\partial Z}{\partial z} = 0 \qquad \text{at } z = L. \tag{19}$$

Using Eq. (9) we write the flux emerging from the sample as

$$\begin{aligned} J_+ &= \frac{Uv}{4} - \frac{D}{2}\frac{\partial U}{\partial z} \\ &= \frac{XYZv}{4} - \frac{vl^*}{6}XY\frac{\partial Z}{\partial z} = XYZ\left(\frac{1}{4} + \frac{l^*}{6C}\right) = \frac{vXYZ}{2(1+R)} \end{aligned} \tag{20}$$

where Eqs. (8) and (12) are used in the last steps, and $Z = Z(z,t)\big|_{z=L}$. The time taken for the sound to travel a path of length s through the sample is s/v. Using this in Eqs. (15) and (16), the solutions for $X(x,t)$ and $Y(y,t)$, we write the outgoing flux as

$$J_+ = \frac{v^2}{8\pi Ds}\frac{e^{-\frac{(x-x_i)^2 v}{4Ds}} e^{-\frac{(y-y_i)^2 v}{4Ds}}}{(1+R)} Z(z,t)\big|_{z=L}. \tag{21}$$

This is proportional to $p(s, \vec{r}_i, \vec{r}_t)$ and we may write the correlation function, Eq. (10) as

$$g_1(\Delta\nu) \propto \int ds\, dx_i\, dy_i\, p(s, \vec{r}_i, \vec{r}_t)\, e^{-i2\pi\Delta\nu s l^*/3D - s/l_a}$$

$$= \frac{v^2}{8\pi D(1+R)} \int_0^\infty \frac{Z(z,t)\big|_{z=L}}{s} ds \int dx_i\, e^{-\frac{(x-x_i)^2 v}{4Ds}} \int dy_i\, e^{-\frac{(y-y_i)^2 v}{4Ds}}\, e^{-\frac{i2\pi\Delta\nu s l^*}{3D} - \frac{s}{l_a}} \qquad (22)$$

Integrating over x_i and y_i we obtain

$$g_1(\Delta\nu) \propto \frac{3D}{2l^*(1+R)} \int_0^\infty Z(z,t)\big|_{z=L}\, e^{-\left(\frac{3D + 2\pi i \Delta\nu l^* l_a}{3Dl_a}\right)s} ds\,. \qquad (23)$$

Making the substitutions

$$q^2 \equiv \frac{2\pi i \Delta\nu}{D}$$
$$\alpha^2 \equiv \frac{3}{l^* l_a}, \qquad (24)$$

and using $t = s/v$ to write $P(s) \propto Z(z,t)\big|_{z=L}$, our correlation function becomes

$$g_1(q) \propto \int_0^\infty P(s) e^{-\left(q^2 + \alpha^2\right) l^* s/3} ds\,. \qquad (25)$$

$P(s)$ represents the probability of a wave traversing a path of length s regardless of the entry and exit points on the sample. We see that $g_1(q)$ is the Laplace transform of $P(s)$, meaning that the solution to the Laplace transform of the one dimensional diffusion equation, Eq. (17), immediately yields $g_1(q)$. Carslaw and Jaeger have solved the diffusion equation by Laplace transform methods for a slab geometry [5]. Their solution is

$$\begin{aligned}\overline{Z} &= \int_0^\infty Z(z,t)\,e^{-pt}\,dt \\ &= \frac{1}{2D\eta^2}e^{-\eta|z-z_o|} + A\sinh(\eta z) + B\cosh(\eta z),\end{aligned} \tag{26}$$

where $\eta = \sqrt{p/D}$. We determine the coefficients A and B using the Laplace transforms of the boundary conditions for $z = 0$ and $z = L$, Eqs. (18) and (19). These are

$$\overline{Z} - C\frac{\partial \overline{Z}}{\partial z} = 0 \qquad \text{at } z = 0 \tag{27}$$

$$\overline{Z} + C\frac{\partial \overline{Z}}{\partial z} = 0 \qquad \text{at } z = L. \tag{28}$$

Solving for A and B we obtain

$$\overline{Z} = \frac{\sinh\left[(L - z + z_o)\eta\right] + C\,\eta\cosh\left[(L - z + z_o)\eta\right]}{\left(1 + C^2\eta^2\right)\sinh(L\eta) + 2C\,\eta\cosh(L\eta)}. \tag{29}$$

From Eqs. (25) and (26) we see that $g_1(q)$ is equivalent to $\overline{Z}$ if we make the transformations $s \to t/v$ and $p \to (q^2 + \alpha^2)vl^*/3$. Substituting, the field correlation function becomes

$$g_1(q) \propto \frac{\sinh\left(z_o\sqrt{q^2+\alpha^2}\right) + C\sqrt{q^2+\alpha^2}\cosh\left(z_o\sqrt{q^2+\alpha^2}\right)}{\left[1 + C^2\left(q^2+\alpha^2\right)\right]\sinh\left(L\sqrt{q^2+\alpha^2}\right) + 2C\sqrt{q^2+\alpha^2}\cosh\left(L\sqrt{q^2+\alpha^2}\right)}. \tag{30}$$

We expect the correlation function to decay more rapidly for thicker samples, because there are a larger number of scattering events encountered in long paths than there are in short paths.

2.1.2 Point Source Correlation Function

At the time of writing there does not exist an analytical form of the frequency correlation function for a point source of diffusing sound. However we use the fact that the field–field correlation function (as the frequency is varied) is the Fourier transform of the transmission time series [2] to analyze data taken with a point source. The analytical form for the transmitted sound flux through a slab–like sample of scatterers is given by [1]

$$J(t) = \frac{e^{-r^2/4Dt}\, e^{-t/\tau_a}}{2\pi L^2 t} \sum_{n=1}^{\infty} A_n\, e^{-D\beta_n^2 t/L^2}, \tag{31}$$

with

$$A_n = \frac{\beta_n\left[\beta_n K \sin\beta_n - \cos\beta_n\right]\left[\sin(\beta_n z_0/L) + \beta_n K \cos(\beta_n z_0/L)\right]}{\beta_n^2 K^2 + 2K + 1}. \tag{32}$$

Where the dimensionless constant K is given by

$$K = \frac{2l^*}{3L}\frac{1+R}{1-R}. \tag{33}$$

and the values of β_n are given by the zeros of the equation

$$\tan\beta = \frac{2\beta K}{\beta^2 K^2 - 1}. \tag{34}$$

The correlation function is then the Fourier transform of *J(t)*

$$g_1(\Delta\nu) = \frac{1}{\sqrt{2\pi}} \int_{-\infty}^{\infty} J(t) e^{-i2\pi\Delta\nu t} dt.$$

2.2 Spatial Correlation Function

In the introduction we defined a speckle as an individual bright or dark spot in the complex pattern (Fig. 1.1) seen as a result of transmission or reflection of a classical wave from a sample of randomly distributed scatterers. In this section we elaborate on those initial discussions, as we wish to generate expressions for theoretical spatial autocorrelation functions to compare with experimental data and provide a measure of speckle size. First we outline some important statistical properties of a speckle, and then discuss a simple model of the spatial correlation function employed in this thesis.

Because it is unreasonable to base the description of a speckle pattern on the exact, microscopic details of a particular ensemble of scatterers, we discuss the analysis of a speckle in statistical terms [6]. Specifically we refer to the first–order statistics of the speckle, the statistical properties of a point in space, and to the second–order statistics, where the properties refer to an area in space. An example of first order statistical properties is the probability distribution of the intensities, while a second order property is the spatial autocorrelation function [7].

2.2.1 First-Order Statistics

The probability distribution of the intensity, I, which tells us how likely it is to see a bright peak at an observation point, has been called the most important statistical property of a speckle pattern [6]. A random walk approach [6,7,8] is employed to model the distribution, where the random walk refers to the

superposition of complex amplitudes and phases of the scattered waves on the observation plane of the speckle. The probability density for the intensity has been worked out in this random walk approach [7], where the phases are assumed to be randomly distributed and there is a large number of contributions to the superposition. The result for the distribution of intensities is a decaying exponential

$$P(I) = \frac{1}{\langle I \rangle} e^{-I/\langle I \rangle}, \tag{35}$$

where $\langle I \rangle$ is the ensemble averaged intensity. In addition the distribution of the phases is

$$P(\theta) = \frac{1}{2\pi} \qquad -\pi < \theta < \pi \tag{36}$$

which is uniform on the primary interval $(-\pi,\pi)$.

2.2.2 Second-Order Statistics

While the distributions discussed in the previous section give us a simple picture of some fundamental properties of speckles, recent work [9,10,11] has focused on possible long range correlations in the speckle pattern itself. In particular, Feng *et al.* have shown the spatial correlation function to be composed of three terms, the first of which dominates the function and describes short range correlations in the speckle pattern, while the second and third terms deal with possible memory effects and with long range correlations, respectively.

In order to obtain information about the spatial properties of speckles we turn to the short range correlations that dominate the correlation function and

which describe the large intensity fluctuations seen in such patterns. The short range correlation function gives a reasonable measure of 'the average width' [7] of the speckle.

In an infinite medium, where both the source and detector are within the sample, Shapiro[12] has derived the spatial correlation function for scattered fields between two points separated by a distance, Δx, as

$$g_1(\Delta x) = \frac{\sin(k\Delta x)}{k\Delta x} e^{-\frac{\Delta x}{2l}}, \tag{37}$$

where k is the wavevector in the medium, and l is the scattering mean free path. This expression is valid for $\Delta x < l$. It is stressed that this result only holds when the sound is detected *inside* the medium.

In our experiment, however, the detector is placed outside the sample, separated from the surface by a short distance z. The circular geometry of our problem allows us to make use of a familiar form of the autocorrelation function developed for an optical reflection experiment where a circular rough surface is uniformly illuminated by a coherent source.

The result we will use arises from a calculation of the field autocorrelation for two points (x_1,y_1) and (x_2,y_2) in the (x,y) plane of observation of a speckle generated by reflecting light off a rough (compared with the input wavelength) surface in the (x',y') plane, Fig. 2.2.

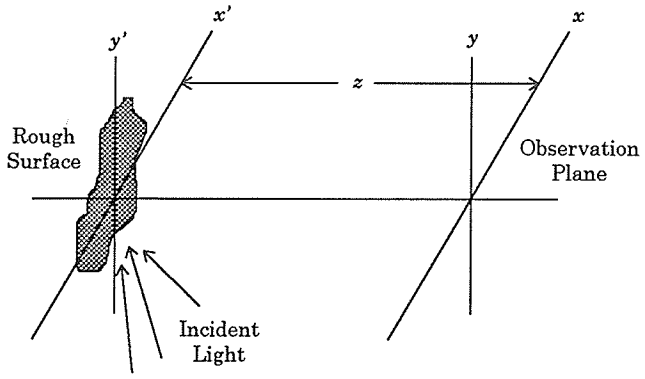

Figure 2.2. Geometry for derivation of autocorrelation function.

The autocorrelation function is

$$g_1(x_1,y_1;x_2,y_2) = \left\langle S(x_1,y_1)S^*(x_2,y_2)\right\rangle \tag{38}$$

where $S(x,y)$ is the field at point (x,y). In order to calculate this correlation function one employs a relationship between the fields at the scattering surface, $\alpha(x',y')$, and the fields in the observation plane $S(x,y)$. The required relationship is the Huygens–Fresnel principle, which allows us to write $S(x,y)$ as

$$S(x,y) = \frac{1}{\lambda z} e^{-i\frac{\pi}{\lambda z}\left(x^2+y^2\right)} \iint\limits_{all\ space} \alpha(x',y') e^{-i\frac{\pi}{\lambda z}\left(x'^2+y'^2\right)} e^{i\frac{2\pi}{\lambda z}(xx'+yy')} dx'\,dy'. \tag{39}$$

With this one is able to compute the autocorrelation function [7] giving,

$$g_1(\Delta x) = 2\frac{J_1\left(\frac{\pi D}{\lambda z}\Delta x\right)}{\frac{\pi D}{\lambda z}\Delta x}, \tag{40}$$

where J_1 is the first order Bessel function, Δx is the spatial separation of points in the observation plane, D is the diameter of the circular rough surface, and z is the distance between the surface and the observation point.

We use the decay of the correlation function to give us an indication of the speckle size. Specifically we look for the separation at which $g_1(\Delta x)$ first decays to zero and (40) tells us that the speckle size is roughly $\sim\lambda z/D$. This means that the speckle size increases with increasing z and increasing λ, while decreasing with increasing D.

2.3 Temporal Autocorrelation Function

In this section we develop a theoretical expression for the temporal field autocorrelation function of multiply scattered sound from a medium where the scatterers are in motion. For moving scatterers, the scattered sound field exhibits temporal fluctuations resulting from the change in phase of the scattered waves. These temporal fluctuations can be characterized by the time correlation function $g_1(\tau)$ of the scattered sound field. Analysis of the temporal correlation function yields information on the motion of the scattering particles.

We begin by considering a wave that is detected after having been scattered by a sequence of n uniform, separate, scatterers located at positions $\bar{r}_1,.....,\bar{r}_n$. For a scattered sound path consisting of n scatterings, the autocorrelation function is

$$\begin{aligned} g_1^{(n)}(\tau) &\equiv \left\langle F^{(n)}(0)F^{(n)}(\tau)\right\rangle \Big/ \left\langle \left|F^2\right|\right\rangle \\ &= \frac{\left\langle \left|F^{(n)}(0)\right|^2\right\rangle}{\left\langle \left|F^2\right|\right\rangle}\left\langle e^{-i\Delta\phi^{(n)}(\tau)}\right\rangle \end{aligned} \tag{41}$$

where $F^n(\tau)$ is the contribution to the scattered sound field from the path, $\left\langle \left|F^2\right|\right\rangle$ is the average intensity, and $\Delta\phi^{\,n}(\tau)$ is the total change in its phase due to the motion of all n scatterers in the path during the time interval τ. From Fig. 2.3 it is clear that this phase change is

$$\Delta\phi^{(n)}(\tau) = \sum_{i=1}^{n}\Delta\phi_i^n(\tau) = \sum_{i=1}^{n}\bar{k}_i\cdot\left(\Delta\bar{r}_{i+1}(\tau) - \Delta\bar{r}_i(\tau)\right) \tag{42}$$

where $\Delta\vec{r}_i(\tau) = \vec{r}_i(\tau) - \vec{r}_i(0)$ is the position change of the ith scattering particle in time τ, and k_i is the wavevector of the scattered wave from particle i pointing towards particle $i+1$.

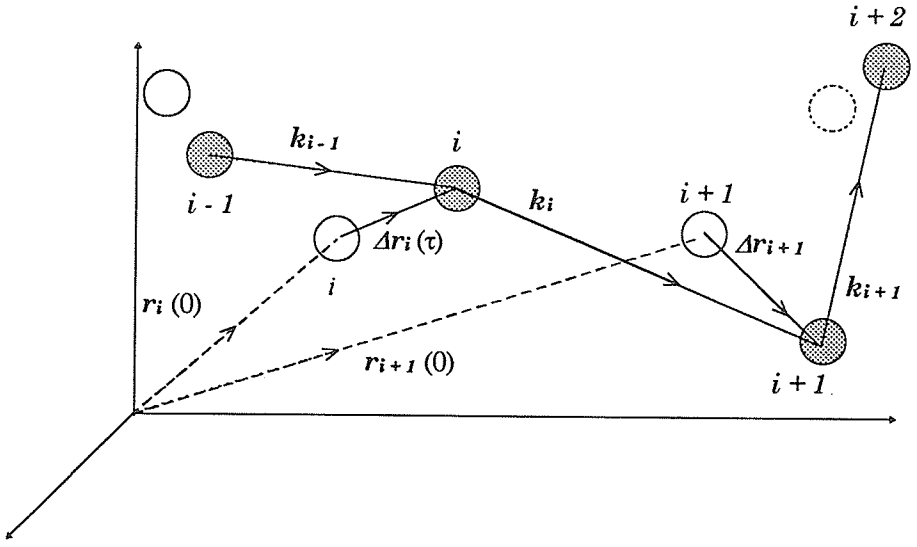

Figure 2.3. Scattering diagram for DAWS theory.

Equation (42) shows explicitly that it is only *relative* motion of the scatterers within the sample that contributes to $\Delta\phi^{n}(\tau)$. Alternatively $\Delta\phi^{n}(\tau)$ can be written in terms of the scattering wavevector $\vec{q}_i = \vec{k}_i - \vec{k}_{i-1}$ as

$$\Delta\phi^{(n)}(\tau) = \sum_{i=1}^{n} \vec{q}_i \cdot \Delta\vec{r}_i(\tau) \tag{43}$$

Returning to Eq. (41) we write the average contribution to $g_1^{(n)}(\tau)$ from all paths with n events as

$$g_1^{(n)}(\tau) = P(n)\left\langle \prod_{i=1}^{n} e^{-i\Delta\phi_i(\tau)} \right\rangle, \tag{44}$$

where the factor $P(n) \equiv \left\langle \left| F^{(n)}(0) \right|^2 \right\rangle \Big/ \left\langle \left| F^2 \right| \right\rangle$ is the fraction of the total scattered sound intensity in paths having n scattering events. The total field autocorrelation function is obtained by summing over all paths that contribute to the total field measured at the detector:

$$g_1(\tau) = \sum_n g_1^n(\tau) = \sum_{n=1}^{\infty} P(n)\left\langle \prod_{i=1}^{n} e^{-i\Delta\phi_i(\tau)} \right\rangle. \tag{45}$$

In a continuous wave experiment, this summation extends over all n. However in a pulsed experiment the summation is restricted to include only those paths whose length differs by the pulse length ($\Delta t/v$). In particular, for a narrow pulse $P(n)$ is essentially constant in the summation over n and the field correlation function takes on the relatively simple form

$$g_1^{t_s}(\tau) = \left\langle \prod_{i=1}^{n} e^{-i\Delta\phi_i(\tau)} \right\rangle \tag{46}$$

where $t_s = s/v_E$ is the observation time at which the correlation function is measured, corresponding to a path of length $s = nl$, where l is the scattering mean free path.

For large n it is a good approximation to assume that the phase shifts between scattering events are uncorrelated. This allows us to write Eq. (46) as

$$g_1^{t_s}(\tau) = \left\langle e^{-i\Delta\phi_i(\tau)} \right\rangle^n. \tag{47}$$

To evaluate (47) we note that, for the range of times over which $g_1^{t_s}(\tau)$ can be reliably measured, $\Delta\phi_i(\tau)$ is small for any step along any path having large n. Hence the exponential can be expanded

$$\left\langle e^{-i\Delta\phi_i(\tau)}\right\rangle^n \cong \left[1 - i\left\langle\Delta\phi_i(\tau)\right\rangle - \frac{1}{2}\left\langle\left(\Delta\phi_i(\tau)\right)^2\right\rangle - \cdots\cdots\right]^n \qquad (48)$$

so that the leading terms can be averaged individually. For random motion we must have $\langle\Delta r(\tau)\rangle = 0$, since we are averaging over a large number of scatterers and we expect their relative motions to be uncorrelated. Using Eq. (42) we write the change in phase $\Delta\phi_i(\tau)$ as

$$\begin{aligned}\Delta\phi_i(\tau) &= \vec{k}_i\cdot\left(\Delta\vec{r}_{i+1}(\tau) - \Delta\vec{r}_i(\tau)\right)\\ &= k_o\left[\Delta r_{i+1}(\tau)\cos\alpha_i - \Delta r_i(\tau)\cos\beta_i\right]\end{aligned} \qquad (49)$$

where α_i and β_i are the angles between $\vec{k}_i$ and $\Delta\vec{r}_i(\tau)$ and $\Delta\vec{r}_{i+1}(\tau)$ respectively, and $k_o = |\vec{k}_i|$. Since the directions of $\vec{k}_i$ and $\Delta\vec{r}_i(\tau)$ are uncorrelated (α_i and β_i, when averaged over many scatterings, have a flat distribution) the averages in Eq.(48) are easy to perform. The first term gives

$$\begin{aligned}\left\langle\Delta\phi_i(\tau)\right\rangle &= k_o\left[\left\langle\Delta r(\tau)\right\rangle\left\langle\cos\alpha\right\rangle - \left\langle\Delta r(\tau)\right\rangle\left\langle\cos\beta\right\rangle\right]\\ &= 0\end{aligned} \qquad (50)$$

since $\langle\Delta r(\tau)\rangle = 0$ and also

$$\begin{aligned}\left\langle\cos\alpha\right\rangle &= \int\cos\alpha\,d\Omega \Big/ \int d\Omega\\ &= \tfrac{1}{2}\int\cos\alpha\sin\alpha\,d\Omega\\ &= 0\end{aligned}$$

The second term in Eq.(48) gives

$$\begin{aligned}\tfrac{1}{2}\left\langle\left(\Delta\phi_i(\tau)\right)^2\right\rangle &= \tfrac{1}{2}k_o^2\left\langle\left(\Delta r(\tau)\cos\alpha\right)^2\right\rangle \\ &\quad - 2\left\langle\Delta r^2(\tau)\cos\alpha\cos\beta\right\rangle \\ &\quad + \left\langle\left(\Delta r(\tau)\cos\beta\right)^2\right\rangle \\ &= \tfrac{1}{2}k_o^2\left\langle\Delta r^2(\tau)\right\rangle\left(\left\langle\cos^2\alpha\right\rangle + \left\langle\cos^2\beta\right\rangle\right) \\ &= \tfrac{1}{3}k_o^2\left\langle\Delta r^2(\tau)\right\rangle\end{aligned} \tag{51}$$

since in 3 dimensions

$$\begin{aligned}\left\langle\cos^2\alpha\right\rangle &= \int\cos^2\alpha\sin\alpha\,d\Omega \Big/ \int d\Omega \\ &= \tfrac{1}{2}\left[-\frac{\cos^3\alpha}{3}\right]_0^{\pi} \\ &= \frac{1}{3}\end{aligned}$$

and similarly for $\left\langle\cos^2\beta\right\rangle$.

Thus Eq.(48) can be written

$$\begin{aligned}\left\langle e^{-i\Delta\phi_i(\tau)}\right\rangle^n &= \left[1 - \frac{1}{3}k_o^2\left\langle\Delta r^2(\tau)\right\rangle - \cdots\cdots\right]^n \\ &\approx e^{-\frac{1}{3}k_o^2\left\langle\Delta r^2(\tau)\right\rangle n}\end{aligned} \tag{52}$$

and the field correlation function for a pulsed experiment is

$$g_1^{t_s}(\tau) = e^{-\frac{1}{3}k_o^2\left\langle\Delta r^2(\tau)\right\rangle s/l} \tag{53}$$

In the continuum limit the sum over n is approximated by an integral over all scattering path lengths s

$$g_1(\tau) = \int P(s)\, e^{-\frac{1}{3}k_o^2\langle \Delta r^2(\tau)\rangle \frac{s}{l}} ds, \tag{54}$$

where $P(s)$ is now the fraction of total scattered sound intensity that has traveled a path of length s through the sample to the detection point, and can be calculated from diffusion theory using appropriate boundary conditions [1].

For large particles, where sound is not isotropically scattered, we must replace l by l^*, the transport mean free path [6]. We can establish the relationship between l and l^* by the following argument: the scattering mean free path, l, is generally less than l^* for anisotropic scatterers [14] and l^* can be obtained by summing the projections of all steps of length l in the path onto the direction of the first step. Thus

$$l^* = l\sum_{i=1}^{n}\langle \cos\theta \rangle^i \tag{55}$$

where $\langle \cos\theta \rangle$ is the average angle between steps. For large n this is $l^* = l/(1-\langle \cos\theta \rangle)$. In general we write,

$$g_1^{t_s}(\tau) = e^{-\frac{1}{3}k_o^2\langle \Delta r^2(\tau)\rangle s/l^*} \tag{56}$$

By inverting this equation we obtain a useful expression for the mean square displacement of the scattering particles, which in turn yields information regarding the particle dynamics

$$\langle \Delta r^2(\tau)\rangle = -\frac{3l^*}{sk_o^2}\ln\left(g_1^{t_s}(\tau)\right) \tag{57}$$

We now determine analytical expressions of $\langle \Delta r^2(\tau) \rangle$ as a function of time for various types of particle motion. Specifically we examine stochastic or random motion, and then deterministic motion.

2.3.1 Stochastic Motion

For stochastic motion, the particle movements are described as a random walk, with the classic example being Brownian motion. For random motion, the mean particle displacement is zero, and the mean square displacement is given by

$$\langle \Delta r^2(\tau) \rangle = 6D_p\tau \tag{58}$$

where D_p is the single particle diffusion coefficient [15]. This indicates that for random motion the mean square particle displacement increases linearly with time.

For the large, 0.5 mm-diameter particles used in our experiment, stochastic motion resulting from the Brownian motion of the particles is negligible. However, non-Brownian mechanisms, such as collisions between the particles when subjected to a fluid flow can also cause the motion to appear stochastic on a length scale corresponding to the collision mean free path. Whether or not this type of stochastic behavior is observed thus depends on the distance over which particle motion is probed.

2.3.2 Deterministic Motion

For deterministic motion, the particles move in response to an external stimulus and therefore do not move randomly during the time interval τ. However, the motion is generally far from uniform, one example being the particle dynamics

typical of inhomogeneous convective flows. For deterministic motion, the particle displacements can be written

$$\Delta\vec{r}_i(\tau) = \bar{V}_i t$$

where $\bar{V}_i t$ is the velocity of the ith scatterer. When $\langle \Delta r\ (\tau) \rangle = 0$, the mean square particle displacement is given by

$$\langle \Delta r_i^2(\tau) \rangle = \langle \Delta V_i^2 \rangle \tau^2 \tag{60}$$

where

$$\langle \Delta V_i^2 \rangle = \langle V_i^2 \rangle - \langle V_i \rangle^2$$

is variance of the particle velocity. From Eq. (60) we see that $\langle \Delta r^2(\tau) \rangle$ varies quadratically with time. We can therefore measure the variance in velocity by obtaining the temporal autocorrelation function in an experiment.

This holds only for the case where $\langle \Delta r\ (\tau) \rangle = 0$. In other types of deterministic motion there are correlations between the motions of individual beads and for these $\langle \Delta r(\tau) \rangle \neq 0$. One example is shear flow [14], for which, as in the case of convective motion, the argument of the exponential in the correlation varies as τ^2. However it is the velocity gradient and not the velocity variance that is measured for the case where $\langle \Delta r(\tau) \rangle \neq 0$.

2.4 References

[1] J.H. Page, H.P. Schriemer, A.E. Bailey, and D.A. Weitz, *Phys. Rev. E* **52**, (1995), 3106.

[2] A.Z. Genack, in *Scattering and Localization of Classical Waves in Random Media,* edited by Ping Sheng. (World Scientific, Singapore, 1990).

[3] J.X. Zhu, D.J. Pine, and D.A. Weitz, *Phys. Rev. A* 44, (1991) 3948.

[4] D.G. Zill, *Differential Equations with Boundary-Value Problems,* (PWS-Kent, Boston, 1989) **2**, 142.

[5] H.S. Carslaw and J.C. Jaeger, *Conduction of Heat in Solids,* **2ed**. Clarendon Press, Oxford, (1959), 373

[6] J.W. Goodman, *J. Opt. Soc. Am.*, **66**, (1976), 1135.

[7] J.W. Goodman, in *Laser Speckle and Related Phenomena,* edited by J. C. Dainty . Springer Verlag, Berlin, **9**, (1975), pp. 9 –35.

[8] S. Feng, in *Scattering and Localization of Classical Waves in Random Media,* edited by Ping Sheng. (World Scientific, Singapore, 1990).

[9] S. Feng, C. Kane, P. Lee, and A. D. Stone, *Phys. Rev. Lett.* **61**, (1988), 834.

[10] E. Kogan, and M. Kaveh, *Phys. Rev. B* **45**, (1992-II), 1049.

[11] R. Pnini and B. Shapiro, *Phys. Rev.* **B39**, (1989) 6986.

[12] B. Shapiro, *Phys. Rev. Lett.* **57**, (1986), 2168.

[13] D.J. Pine, D.A. Weitz, G. Maret, P.E. Wolf, E. Herbolzheimer, and P.M. Chaikin, in *Scattering and Localization of Classical Waves in Random Media,* edited by Ping Sheng. (World Scientific, Singapore, 1990).

[14] X. Qui, X.L. Wu, J.Z. Xue, D.J. Pine, D.A. Weitz, and P.M. Chaikin, *Phys. Rev. Lett.* **65**, (1990), 516.

[15] F. Reif, *Fundamentals of Statistical and Thermal Physics.* (McGraw Hill, 1965), 486.

3. APPARATUS AND PROCEDURE

In this section we outline the methods by which the data were acquired and the relevant apparatus used in those acquisitions. We focused on three areas of interest: frequency, spatial, and temporal correlation studies. In each case ultrasound was focused on samples of random scatterers and detected emerging from the opposite face of the sample. The scatterers in the frequency and spatial correlation studies were static, while in the temporal correlation, or diffusing acoustic wave study, the scatterers were in motion.

Beginning with the frequency correlation study, we outline the apparatus used, including brief descriptions of major components and sample preparation along with a discussion of the method by which data were collected. The spatial correlation study is then described in this manner followed by the diffusing wave study. As a number of pieces of apparatus were common to the three studies, we avoid repetitive descriptions by describing common components as they are introduced.

3.1 Frequency Correlation Study

Frequency correlation data were collected for two types of incident ultrasound. In the first case, a small diameter flat transducer generated approximate plane waves which were passed through a sample of static scatterers. In the second case, a spherical focus transducer focused waves to a point on the input face of the sample. In both cases, the sound field that was transmitted through the sample was detected using a miniature transducer or hydrophone. Specific transducers were required to generate each type of wavefront, so that in each case a different arrangement of generating transducer, sample and hydrophone was needed. We discuss these arrangements and the motivation for each in the following paragraphs, after first describing the general layout of the experiment.

The general arrangement of apparatus for the frequency correlation study is depicted in the following diagram, Fig. 3.1.

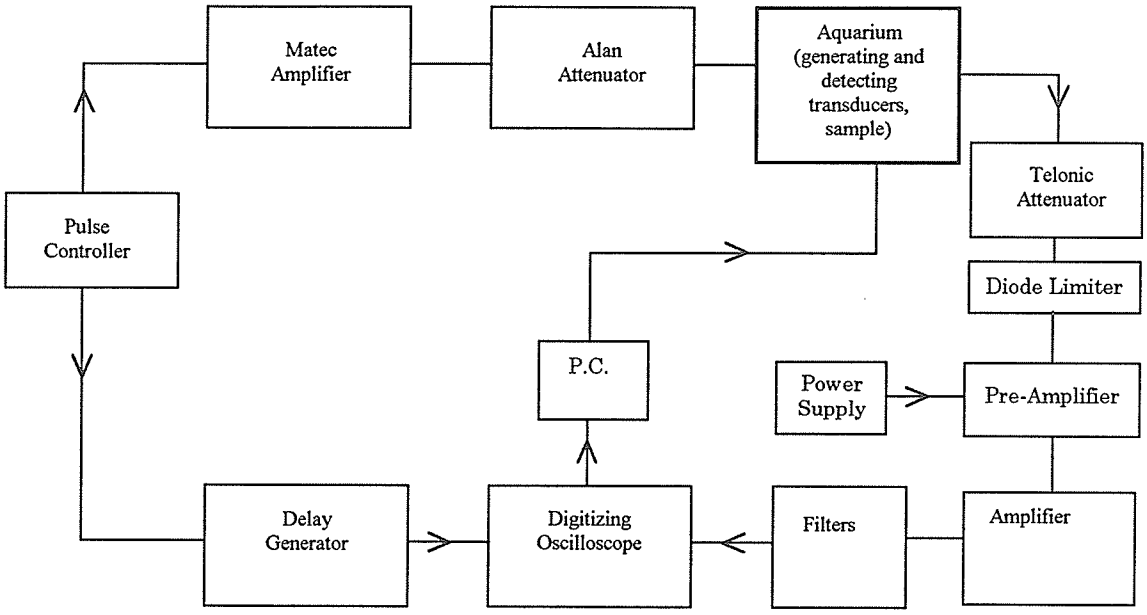

Figure 3.1. Block diagram of frequency correlation apparatus.

We wished to generate a sound pulse, direct it towards a sample of random scatterers and detect the scattered sound field emerging from a point on the opposite side of the sample. To achieve this, the Matec amplifier generated an electronic pulse train of width and repetition rate determined by the pulse controller. This signal was attenuated by the Alan attenuator, converted to an acoustic signal by a transducer and directed at the sample. After this signal had diffused through the sample, it was detected by a hydrophone, and converted back to an electronic signal. The transducer, sample and hydrophone were immersed in a water tank which provided a homogeneous low attenuation coupling medium for sound propagation.

The signal from the hydrophone was attenuated, and spurious peaks were blocked with a diode limiter. The resultant signal was then amplified and filtered using an high pass filter to block low frequency noise at the input to the oscilloscope. Finally the signal was digitized by the oscilloscope and then downloaded to the computer.

As the scatterers were static, sound emerging from the sample at a specific point had always traveled the same distribution of paths. To examine different path distributions it was necessary to acquire data at different detection points on the sample's back face. This was achieved by translating the sample between acquisitions in the focused sound study, and translating the detecting hydrophone in the plane wave study.

This basic arrangement of equipment was the same in the frequency correlation and spatial correlation studies, with only the relative positions of the hydrophone, sample and transducer within the aquarium changing for each study.

3.1.1 Aquarium

We used a 425 litre aquarium within which the sample, hydrophone and transducer were suspended, Figs. 3.2 and 3.3. The walls and floor of the tank were lined with sheets of 2.5-cm-thick Styrofoam insulation to damp any reflections off these surfaces. Glued to these sheets were parallel strips of the insulation vertically spaced 10 cm apart, effectively ribbing the tank to further attenuate any reflected signals. An iron frame surrounded the tank supporting the holding assemblies for the sample, transducer and hydrophone. The two types of waves used in the

frequency correlation study required separate arrangements of hydrophone, sample and transducer. We describe each set-up individually, starting with the plane wave configuration. Fig. 3.2 shows the arrangement of the sample and acoustic equipment in this configuration.

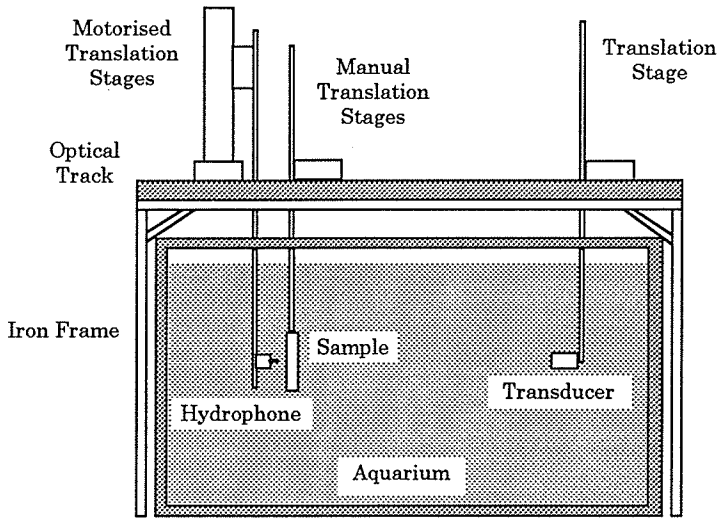

Figure 3.2. Aquarium arrangement in plane wave configuration.

The hydrophone is mounted on two motorized translation stages allowing it to move in a plane parallel to the sample face. The sample was sandwiched between metal rings and these were connected to two manual translation stages allowing movement in transverse and longitudinal directions. The flat-faced, plane-wave transducer was mounted on a single stage allowing transverse motion. The sample was placed in the far field of the transducer. The hydrophone was placed within 2 mm of the back face of the sample. In order that no signal was detected leaking around the sample, a baffle of Styrofoam surrounded the sample (not shown). By

moving the hydrophone around with the translation stages, we acquired data from various scattering distributions in the sample. We translated the hydrophone over an 11 × 11 grid of 3 mm spacing, acquiring data at each point.

The sample was held stationary with respect to the generating transducer to ensure that the sound incident on the sample face represented the flat part of the transducer output, as discussed in further detail in the section on transducers (Pg. (39)). If we had moved the sample and held the transducer and hydrophone stationary then, because the signal illuminated the entire face of the sample rather than focused to a point, at some positions we would collect unreliable data since the sound field would have impinged upon part of the baffle rather than the sample face.

We now discuss the focused-waves configuration; a schematic of the acoustic apparatus in this configuration is shown in Fig. 3.3.

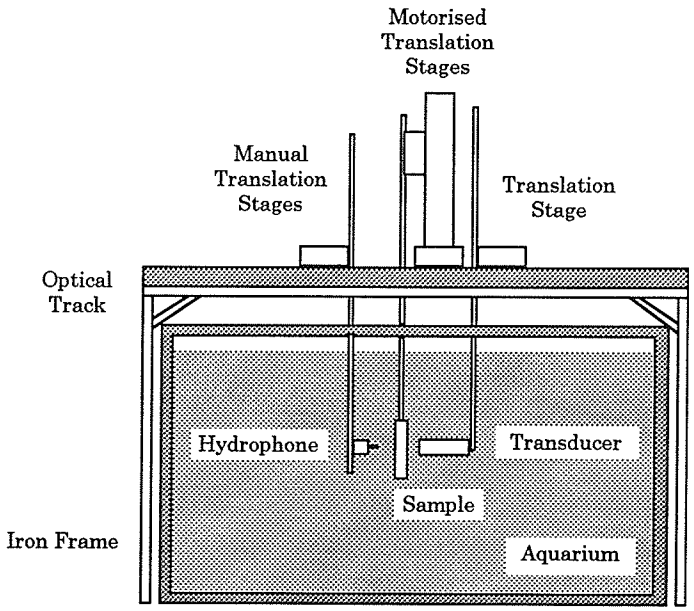

Figure 3.3. Aquarium arrangement in the point source configuration.

The front face of the sample was positioned at the focus of the transducer. The entire sample was mounted to the motorized translation stages. The hydrophone was placed within 2 mm of the rear face of the sample. We held the hydrophone and generating transducer on axis and translated the sample over the same 11 × 11 grid pattern as in the plane wave case. Because the amount of sound detected by the hydrophone decreased dramatically as it was moved off-axis from the transducer focus, to gather data from different scattering paths it was necessary to translate the sample rather than the hydrophone as was done for plane waves.

3.1.2 Transducers

This experiment utilized two types of immersion transducers of cylindrical shape: a focusing transducer of diameter 2.54 cm, focus 5.67 cm, and central frequency 2.5 MHz, and a flat transducer of diameter 0.635 cm and central frequency 2.5 MHz. This flat transducer generated approximate plane waves as long as they were detected in its far field, which we define below. The cross section of a typical immersion transducer is shown in Fig. 3.4.

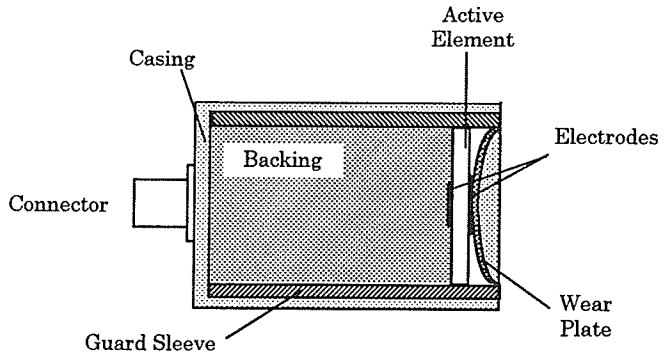

Figure 3.4. Cross section of spherical focus immersion transducer.

Transducers exploit properties of piezoelectric crystals to convert between electrical and mechanical energy. Ultrasonic transducers are used to generate and detect sound fields at frequencies above 20 KHz, with typical values between 1 and 20 MHz.

The characteristics of the active element, the backing and the wear plate determine the performance of the transducer. The active element is of high acoustic impedance and is designed to produce longitudinal waves. The backing is a dense, highly attenuative, high density material with acoustic impedance matched to that of the active element. The impedance match between the backing and active element ensures that the transducer, while heavily damped and lower in signal amplitude, exhibits good broadband characteristics and high range resolution. The wear plate is designed to function as a transformer between the water and the active element. The thickness is chosen so that waves generated by the active element and those undergoing reflections in the wear plate are emitted in phase causing constructive interference to occur, thereby strengthening the emitted signal Fig. 3.5.

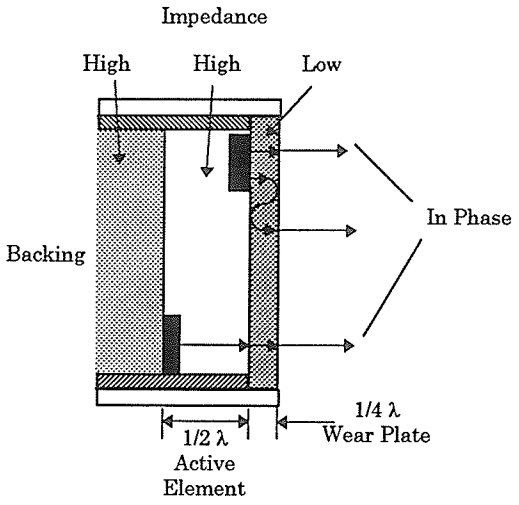

Figure 3.5. Detail of relationship between wear plate and active element f or a plane wave immersion transducer.

A transducer generates a sound field that can be separated into two regions, the *near field* and the *far field.* The near field is the area immediately in front of the transducer and has sound profile that is composed of a number of maxima and minima. As the distance from the transducer face increases, the number of maxima decreases, becoming a single maximum at the near field distance, or *natural focus,* of the transducer. Beyond this natural focus is the far field region where the pressure of the sound field decreases rapidly with the peak becoming less sharply defined. As this peak becomes flatter, the wavefront begins to approximate a plane wave. A representation of this is shown in Fig. 3.6.

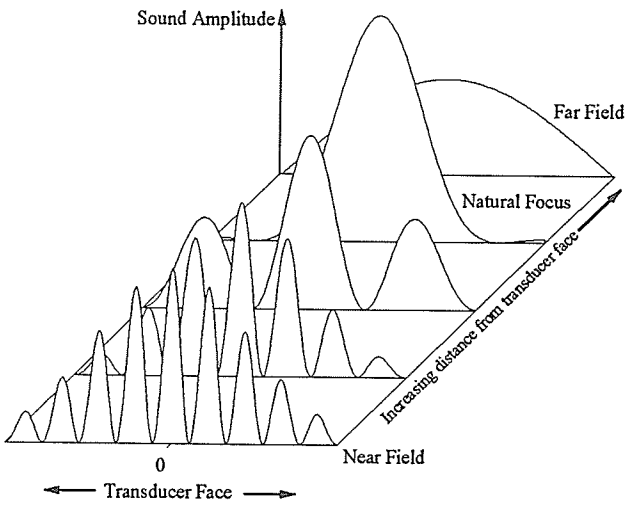

Figure 3.6. Representation of Sound Field as a function of distance from transducer face.

We can calculate the near field distance, N, for a transducer using the following equation

$$N = \frac{D^2 f}{4v} \tag{1}$$

where D is the diameter of the transducer element, v is the velocity of sound and f is the frequency. We used a small 0.635 diameter transducer in order to achieve a close near field distance, giving the sound a longer region to disperse in before impinging on the sample. The natural focus for our transducer is at 1.4 cm and we placed the sample 72 cm from the transducer face. At this distance from the focus the sound profile was nearly flat across an area of more than 4 cm^2.

The spherical focus transducer used in the experiment uses an acoustic lens to shift the natural focus closer to the transducer face resulting in an increased signal amplitude. The parameter that characterizes this increase is called the

normalized focal length S_F. This is the ratio of the focus in water, F, of the transducer to its near field distance i.e. $S_F = F/N$. Another important parameter of a focusing transducer is the focal zone, the region surrounding the normalized focus, bounded by the – 6 dB points of the signal amplitude. The length of this zone is determined by

$$F_Z = N S_F^2 \left[\frac{2}{1 + 0.5 S_F} \right]. \qquad (2)$$

Our 2.54 cm diameter focusing transducer thus has a near field distance of 2.5 cm, a normalized focal length of 2.26 cm, and a focal zone of 12.0 cm, in the middle of which we placed the sample.

3.1.3 Hydrophone

A standard transducer, identical to those used for generation of ultrasound, is also capable of sound detection and could have been used in the experiment to detect the signal emerging from the sample. However these large diameter transducers sense an average acoustic field across their entire face, while the area over which the signal is constant in phase and amplitude is on the order of a wavelength. This average acoustic field is then a superposition of interfering phases and amplitudes. We wanted to be able to detect the signal from a single speckle, or coherence area, where the phase and amplitude were constant. Therefore we used a miniature hydrophone of area comparable to the speckle size to detect the ultrasound.

This hydrophone was a needle-shaped instrument, the point of which was a ceramic crystal encased in gold foil. The crystal acted as a piezoelectric element, detecting sound emerging from the sample and converting it to an electronic signal. The diameter of the tip of hydrophone was less than the wavelength of the ultrasound. There were two of these hydrophones, manufactured by Specialty Engineering Associates, one having a 400 μm diameter tip, the other a tip of 200 μm diameter. The hydrophone came supplied with its own pre-amplifier, of gain 30 dB, used to improve the signal to noise ratio of the detected signal.

3.1.4 Sample Preparation

Samples consisted of 10 cm diameter cells filled with 1 mm diameter glass beads and distilled water. The cells were made from a thickness of PVC tubing of circular cross-section, faced by thin sheets of polystyrene plastic, Fig. 3.7.

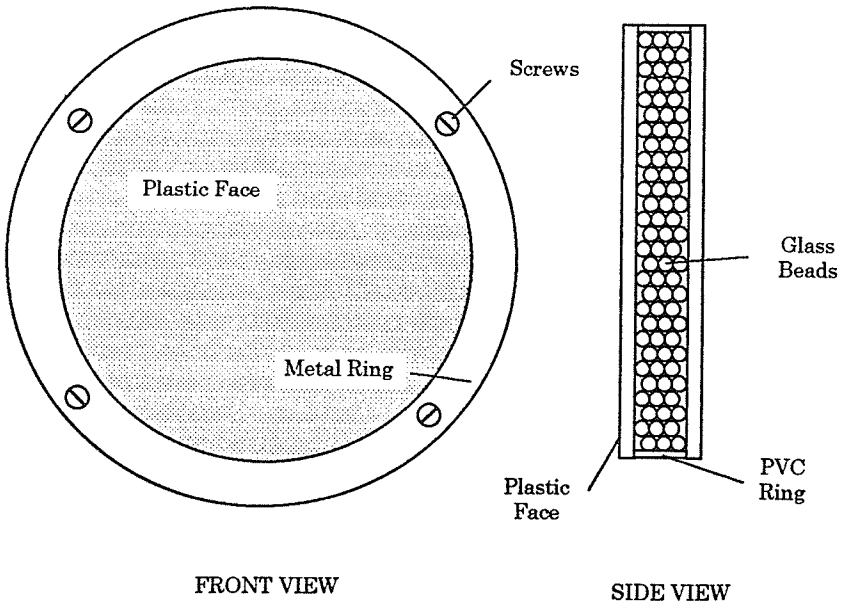

Figure 3.7. Sample cell.

The beads were packed to a density of approximately 0.63 in the following manner. The mass of the empty cell was measured. The cell was filled with distilled water introduced through a hole in the PVC. The mass of the cell filled with water was measured. The cell was then clamped in a vice between flat sheets of metal to ensure the cell thickness remained constant as beads were packed in. Beads were then introduced into the cell. As the cell filled up, displaced water was forced out of the hole causing the beads to form clumps and jam the hole. This was circumvented by gently tapping on the metal sheets, causing the beads to fall through the hole. This small vibration also allowed the beads to settle evenly throughout the cell. Also, as the cell became fuller the beads were packed tightly by tamping them down with thin rods. Measuring the mass of the cell after the beads were packed enabled a calculation of the packing fraction to be made using the following equation

$$\begin{aligned} Packing\ Fraction &= \frac{volume\ of\ beads}{total\ volume\ of\ cell} \\ &= \frac{m_B / \rho_G}{V_T} \end{aligned} \tag{3}$$

where ρ_G is the density of glass and m_B is the mass of the beads. Since the mass of the beads is not known, we write this equation in terms of known and measurable quantities. The total volume is written as the sum of the volumes of beads and water in the cell

$$\begin{aligned} V_T &= V_B + V_{H_2O} \\ &= \frac{m_B}{\rho_G} + \frac{m_{H_2O}}{\rho_{H_2O}} . \end{aligned} \tag{4}$$

Now the total mass is just

$$m_T = m_B + m_{H_2O} \tag{5}$$

so that we can combine Eqs. (4) and (5) to solve for the mass of beads,

$$m_B = \frac{\left(\rho_{H_2O} V_T - m_T\right)\rho_G}{\rho_{H_2O} - \rho_G}. \tag{6}$$

Using this result in Eq. (3) we write the packing fraction as

$$Packing\ Fraction = \frac{\left(\rho_{H_2O} V_T - m_T\right)}{\left(\rho_{H_2O} - \rho_G\right)V_T}. \tag{7}$$

In this manner cells were constructed having thickness 3, 5, and 10 mm. A thin, 1.9 mm, sample was constructed in a slightly different fashion, having a square cross section with a single thin strip of polystyrene serving as sides in place of the PVC ring.

After a cell was filled, the hole was sealed and the cell stored in a distilled water bath until used.

3.1.5 Translation Stages

The motorized translation stages were manufactured by Unislide. These could move 30 cm in increments of 3150 steps per cm. The movement of the stages was directed by computer over a GPIB bus. The computer code controlling the translation stages was written to work in conjunction with code directing the oscilloscope to acquire and download data to a PC. Thus we were able to direct the computer to acquire data at any number of positions, telling it where to start and

what sort of grid to examine. Then we simply let the instruments gather the data with minimal human interaction.

3.1.6 Matec 6600 rf Pulse Generator

We used a Matec 6600 rf Pulse Generator in conjunction with a model 755 rf Plug-In to generate the ultrasonic signal. These devices were capable of producing electromagnetic pulses in the frequency range between 1 and 20 MHz at an rms power of 1 KW. The pulse width was variable between 0.5 and 100 μs. The pulse amplitude was also continuously variable between zero and maximum with a nominal output of 1 KW at its peak. We were able to trigger the pulse generator externally using an 'in house' manufactured pulse generator that allowed us to set a width for each pulse and repletion rate for a train of pulses.

3.1.7 Oscilloscope

We used a Tektronix 544A Digitizing Oscilloscope to acquire, digitize, and in the diffusing wave case, store data. The oscilloscope could digitize data at rates of up to 1 GigaSamples/second. The oscilloscope was set to trigger just before a signal emerged from the sample by using a delay pulse from a Stanford delay generator as the trigger. The delay was set to the time taken for a sound wave to traverse the distance from transducer to hydrophone through water.

To improve the signal-to-noise ratio, it was necessary to average many waveform acquisitions into a single record, each acquisition consisting of data collected for 100 μs after a trigger. Typically the oscilloscope was set to average

1000 waveforms, of 5000 pts each, into a single record. These data were digitized at a rate of 50 MegaSamples/second. Each record we collected corresponded to the diffusing ultrasonic signal collected at a specific point, or speckle, on the sample face.

3.1.8 Stanford Delay Generator

The Stanford delay generator was used in the experiment to delay the response of the oscilloscope to an input pulse. The oscilloscope was set to trigger only after enough time had elapsed for the signal to traverse the distance between the generating transducer and receiving hydrophone. We could set the amplitude and repetition rate and length of the delay pulse.

The delay generator had four channels with each channel operating either independently or in tandem with the others. The instrument could be triggered either externally or internally. For this experiment it was triggered by the pulse controller, and the delays to each channel were referenced to that trigger.

3.1.9 Filters

A number of filters were used to limit noise. These filters were simple low pass or high pass 3, 5, or 7 pole Butterworth filters. For example, when we used a 2.5 MHz pulse as our input signal, a 0.13 MHz high pass filter was placed in the system prior to amplification. In the diffusing acoustic wave spectroscopy experiment, at the input to the oscilloscope, a 2 MHz high pass filter was used in conjunction with a 3 MHz low pass filter to create a bandpass filter configuration.

3.2 Spatial Correlation Study

The apparatus was configured as in the frequency correlation study, and arranged in the plane wave geometry. We used a miniature hydrophone of 200 μm tip diameter as a detector. The sample was a 1.0 cm thick cell filled with 1.0 mm diameter glass beads similar to those used in the acquisition of frequency correlation data

We were interested in determining the size of the individual speckles. To this end we acquired data at 801 positions, scanned transversely across the face of the sample in 0.003 cm increments, for a total displacement of 2.4 cm. We repeated this for a number of these 'lines', with a line separation of 0.1 cm, to collect data weighted by different bead arrangements.

The data were acquired using oscilloscope settings similar to those employed in the acquisition of frequency correlation data; in this case, however, the input waveform was long enough (200 ms) to be considered a continuous wave (cw). Thus all scattering paths were sampled by the scattered wave, and the signal emerging from the sample at a given point was constant in amplitude and phase. At each position the recorded signal was 10 μs long and this signal represented the average of 300 waveforms. The frequency of the input waveform was 2.5 MHz. Two other frequencies were used in this cw configuration to collect data for comparison. These were at 1.5 MHz and 3.5 MHz and were taken from a single 'line' only.

3.3 Temporal Autocorrelation Study (DAWS)

In this portion of the experiment, our goal was to use correlation analysis of diffusing sound to learn about the behavior of particles in motion. The sample no longer consisted of static scatterers in a disk shaped cell but was a fluidized bed with the scatterers in motion. The paths taken by the ultrasound before emerging from a point in the sample were subject to temporal variations.

Rather than detect transmitted sound at different points in the sample to investigate statistically independent bead distributions, we only needed to gather data from a single point to be able to gain information regarding particle dynamics, since the temporal fluctuations of a single speckle contained the requisite information. This is justified since we were able to observe variations in the intensity of the detected sound emerging from the sample at a specific point as the beads moved about, analogous to examining bright and dark speckles in a static scatterer experiment.

Three methods of measuring temporal fluctuations of the scattered sound were employed, requiring two slightly different apparatus configurations. In this section, we outline the three collection methods and their individual strengths, then describe the general configuration and operation of the equipment. Within this overview we also highlight the differences in set-up for each acquisition method and give detailed explanations of components not discussed previously in the frequency correlation study.

3.3.1 Acquisition methods

1. In the first method the incident sound consisted of short pulses, of width much shorter than time required to diffuse through the sample. This approach could only be used when the particle dynamics were relatively slow since our apparatus limited the rate at which we could send an input signal. We were able to take advantage of the better signal to noise characteristics and higher power levels available to a short pulse incident waveform. Using short pulses allowed us to focus on sound that had traversed specific pathlengths within the sample, simplifying the form of the temporal autocorrelation function used to determine the scattering particle motion.
2. In the second method incident sound was also short pulse, but the temporal fluctuations of the multiply scattered ultrasound could be measured for much faster particle dynamics. This was achieved by using a boxcar integrator to sample the detected field in a narrow, 30 ns, time interval. We chose the interval to be much smaller that the ultrasonic period so that the detected sound field was essentially constant over the sampling interval, allowing the boxcar to accurately measure the true sound field. Using this method, we acquired the scattered signal from consecutive pulses whose repetition rate could be increased up to the fundamental limit imposed by the amount of time taken for sound to diffuse through the sample, typically 50 to 100 μs, depending on the sample thickness. This method did not allow us to measure the phase and amplitude of the field independently but we were able to calculate the field autocorrelation function from the data.

3. The third acquisition method used incident sound which consisted of very long pulses. The pulse width was greater than the time required for sound to diffuse through the sample. We then detected the variations in the scattered sound field caused by the motion of the scattering particles. This approach, which we refer to as quasi-continuous-wave (cw), allows us to measure the particle dynamics on time scales which range between the ultrasonic period (tenths of a microsecond) and several milliseconds. The upper limit is set by the maximum record length of the digitizing oscilloscope (50 000 pts) and the requirement that the maximum time interval per point be considerably less then the period of the wave in order to measure the field correctly. The cw method is most suitable for investigating rapid dynamical processes on fast timescales.

3.3.2 Overview of Apparatus

A block diagram of the experiment showing all of the apparatus used in the three acquisition methods is shown in Fig. 3.8. The dashed lines in the figure indicate apparatus that was added for use in method 3.

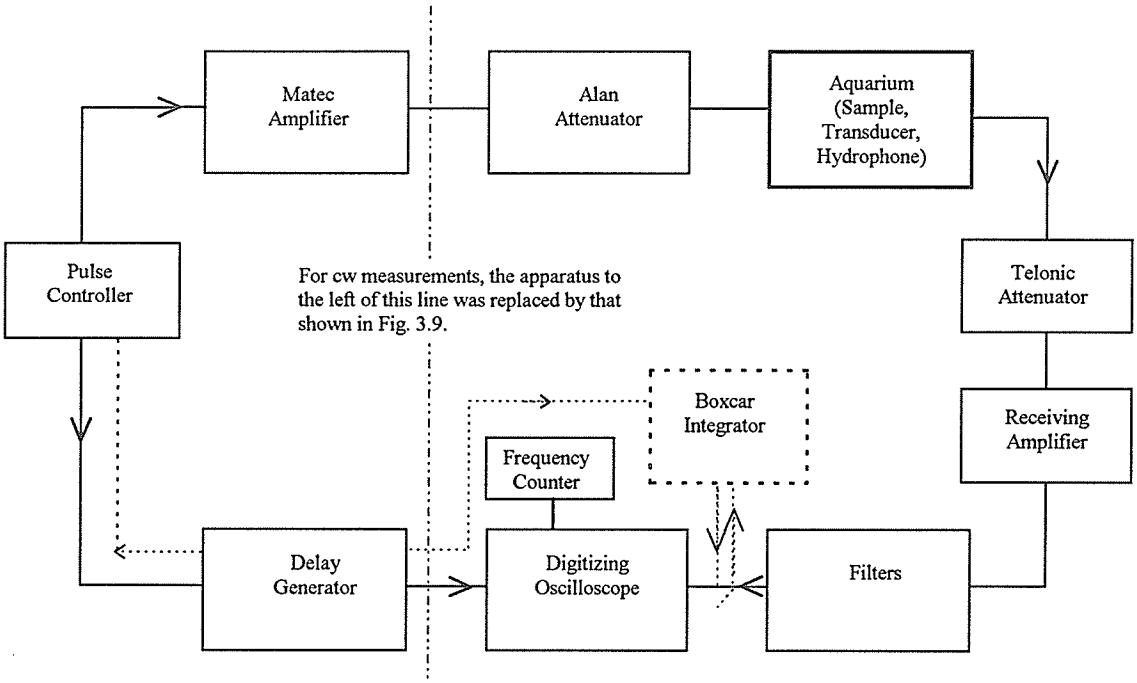

Figure 3.8. Block diagram of diffusing wave apparatus.

A pulse train was generated by the Matec amplifier; the width of each pulse and their repetition rate controlled by the pulse controller. The Alan attenuator, which attenuates in 1 decibel increments between 0 and 42 dB, reduced the signal before it was converted to an acoustic pulse by a focusing transducer. In order not to overdrive the transducer it was imperative to have at least 12 decibels of attenuation in the Alan attenuator. The sound waves then diffused through the sample and were detected on its opposite side by a small-diameter hydrophone. This signal was attenuated by the Telonic attenuator in order to prevent large signals from overdriving the amplifier at the next stage. The signal was amplified and filtered to remove noise caused by the electronic equipment, and then was digitized and stored in the oscilloscope. We used a frequency counter to count the

rate at which the oscilloscope was triggering. This allowed us to check that the response to each input pulse was recorded and thus no trigger inputs were being missed due to duty cycle limitations of the oscilloscope.

For the second acquisition method we used the boxcar integrator to sample sound at a specific instant in the diffusion profile. The apparatus set up is as in Fig. 3.8, with signal paths indicated by the short dash line. We used the Stanford delay generator to set the pulse repetition rate and to trigger the boxcar integrator which was inserted into the circuit so that the signal was input to the boxcar after the receiving amplifier. By doing things this way we were able to ensure the oscilloscope, the boxcar and the pulse amplifier were triggered synchronously, and that the oscilloscope trigger was synchronized with the pulse repetition rate. The boxcar output was sent to the oscilloscope to be digitized and stored.

For the third acquisition, where we used a quasi–continuous wave input signal, we altered the above circuit in the manner outlined in the following diagram.

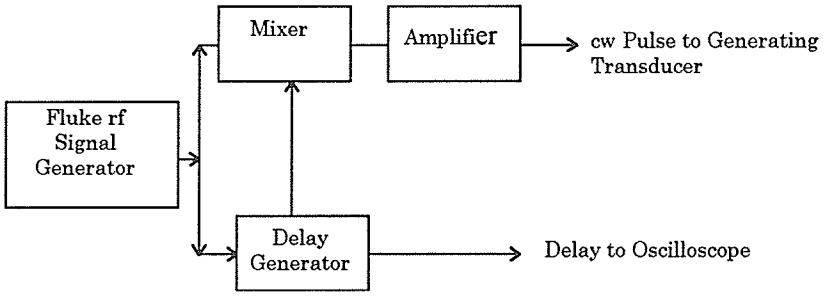

Figure 3.9. Electronics used to generate cw input signal.

This apparatus replaced the equipment to the left of the vertical dashed line in Fig. 3.8. The Fluke rf signal generates a continuous wave which is gated with a

200 ms gate pulse from the delay generator and is then sent to the mixer. The mixer combines the gate pulse with the cw signal and outputs a quasi-cw pulse to the transducers and on through the sample. The delay generator also sends a delay to the oscilloscope, which triggers it to begin an acquisition.

The sample, discussed in the next section, consisted of monodisperse glass beads of 0.5 mm diameter in a glycerol and water solution. This solution flowed through the sample raising the beads.

3.3.3 Fluidized Bed

The fluidized bed used to suspend the beads in the glycerol and water solution is shown in Fig. 3.10.

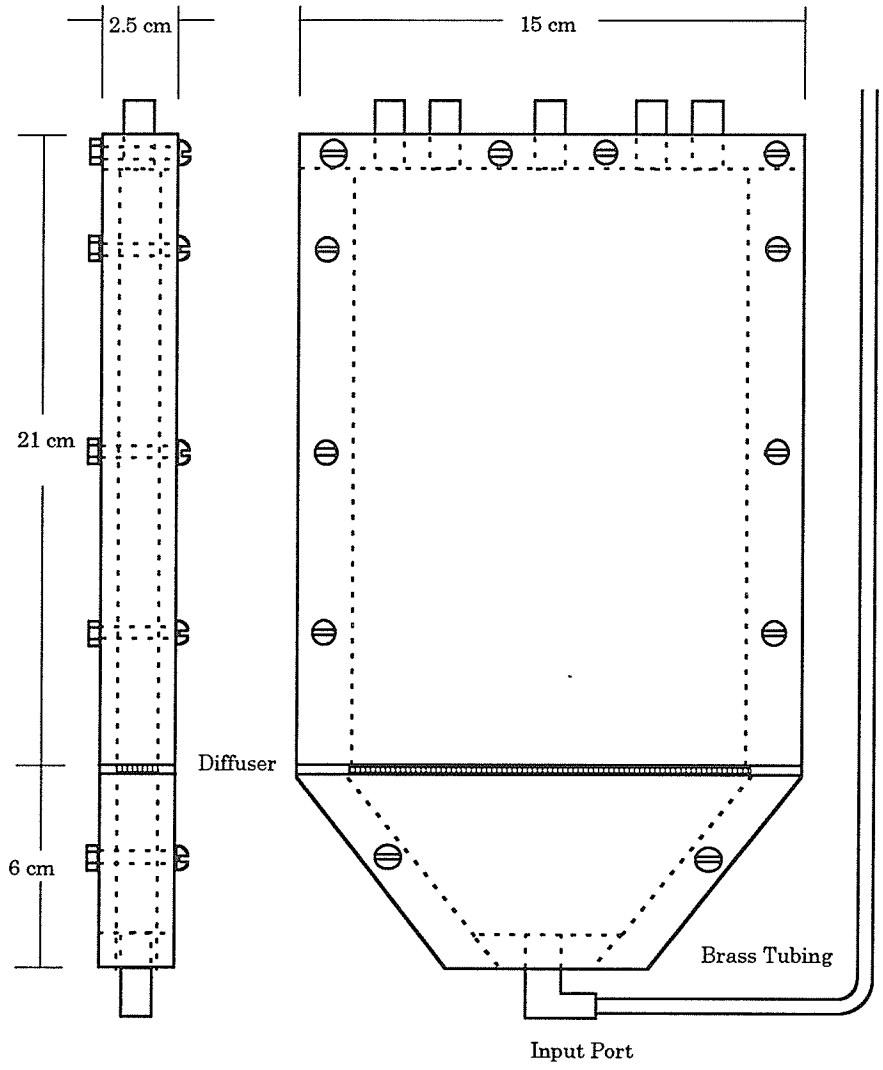

Figure 3.10. Fluidized bed.

Glass beads were contained in the rectangular portion of the bed above a diffuser plate. Initially these beads settled under gravity to a bead density in the range 0.6 to 0.63 [1] in a randomly close-packed configuration. The diffuser, Fig. 3.11, distributed the flow of fluid evenly across the bottom of the portion of the bed containing the beads.

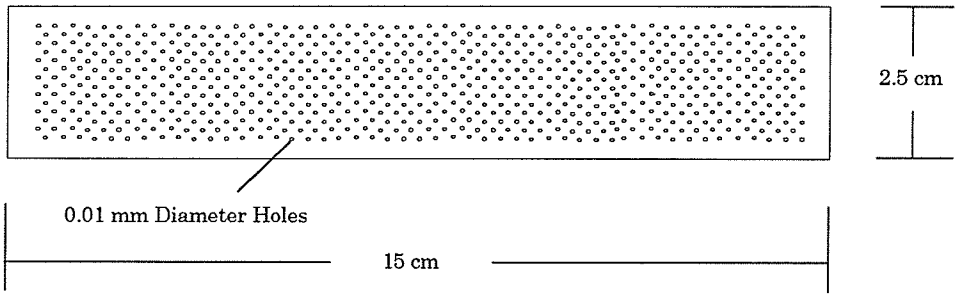

Figure 3.11. Plan view of diffuser.

The diffuser was constructed from hard polystyrene of thickness 3 mm and the holes were evenly spaced ~ 1 mm apart. The diffuser was held in place by means of grooves in the inside faces of the cell, making it easy to remove whenever it became necessary to clean blocked holes.

The faces of the cell were cut from sheets of clear Acrylite of thickness 6.35 mm. A groove was cut into the perimeter of each face into which an o-ring was fixed which sealed the face to a stainless steel midsection. The midsection of the cell was machined from a stainless steel sheet, 13 mm thick. This stainless steel 'ring' was tapped to accept 0.5 inch brass pipe fittings, five at the top and one at the bottom. The fluid entered the cell via the bottom fitting and exited through the five ports at the top. The pipe fittings coupled to 0.25 inch polyflow tubing at the exit ports and 0.25 inch brass tubing at the bottom entry point. The faces and midsection were held together by clamping them between 6 mm thick stainless steel outer rings that were fixed together with stainless steel bolts.

The fluid was pumped through the cell using an ordinary drill pump, which accelerated the fluid between an external reservoir and the cell. Fluid exiting the cell was returned to this reservoir. The drill pump was connected to a Bodine

Electric Company variable speed motor. This motor was a 1/8 Hp, 115 volt, 1.2 amp motor with a maximum of 1725 rpm. We used it in conjunction with a 20:1 step-down gear. The maximum speed at which the drill pump could revolve was then 86 rpm. We were able to vary the speed from barely turning to maximum rpm in a continuous manner using a control panel dial and, in this manner, control the flow rate of fluid through the system.

Initially we intended to use water as the fluid; however, we found that to keep the beads suspended required too great a flow rate, causing bead dynamics that were far too fast to accurately measure using our technique. We decided to use a more viscous fluid to slow the bead dynamics down while still allowing them to be suspended against sedimentation. Glycerol was chosen as it was readily available, had a high viscosity relative to water, was not so absorbing to ultrasound that we would lose the signal, and was soluble in water. Initially the fluidized bed was tested using a 100% glycerol solution. This worked extremely well at raising the beads, in fact it worked too well since we were unable to turn the drill pump slowly enough to prevent the beads from flowing out the exit ports of the cell. A solution of 90% glycerol to 10% water was then tried and found to be effective. At this density, it was possible to raise the beads and control their behavior. We then varied the percentage of glycerol and flow rate in order to obtain data from a variety of viscosities and bead densities.

When the pump started, the settled beads responded by moving upwards from the diffuser in a single group, or slug. After a short time, the single slug broke up into many smaller slugs. These also disintegrated in time until the beads were

distributed evenly over the volume of the cell with no apparent differences in occupied volume fraction. By varying the flow rate, we could vary this volume fraction.

3.3.4 Aquarium

In this experiment the water, transducer, sample and hydrophone were contained in an 82 litre aquarium as shown in Fig. 3.12.

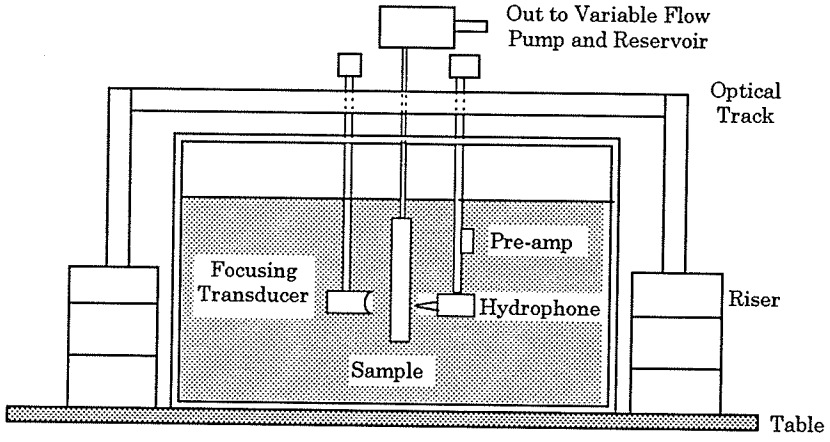

Figure 3.12. Aquarium arrangement for diffusing wave study.

The aquarium was lined with 2.2 mm cork sheet to attenuate reflected signals from the walls. To this end there were also 2.54 cm Styrofoam ribs spaced vertically on the side walls, and horizontally across the bottom. The sample was connected to a longitudinal translation stage which was moved with a micrometer having a resolution of 0.01 inch and a maximum travel of 1 inch. The fluid reservoir and pump were placed outside of the aquarium, level with the top. The transducer had a focus of 5.7 cm, and was placed 5.3 cm from the face of the sample. This

focused sound to a point on the boundary between the beads and cell wall. The hydrophone was placed within 2 mm of the opposite face of the sample. When the beads were in motion, they covered an area of between 143 and 234 cm^2 in a vertical plane within the sample, depending on flow rate and viscosity. We endeavored to place the hydrophone and focus of the transducer at the center of this rectangular area of beads.

3.3.5 Boxcar Integrator

We used a Princeton Applied Research Model 160 high resolution Boxcar Integrator in the experiment. In its normal mode of operation, it extracts synchronous waveforms from noisy repetitive signals by means of a sampling and averaging process. The integrator functions by first using a variable delay, variable–width gate to select a portion of an input signal. The gated signal is then normally averaged by variable time constant integrators whose output is the average of some number of repetitions of the input signal over the gate width interval. This averaging procedure ensures an improved signal to noise ratio, since random noise will average to a minimal level. In this experiment, the averaging mode was essentially disabled by setting the time constant to 10 ns; this limited the averaging to only 5 sequential samplings of the input signal. The gate can either be scanned across or fixed at a point in the input waveform. When the gate is fixed to a point on the input signal, as in this experiment, the boxcar output rises toward the amplitude of the input waveform at the sampled point.

By setting the gate width to 30 ns, we were able to use the boxcar to select a portion of the input waveform whose duration was less than the period of the waves (400 ns), allowing the scattered field to be accurately measured at a particular point on the diffusion profile.

3.3.6 Oscilloscope

For the first data acquisition method, we used a segmented memory mode on the oscilloscope to enable us to concatenate the response to many trigger pulses into a single record length. We instructed the oscilloscope to collect a set number of points after a trigger; this is called a frame. We also instructed the oscilloscope to acquire a set number of frames which it then concatenated into a single record.

For example; the maximum number of points the oscilloscope can acquire in a single record is 50 000, and this can be divided up into 1000 frames of 50 points each. If we sample at 50 MS/s, each frame is a 5 μs long record of the response to an input pulse. If the oscilloscope is triggered every 20 ms, a single record will contain information about the bead motion over 20 seconds. We can vary the amount of time between triggers and can thus examine the bead motion over different timescales. This method overcomes the prohibitively long time taken to download a waveform from the oscilloscope to the computer over an IEEE bus, which would limit the rate at which the scattered field could be sampled to fewer than 1 sample per second. This was too slow to investigate the dynamics in many systems.

We set a delay between the time a sound pulse was generated by the transducer and the trigger pulse of the oscilloscope. The oscilloscope did not trigger

until after a portion of signal had gone through the sample. Thus we could focus on any 5 μs portion of the scattered signal in each frame, and look at different time scales of the fluctuations in different portions of the diffusive profile.

For the second acquisition method, we used the oscilloscope in its regular mode to capture and digitize the output signal from the boxcar integrator. In this case the record length was the maximum possible of 50 000 pts. Each point represented an individual response from the boxcar integrator to an input signal. The key to this method was in the synchronization of oscilloscope and boxcar integrator outlined earlier.

As the third acquisition method utilized a cw input waveform, the scattered signal did not exhibit the fluctuations seen when a short pulse is used but was relatively flat for all time that waves were incident on the sample. Any fluctuations in the scattered signal were due to the bead motion. The oscilloscope was set to acquire data in the same fashion as explained above for method 2.

3.4 References

[1] G.D. Scott, *Nature* **188**, (1960) 908.

4. EXPERIMENTAL DATA AND ANALYSIS

In this section we present the experimental results and discuss the analysis used to interpret them. We begin with the frequency correlation study, presenting first a general discussion of how the correlation functions were determined, and then present specific results from the studies done in the point source and plane wave geometries. We then discuss the results from the spatial correlation study, again introducing the section by discussing the calculations leading to the correlation functions. Finally we present the results of the temporal autocorrelation study, within which the results from each of the three data acquisition methods are discussed separately.

4.1 Frequency Correlation Study

In the experiment we measured the sound field transmitted through a sample of random static scatterers, at a number of independent speckles, for samples of various thickness. The transmitted signal, $F_T(t)$, in a given speckle is actually the sum of the scattered signal $F(t)$, plus an unscattered component which we call the ballistic signal. This ballistic signal is a remnant of the incident pulse $I(t)$, that propagates through the sample without scattering [1] and has the same phase coherence for each speckle. To extract the ballistic signal from the measured waveform we average the transmitted signals from all speckles together and subtract the resulting averaged waveform from each speckle. The effect of the averaging process is to isolate the unscattered component since the scattered signal in independent speckles have random phases and tend to cancel, while the unscattered ballistic signal is unaffected by averaging. The unscattered component can then be removed from the individual transmitted fields before calculating the correlation function. The scattered fields are then given by

$$F(t) = F_T(t) - \langle F_T(t) \rangle_{(ensemble\ average)}, \tag{1}$$

where the ballistic component is given by the second term on the right hand side. Because the ensemble average is confined to a limited number of speckles, there is always the possibility that a small remnant scattered signal would persist after ensemble averaging. To ensure that this was not a problem, we took advantage of the temporal resolution between the ballistic pulse and the bulk of the scattered

fields to limit the averaged wave, $\langle F_T(t) \rangle$, to early times where there is only ballistic signal, before subtracting it from the transmitted signal. The ballistic component is a larger component of the transmitted signal for thinner samples, and becomes comparable to the amplitude of the scattered field in the thinnest sample studied. In thicker samples however, the ballistic component has minimal contribution to the transmitted signal. Examples of the incident, $I(t)$, transmitted, $F_T(t)$, averaged, $\langle F_T(t) \rangle$, and scattered signals, $F(t)$, for two thicknesses are shown in Fig. 4.1. The incident pulse is shown on the left panels Figs. 4.1 (a),(e). It consists of two oscillations with a pulse width of about 1 μs, and a frequency bandwidth ranging from 1 to 4 MHz; in the plot the input pulse is normalized to a peak value of unity. The transmitted signals Figs. 4.1 (b),(f), shown in the right panels, extend over many microseconds, and undergo rapid fluctuations in phase and amplitude as result of the interference of waves traveling different scattering paths. These transmitted signals are an order of magnitude or more smaller in amplitude than the input signal, as a result of the very strong scattering. The time axis on the plots is set so that the input pulse impinges on the sample at time $t = 0$, with the delay in the transmitted signal arising from the time taken for the signal to travel through the sample. The 3.24 mm sample has a large unscattered component at early times that is shown in the averaged waveform Fig. 4.1 (c) to be a significant fraction of the scattered signal, Fig. 4.1 (d), for this thickness. In contrast the 10.17 mm sample shows a ballistic signal, Fig. 4.1 (g), which is a tiny portion of the scattered signal, Fig. 4.1 (h), since it is exponentially attenuated with increasing thickness.

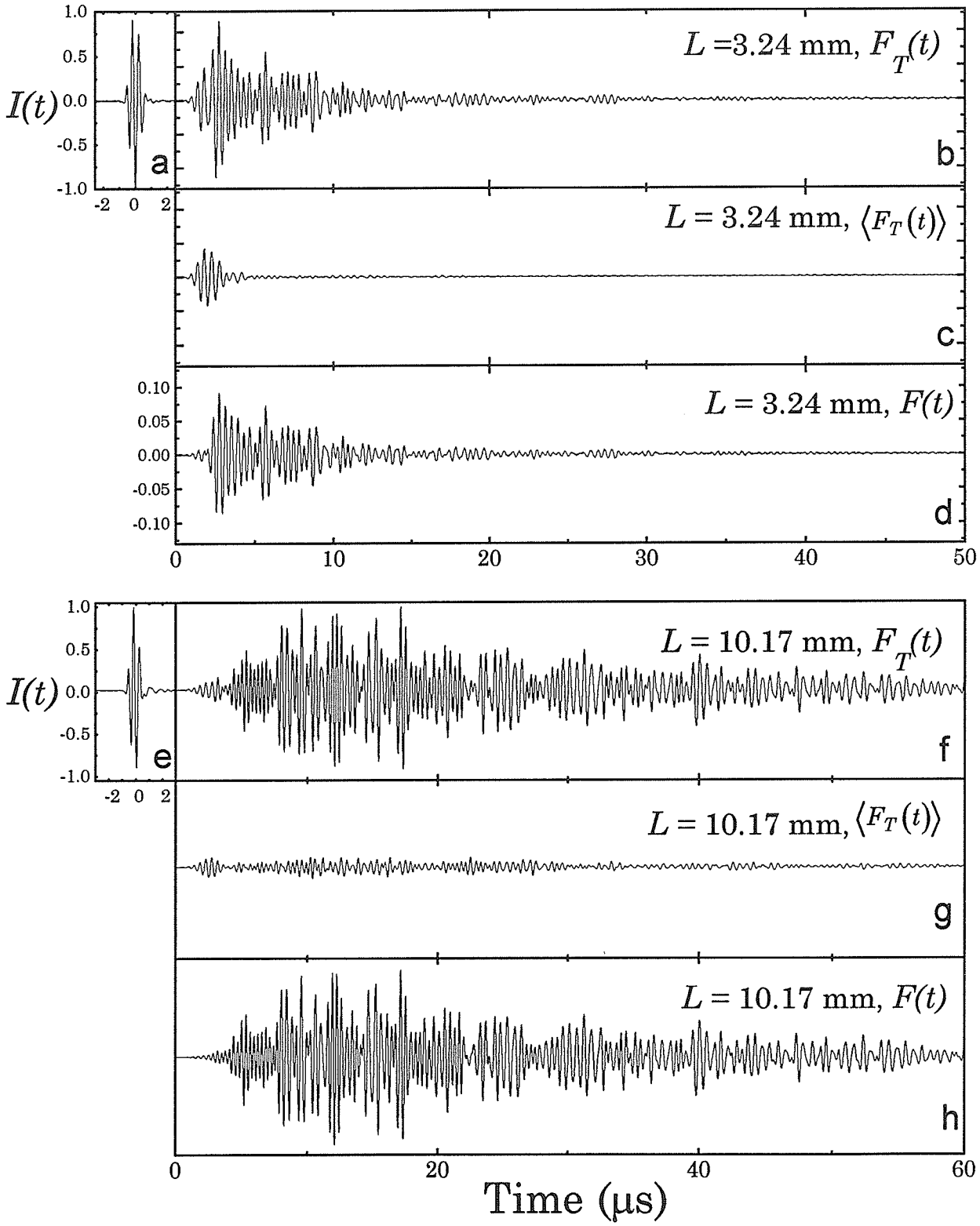

Figure 4.1. Input pulses along with the signal transmitted through samples of two thickness. Input pulses are normalized to unity, all transmitted signals are shown with the same vertical scale to demonstrate the degree of attenuation of the medium, and the relative size of ballistic signal to the scattered and transmitted signals.

To determine the correlation function from the scattered signals we first calculate the complex Fast Fourier Transform (FFT) of each record. We then FFT the input waveform and determine the response function of the medium, $R(\nu)$,

$$R(\nu) = {}^{F(\nu)}\!/_{I(\nu)} \tag{2}$$

where $F(\nu)$ is the FFT of the transmitted scattered waveform, $F(t)$, and $I(\nu)$ is the FFT of the input waveform, $I(t)$. This response function renormalizes the scattered signal to account for different relative amplitudes of different frequency components contained in the input signal. In Figs. 4.2 and 4.3 we show the magnitudes of the FFTs of the data presented in Fig. 4.1. Fig. 4.2 shows $F(\nu)$, $I(\nu)$ and $R(\nu)$ for the 3.24 mm sample and Fig. 4.3 shows $F(\nu)$, $I(\nu)$ and $R(\nu)$ for the 10.17 mm sample. We see from the two sets of figures that, with equal frequency weighting, the response to the input signal will have more rapid fluctuations for a thicker sample.

The frequency correlation function is then calculated from the response function

$$\begin{aligned} g(\Delta\nu) &= \frac{1}{g(0)}\int R(\nu)R^*(\nu+\Delta\nu)\,\mathrm{d}\nu \\ &\approx \frac{1}{g(0)}\sum_{j=0}^{n-i-1}\frac{R(\nu_j)R^*(\nu_j+\Delta\nu_i)}{n-i}, \end{aligned} \tag{3}$$

where n is the total number of data points in the frequency range from ν_0 to ν_n over which the correlation function is calculated, $\Delta\nu = \Delta\nu_i = i\delta\nu$ is the frequency shift, and $\delta\nu$ is the frequency interval between adjacent points in the FFTs. The factor

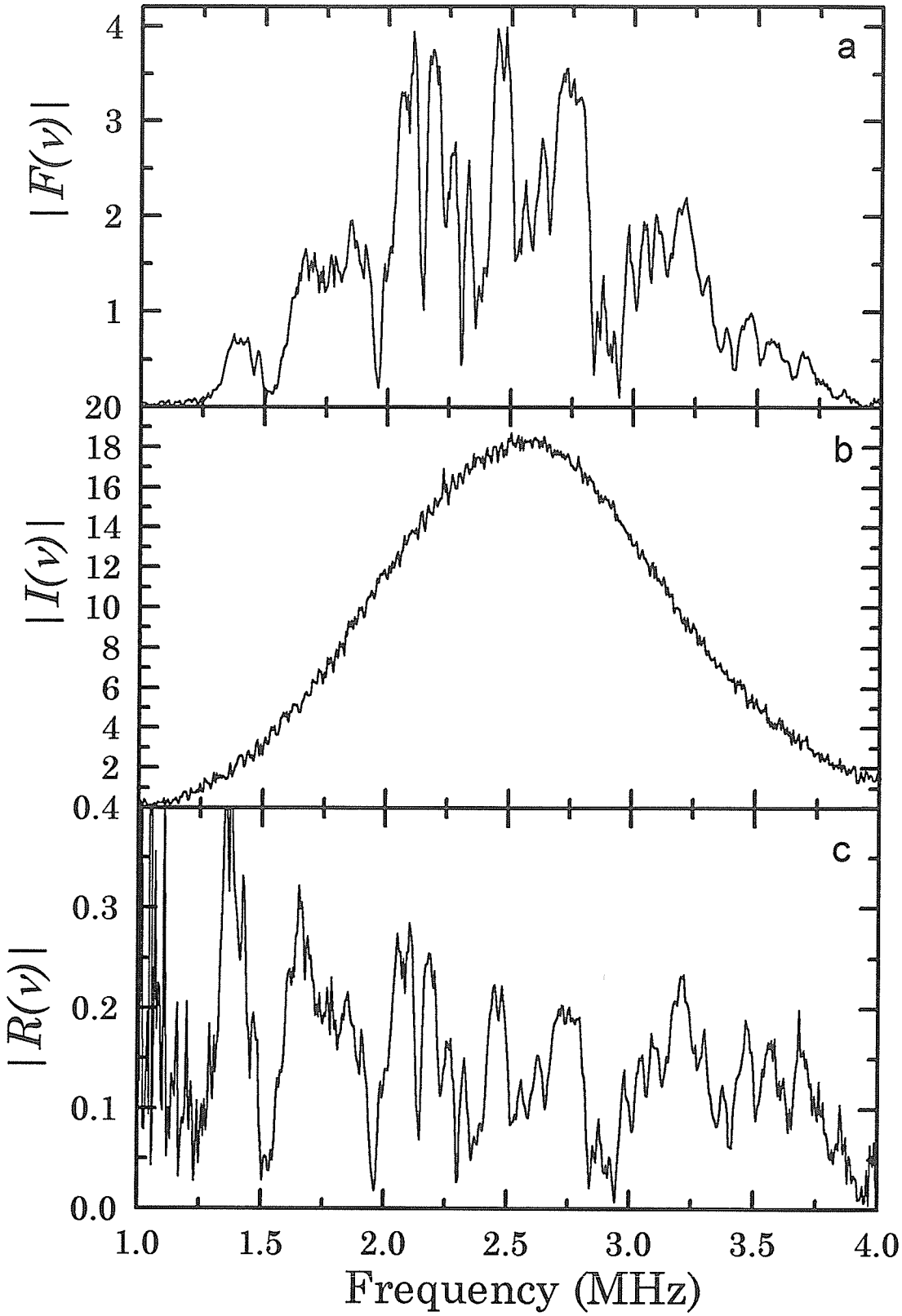

Figure 4.2. Response function for $L = 3.24$ mm sample.
The FFTs of the scattered signal and input pulse are also shown.

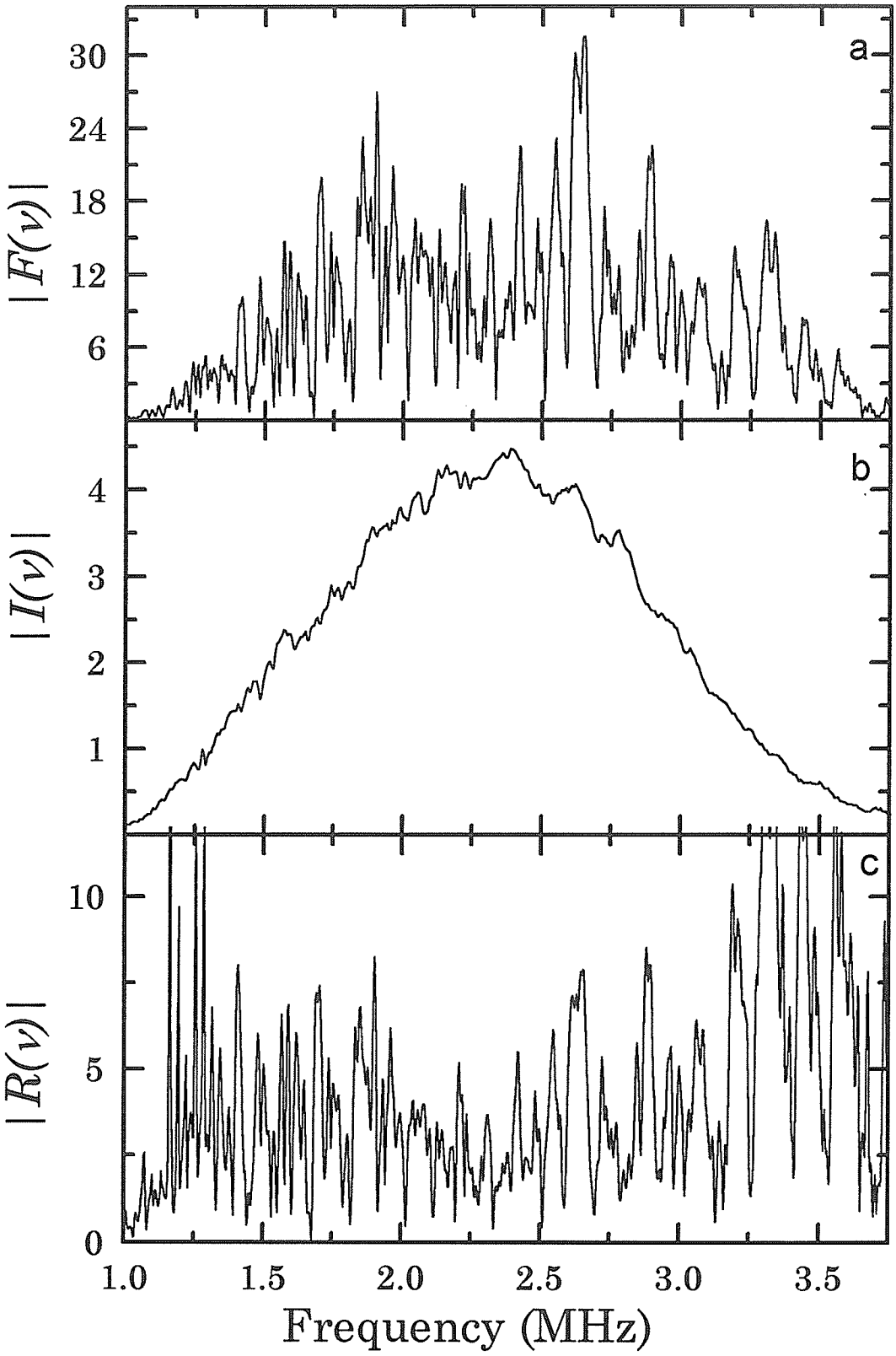

Figure 4.3. Response function for $L = 10.17$ mm sample.

$1/g(0)$ is the correlation function evaluated at $i = 0$ and ensures that the correlation function is normalized to unity at zero frequency shift. We ensemble average $g(\Delta\nu)$ over all of the independent speckles from which data were acquired and then compare $|g(\Delta\nu)|$ with the theoretical expressions developed in Chapter 2.

4.1.1 Point Source Geometry

The results for five samples ranging in thickness from 1.9 to 25 mm are shown in Fig. 4.4. These data were acquired using the focusing transducer of central frequency 2.5 MHz and the correlation functions were calculated for a frequency range of 2–3 MHz, a range in which the majority of the input signal is contained (see Figs. 4.2 and 4.3). We see that the correlation function decays more rapidly as the sample thickness increases.

To quantitatively evaluate these data, we wish to compare them to theoretically predicted correlation functions. As there is no analytical expression for $g(\Delta\nu)$ in the point source geometry, we first calculate the diffusion time profile $J(t)$ and FFT it to obtain the correlation function. An example of this is shown in Fig. 4.5, where the left panel indicates the time profile for diffusion through a 10–mm–thick sample, and the right panel shows the magnitude of FFT of that profile, or $g(\Delta\nu)$. The parameters used in the calculation of $J(t)$ are D, l^*, τ_a, and L. The best values of these parameters have been determined previously by fitting the diffusion time profile, and at the central frequency of 2.5 MHz their values were found to be D = 0.43 mm^2/μs, τ_a = 12 μs, and l^* = 0.8 mm [2]. In Fig. 4.6 we show theoretical

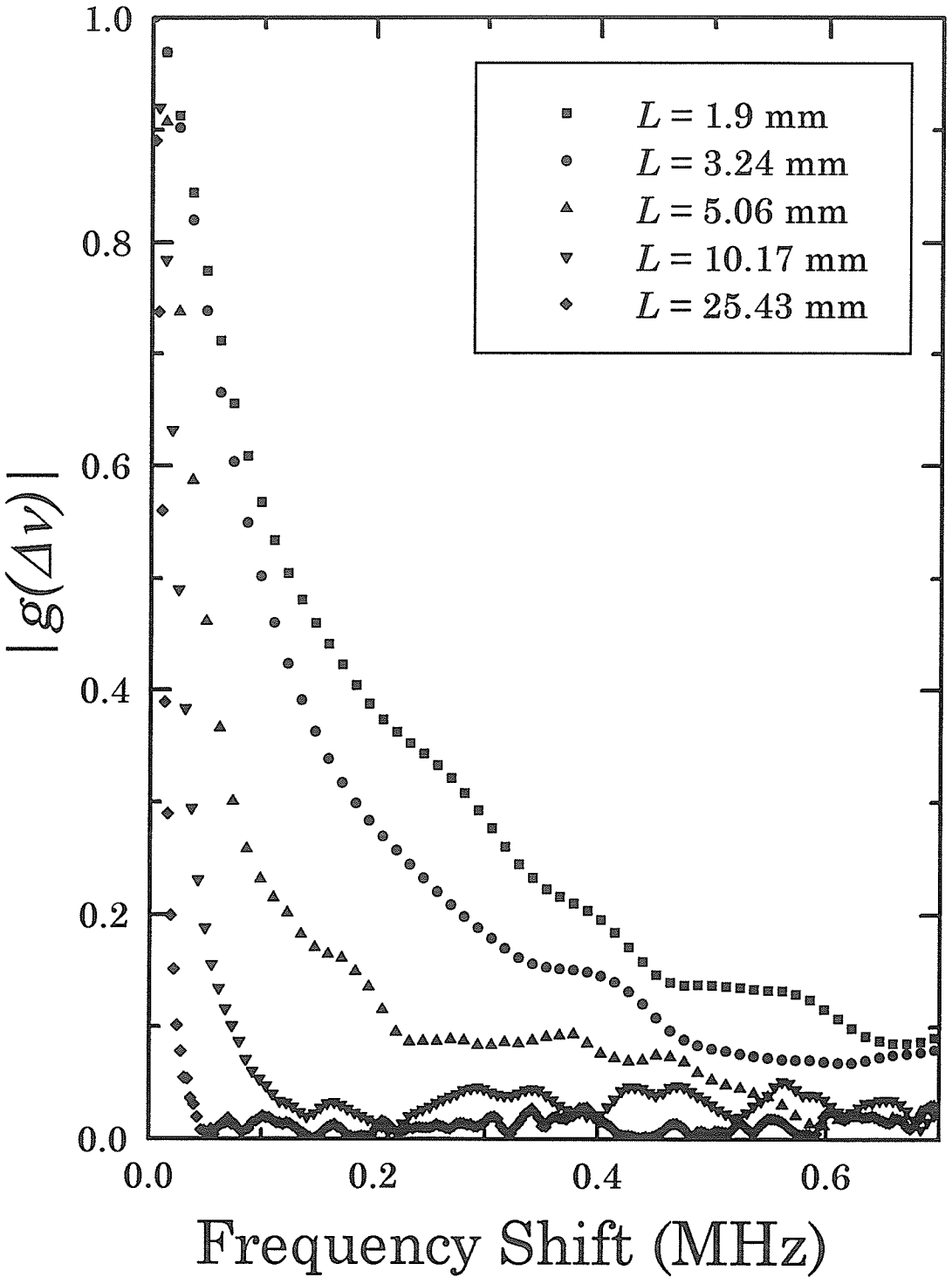

Figure 4.4. Correlation functions for five sample thicknesses measured from 2 to 3 MHz using a focused incident beam.

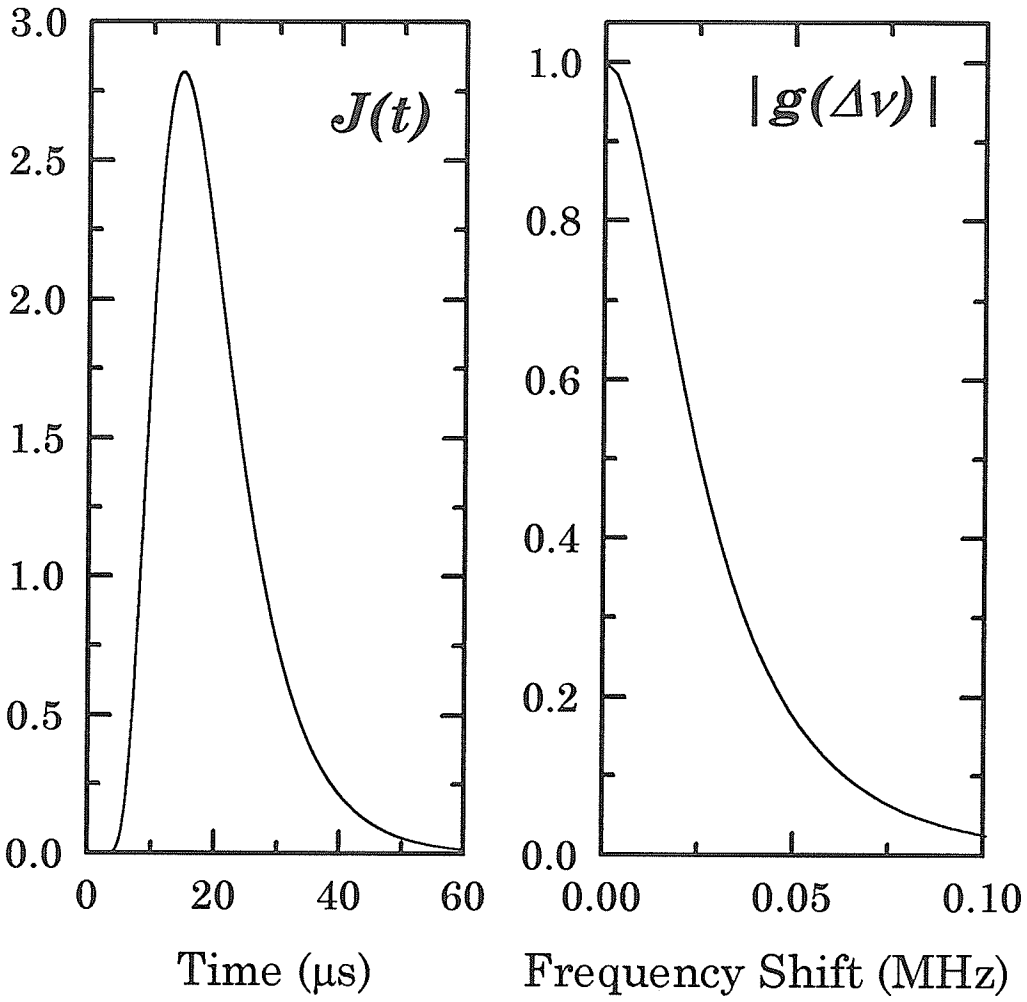

Figure 4.5. Diffusion profile, $J(t)$, for transmission through a 10 mm slab of scattering particles, and its FFT, the frequency correlation function, $|g(\Delta\nu)|$. Arbitrary units.

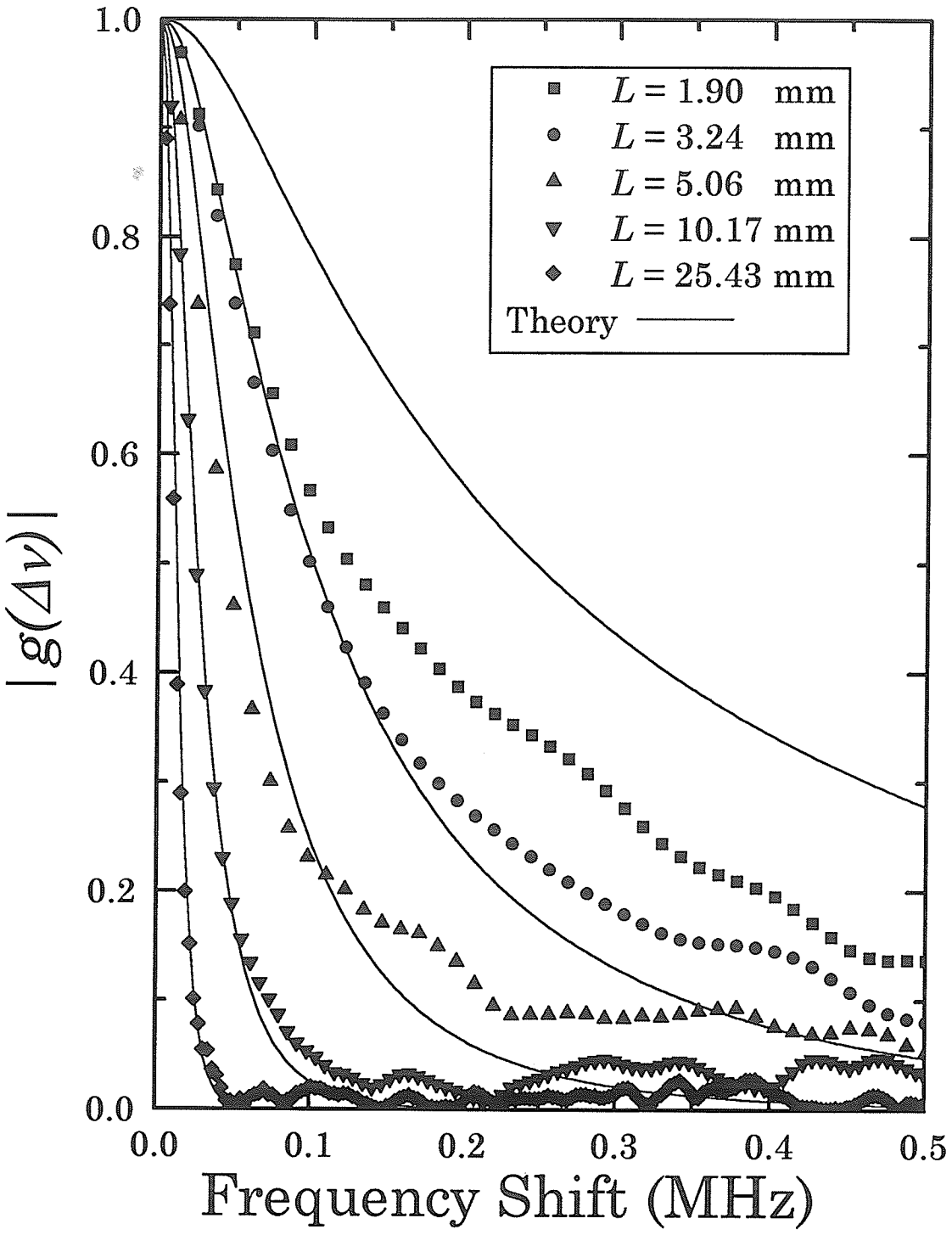

Figure 4.6. Correlation functions from 2 to 3 MHz using a focused incident beam. Also shown are theoretical curves which have been calculated using diffusion theory with $D = 0.43$ mm^2/μs, $\tau_a = 12$ μs, and $l^* = 0.8$ mm.

correlation functions for $g(\Delta\nu)$, calculated using these values, overlaid on the data of Fig. 4.4. These theoretical correlation functions were calculated in the diffusion approximation using the above parameter values. The theoretical curves agree well with the data for all but the thinnest sample at this frequency range. In this thin sample the pulse propagation is mostly ballistic with only a small amount of scattering occurring and we do not expect diffusion theory to provide a good description of the data in this regime.

Because the input signal had bandwidth of 1 to 4 MHz, we have also determined the correlation functions from the data for the 1–2 MHz, 3–4 MHz and 1.2 to 3.8 MHz ranges. These are shown in Figs. 4.7, 4.8 and 4.9 where data for only three thicknesses, a thin L = 3.24 mm, medium L = 9.96 mm, and thick L = 25.43 mm, are plotted. We see that the correlation functions decay much more rapidly for the lower frequency range, possibly indicating a frequency dependence in the parameters D and τ_a. To compare the theory with the data for these frequency ranges we have calculated theoretical curves for each frequency range, as shown in Figs 4.7, 4.8, and 4.9. The parameters used for the 1–2 MHz range were D = 0.29 $mm^2/\mu s$, τ_a = 40 μs, and l^* = 0.8 mm, while for the 3–4 MHz range they were D = 0.35 $mm^2/\mu s$, τ_a = 8 μs, and l^* = 0.8 mm; these values were the results of fitting to time profile data [3,4]. The theoretical predications fit quite well for the medium and thicker samples in all frequency ranges but as the sample thickness decreases to the point where it becomes only a few mean free paths the agreement is not as good.

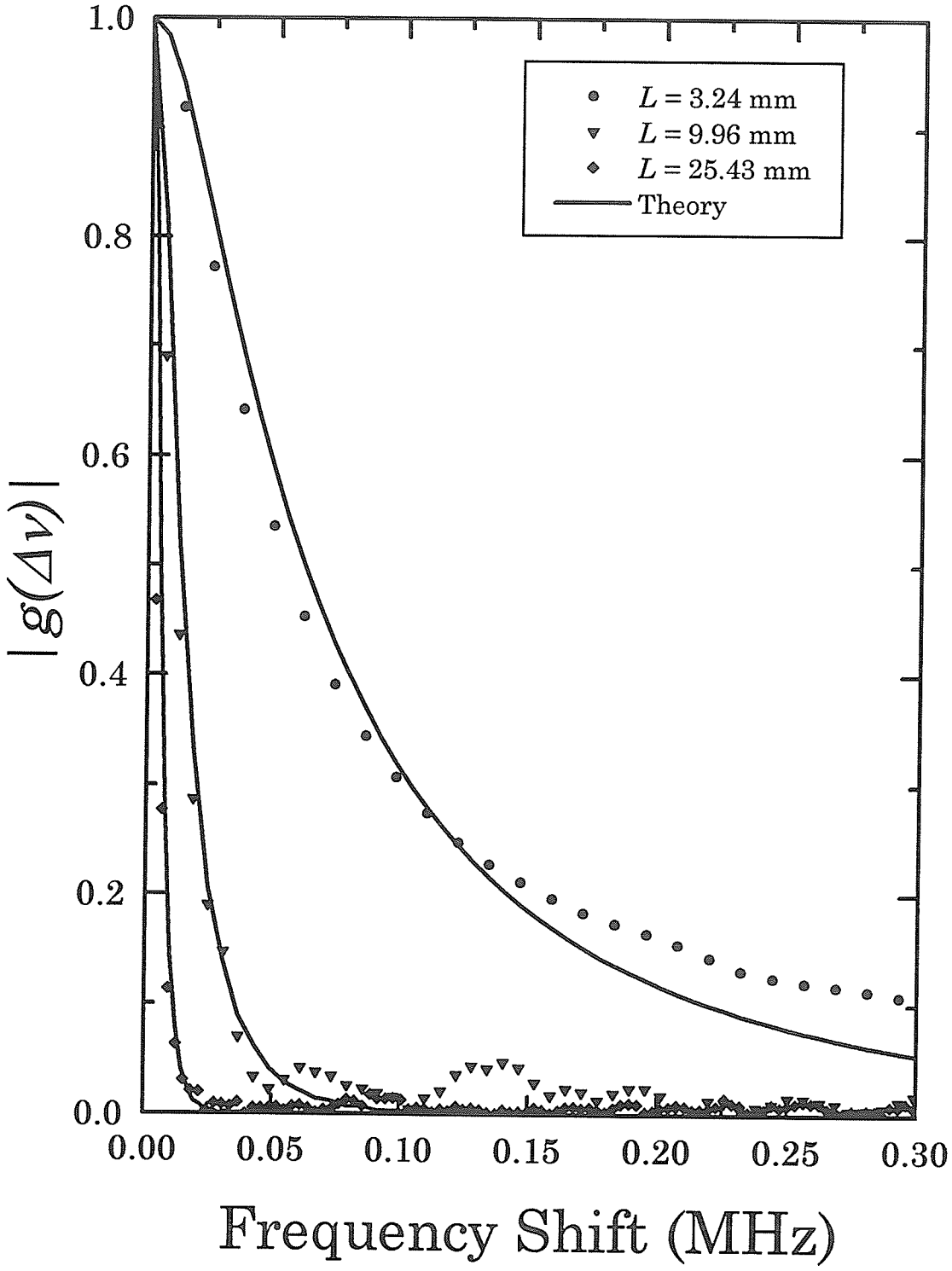

Figure 4.7. Correlation functions measured from 1 to 2 MHz using a focused incident beam. The theory curves are calculated using diffusion theory with D =0.29 mm^2/μs, τ_a = 40 μs and l^* = 0.8 mm.

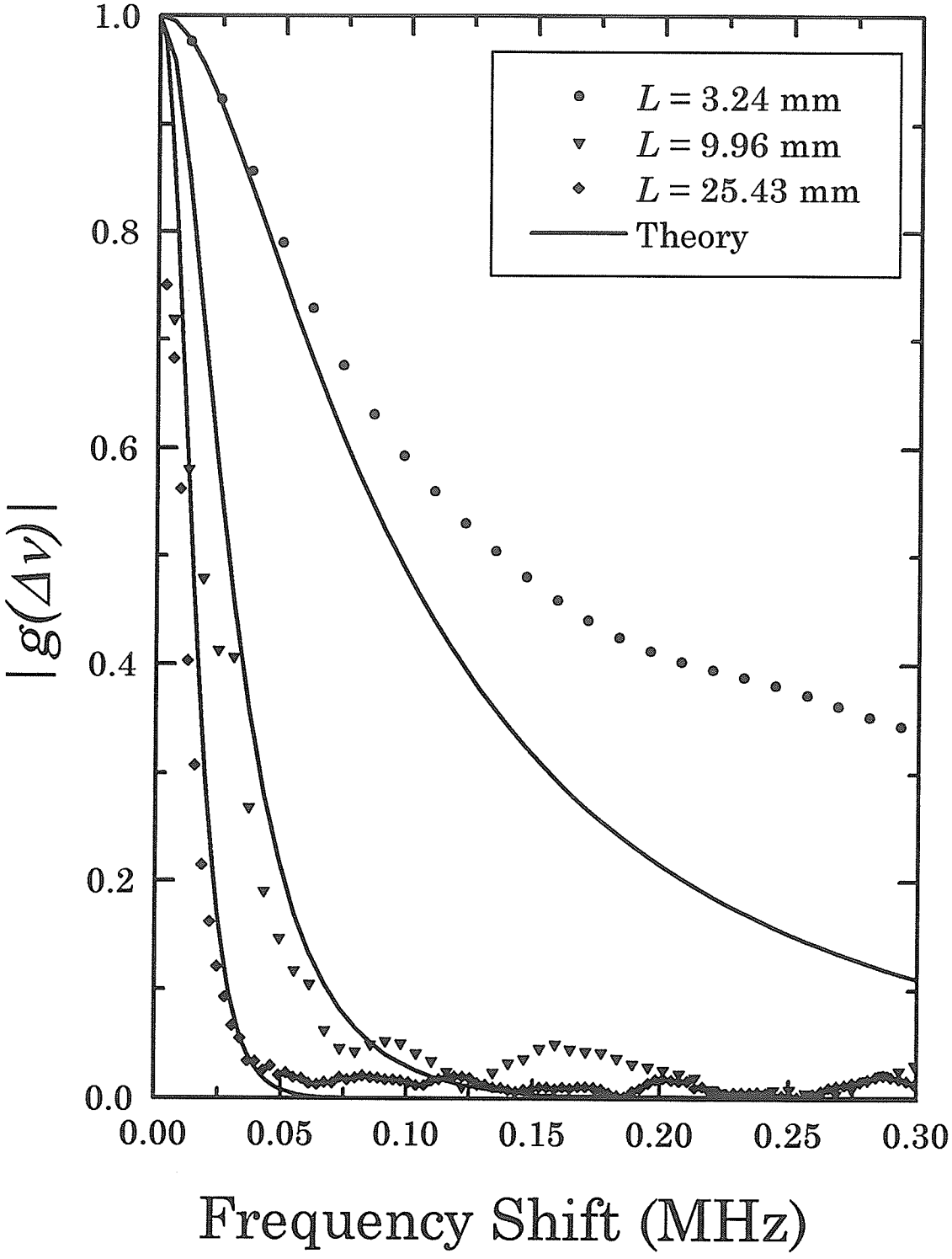

Figure 4.8. Correlation functions measured from 3 to 4 MHz using a focused incident beam. Theory curves are calculated using diffusion theory with $D = 0.35$ mm^2/μs, $\tau_a = 8$ μs and $l^* = 0.8$ mm.

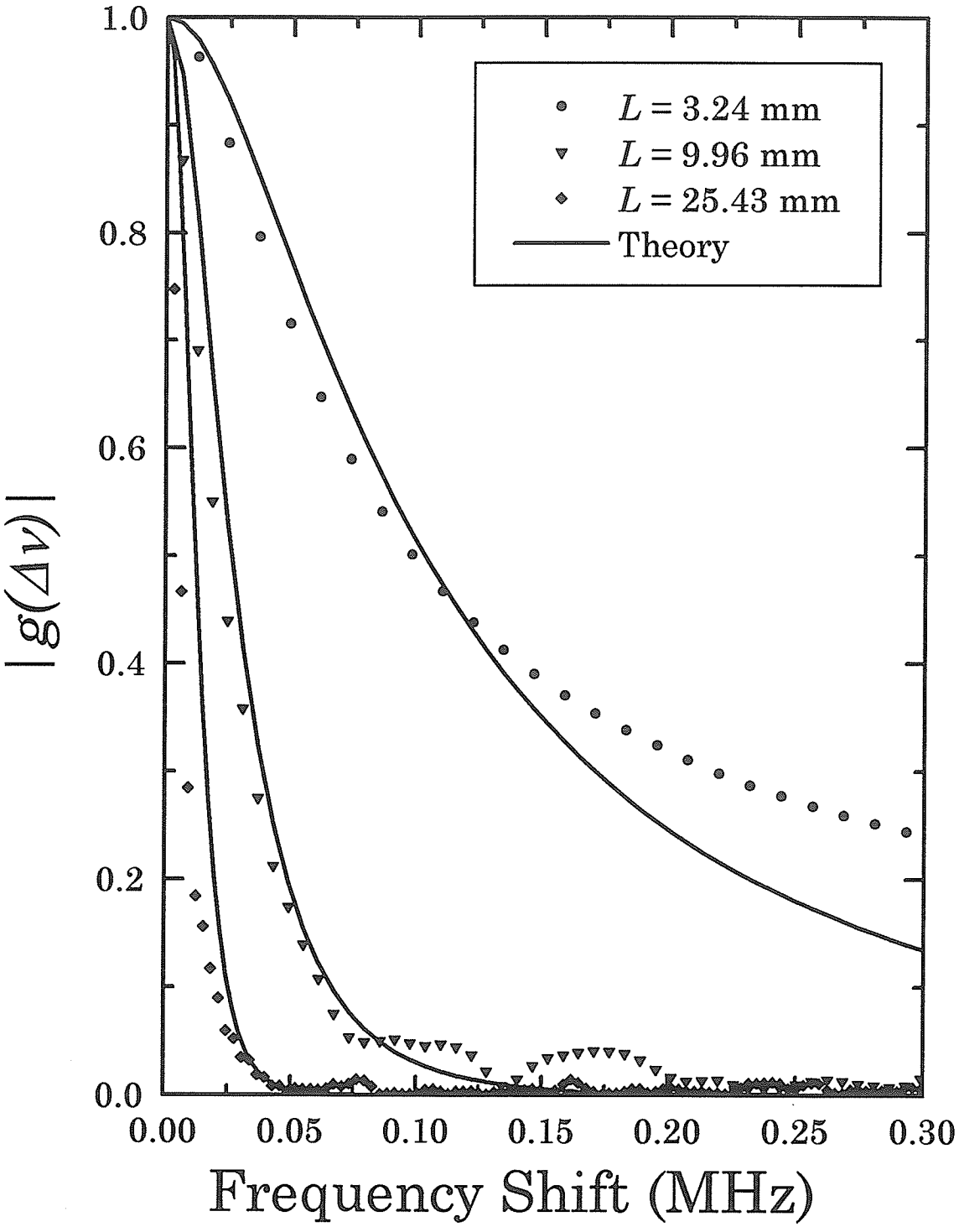

Figure 4.9. Correlation functions measured from 1.2 to 3.8 MHz using a focused incident beam. Theory curves are calculated using diffusion theory with $D = 0.435$ mm^2/μs, $\tau_a = 12$ μs and $l^* = 0.8$ mm.

We see the theory is in better agreement with the data for the lower frequency range which may be evidence for a considerable amount of dispersion in the 3–4 MHz range. Within each frequency range however, the agreement is generally better for the thicker samples, indicating a consistent breakdown in the theory for thinner samples over all frequency ranges.

4.1.2 Plane Wave Geometry

In the plane wave geometry, we acquired data from samples of four different thicknesses. We were unable to generate a strong enough signal to obtain reliable, clean data from samples of thickness $L > 10$ mm, where the lack of signal strength lead to poor signal to noise characteristics in the detected signals. The results for the four sample thicknesses are shown in Fig. 4.10. Once again we note that the correlation functions decay more quickly as the sample thickness increases. For two of the samples, data were acquired with the hydrophone both up close to the sample face, where the separation was ~ 2 mm (*near field*), and far from the sample face, where the separation was approximately 15 cm (*far field*). For the 10 mm sample there is very little difference between the data acquired in the different manners, while for the thinner sample, the correlation function decays much faster when the data were acquired in the far field. This results from a spurious broadening of the diffusive time profile caused by the extra transit time required for sound leaving the sample at oblique angles (with respect to the normal) to travel through the water to the detector. Experimentally this means that the detecting

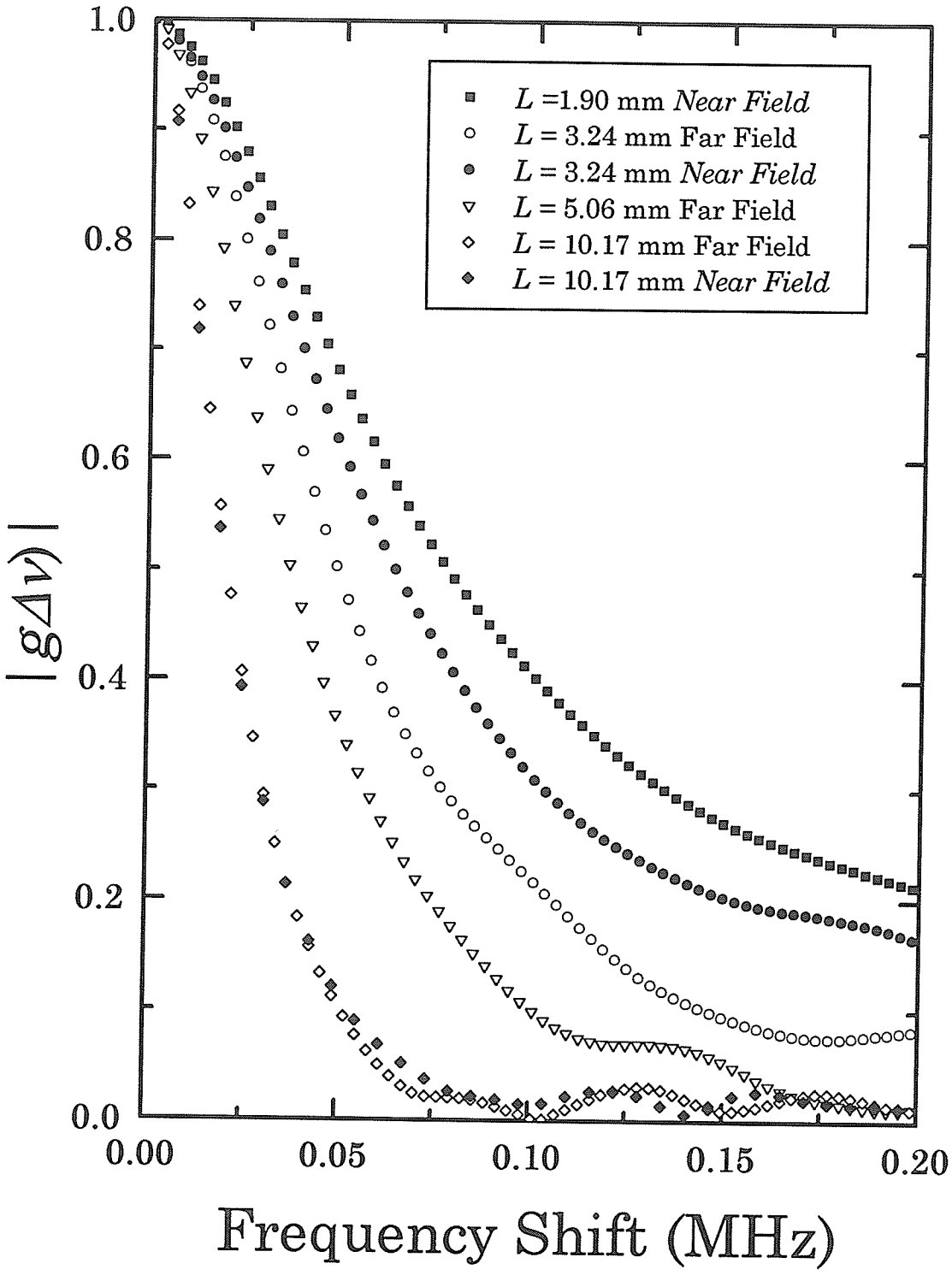

Figure 4.10. Correlation functions from 2 -3 MHz. Plane wave incident beam.
Data were collected in near and far field configurations for two of the sample thicknesses.

hydrophone needs be as close as possible to the sample, in order to avoid obtaining spurious data, particularly for thin samples where the effect is more pronounced.

Using Eq. (30) from chapter 2, we can calculate theoretical correlation functions for each of the four thicknesses. This has been done and the results are shown in Fig. 4.11, where the theory is compared with data. The values used in the calculation were $D = 0.43$ mm^2/μs, $\tau_a = 12$ μs, and $l^* = 0.8$ mm [2,3,4], which are the same values used for the point source correlation functions, in this frequency range. We have included in the plot the intermediate thickness, $L = 5.06$ mm, data (denoted by hollow symbols) which were acquired in the far field. We do not expect the pulse broadening to have as large an effect at this thickness as it did for the $L = 3.24$ mm sample, and we do not have near field data from this thickness. The theoretical curves match the data for the 3.24 mm and 10.17 mm sample very well. The agreement is less good for the 5.06 mm sample, where the data decorrelate faster than the theory. This difference between data and theory is likely due to use of the detector in the far field, rather than from a problem in the theory. This argument is reinforced when we recall that data taken from the far field tend to decorrelate faster than those from the near field as seen in Fig. 4.10. On the other hand the theory does not agree at all well with data taken from the 1.9 mm sample, where the data decorrelates faster than theory.

In general, we see that the theory agrees well with the data for all but the thinnest samples, where it breaks down dramatically.

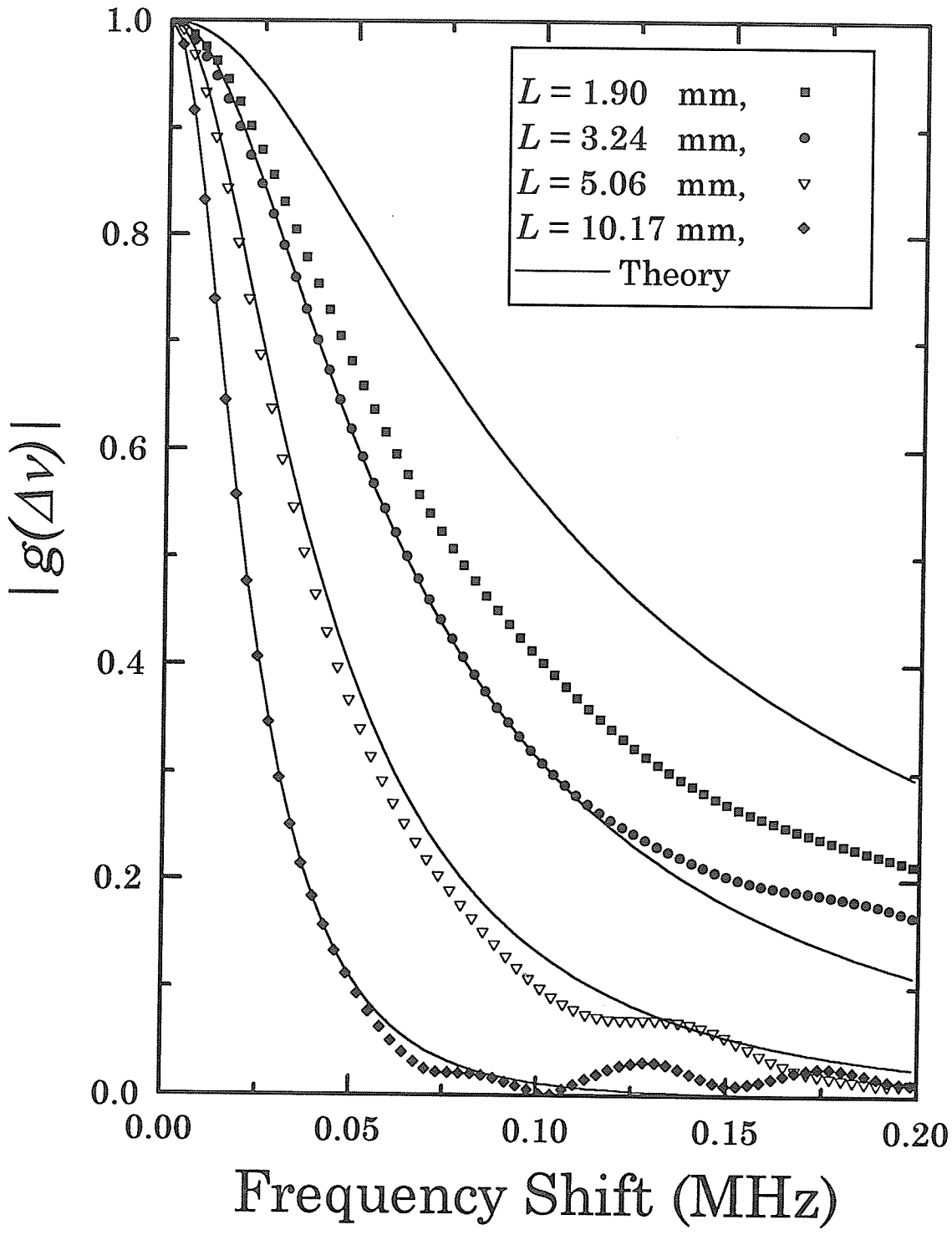

Figure 4.11. Correlation functions from 2 -3 MHz, using a plane wave incident beam. Also shown are theoretical curves calculated for the four sample thicknesses using diffusion theory with $D = 0.43$ mm^2/μs, $\tau_a = 12$ μs, and $l^* = 0.8$ mm.

To further investigate the interpretation of the data using the diffusion approximation, we fit the theory to data to determine the values for D and τ_a which best describe the data. The results of this fitting process are shown in Fig. 4.12. The best fits to the data are shown along with the parameters of D and τ_a corresponding to each fit. The fit curves closely approximate the data, particularly for the thicker samples, and the fit to thinnest sample is surprisingly good. However the parameters generated for each fit are quite different from the parameters we expect at this frequency range. Again the thickest sample has the best agreement, and, as the sample thickness is reduced, the fitted parameters become further removed from our accepted values. We note a gradual decline in the values of both D and τ_a as the sample thickness decreases. The parameters for the 1.9 mm sample do not appear to fit this trend, especially for τ_a which has an unphysically large value.

For all sample thicknesses, we find that a wide range of the parameters D and τ_a give acceptable fits, making it difficult to pin them down unequivocally from frequency correlation data alone. This problem occurs largely because of the correlation between D and τ_a in the fits. This problem has a larger effect in the frequency correlations than in the time domain data (where D is largely determined by the initial rise of the diffusion pulse, and τ_a by its long time tail). If the measured correlation function extended over an additional decade before being lost in the background noise, it would be possible to determine D and τ_a more reliably from the frequency correlation; this is a formidable experimental challenge since the

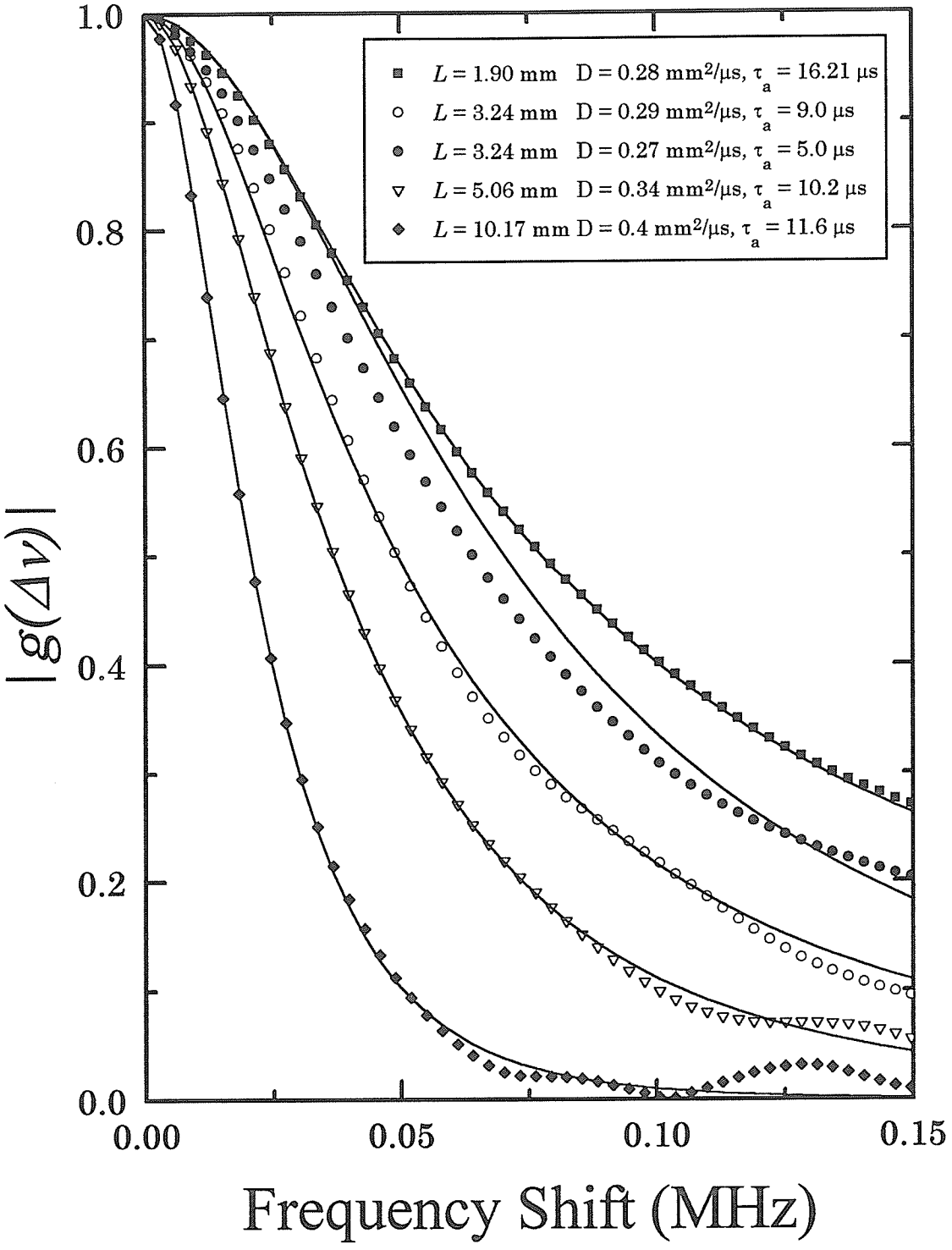

Figure 4.12. Frequency correlation function, evaluated between 2 and 3 MHz, compared with fits to diffusion theory. Plane wave incident beam. (l^* was fixed at 0.8 mm)

frequency range over which the correlation function can be measured is made narrow due to dispersion. Thus one, would need to average over an extremely large (>1000) number of independent speckles to get better results. For the present data we conclude that the most meaningful comparison between experiment and theory can be made for the calculated correlation functions shown in Fig. 4.11.

It appears that for a plane wave input, diffusion theory and experiment agree very well for thicknesses where $L \geq 3$ mm, however, for L less than this there are dramatic discrepancies. This breakdown between theory and experiment seems to happen quite suddenly as the sample thickness is reduced. To investigate this further, we begin by recalling that the correlation function is the Fourier transform of the diffusive time series. Thus we turn to the diffusive time series to learn more about this behavior.

For each of the samples, in both the point source and plane wave geometries, we can analyze the data, from which the correlation functions were determined, in terms of the diffusion time profile. We use these data to examine the behavior of the diffusion profiles for the thinnest samples to investigate further the break down of the diffusion theory at these sample thicknesses. In Fig. 4.13 we plot the 2–3 MHz correlation data for three samples along with the FFT of the diffusive time series for those same samples. These FFTs agree closely with the correlation functions, the small observed differences probably reflecting the effects of dispersion arising from the large frequency range in the diffusive pulse data. The agreement indicates that an examination of the comparison between the diffusion data and theory may give

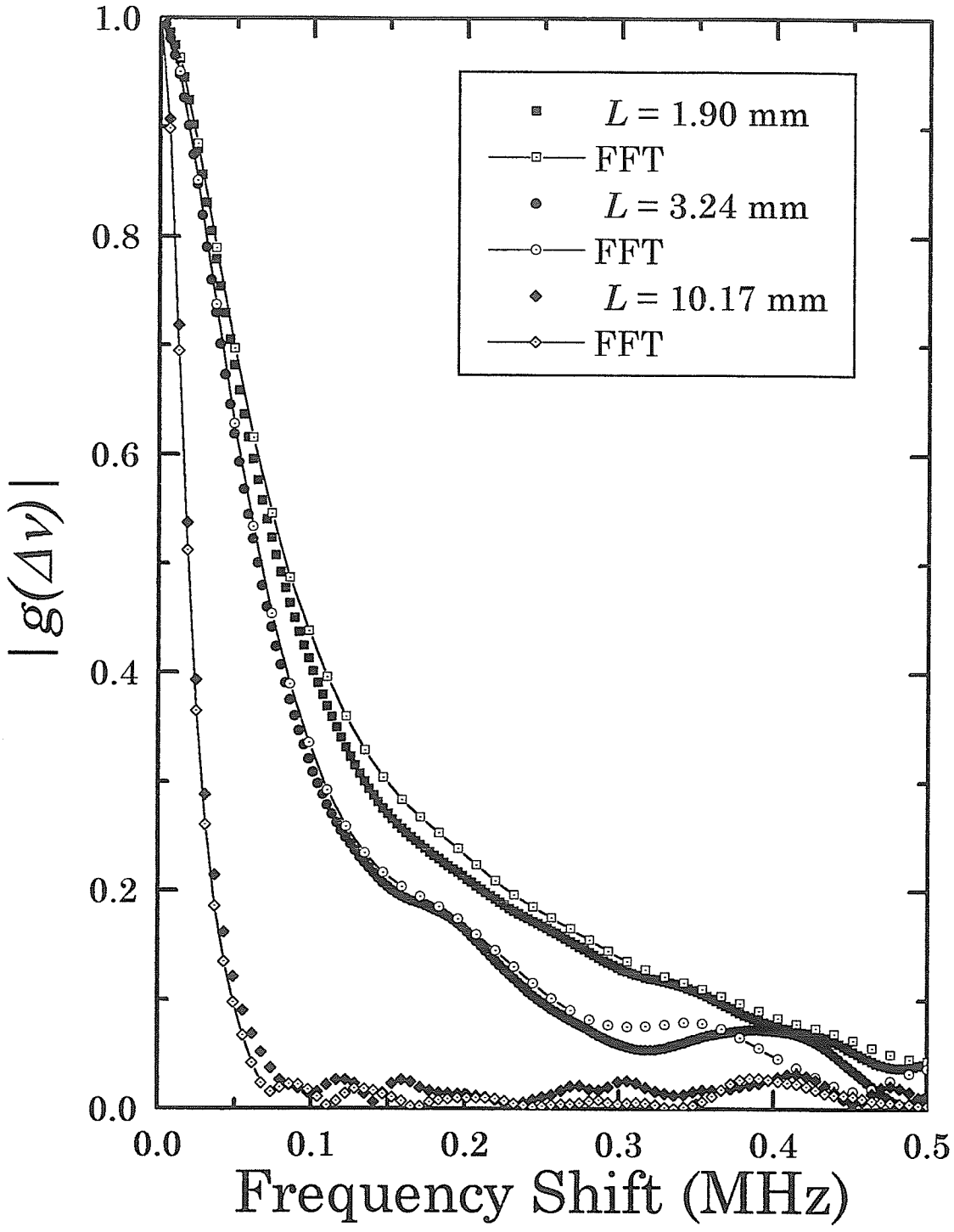

Figure 4.13. Comparison plot of correlation data (symbols) for three sample thicknesses, with FFT of the diffusion profile (line and symbol) corresponding to each thickness. Plane wave input.

us insight into the corresponding relationship between the correlation functions and theory.

In Figs. 4.14 and 4.15, we show the comparison between time domain data and diffusion theory for the two thinnest samples. The plane-wave data and theory are shown in Fig. 4.14, while Fig. 4.15 shows the corresponding point-source results. For the 3.24 mm sample, two theory curves are shown, the solid lines representing the theory normalized to fit the tail of the time-domain data and the dashed lines representing the theory rescaled to fit the peaks in the data. (Because it is difficult to accurately measure the *absolute* transmitted intensity in our experiments [2, 3], the relative magnitude of theory and data is treated as an adjustable scaling factor, of order unity, in the fitting procedure.) In the plane-wave geometry, we see that for the 3.24 mm sample, the solid line gives a very good description of the data over most of the time profile, the exception being the narrow peak between 2 and 4 μs where some additional scattering is observed in the data. By contrast, for the 1.9 mm sample, diffusion theory fails to give an adequate description of the data at all times; not only does the theory begin and peak at earlier times than the data, but it falls well below the data at long times (where no plausible normalization of the theory is consistent with the amount of scattering seen in the data). The corresponding point-source picture (Fig. 4.15) illustrates the differences between theory and experiment even more dramatically. Again, we see that the initial rise of the diffusion profile is predicted by the theory to occur before it is actually observed in the data; furthermore, in the point-source geometry, this holds for *both* the 1.9 mm and 3.24 mm samples.

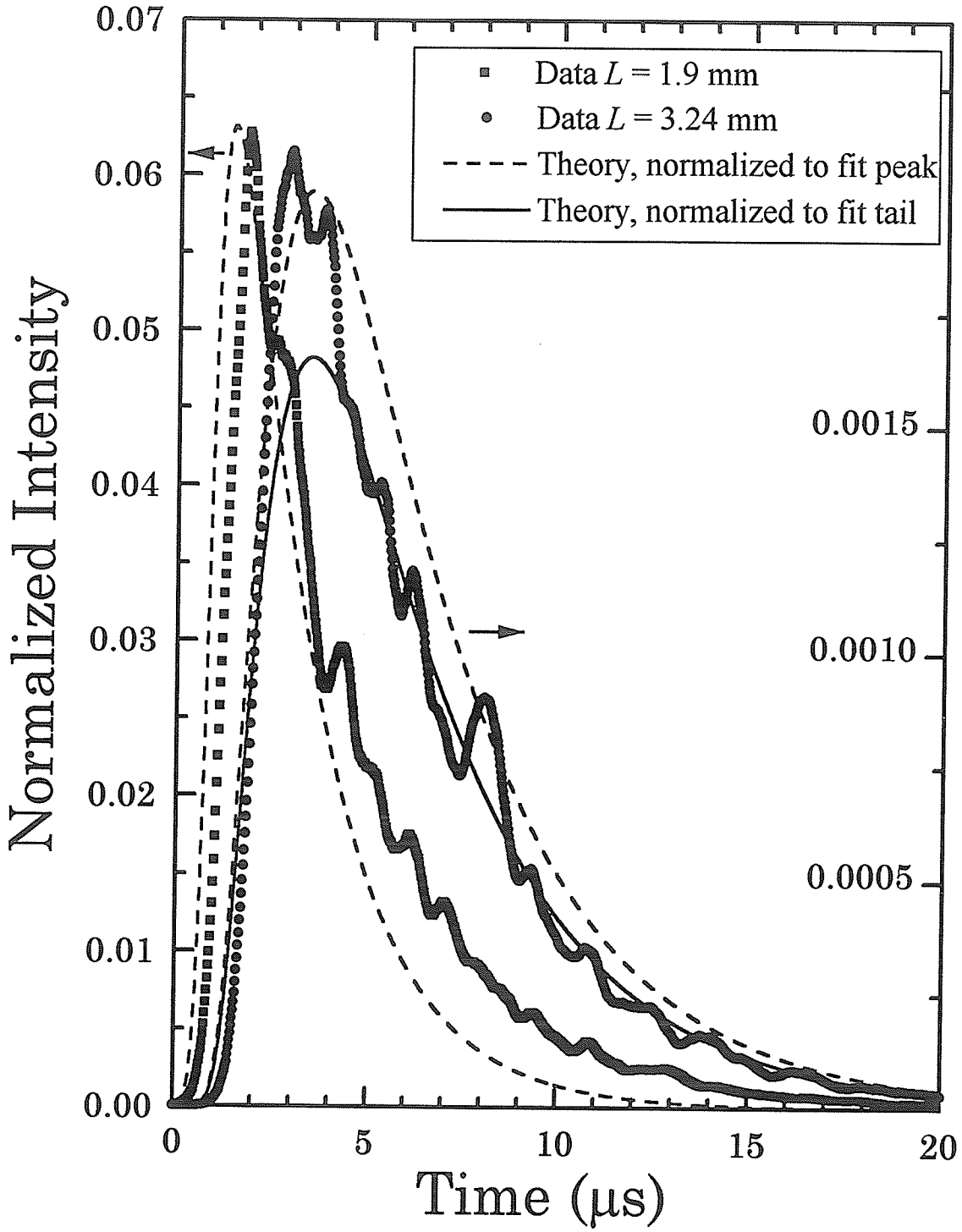

Figure 4.14. Comparison of transmitted intensity profiles (short input pulses, plane wave geometry) with the predictions of diffusion theory using $D = .43$ mm^2/μs, $\tau_a = 12$ μs, and $l^* = 0.8$ mm.

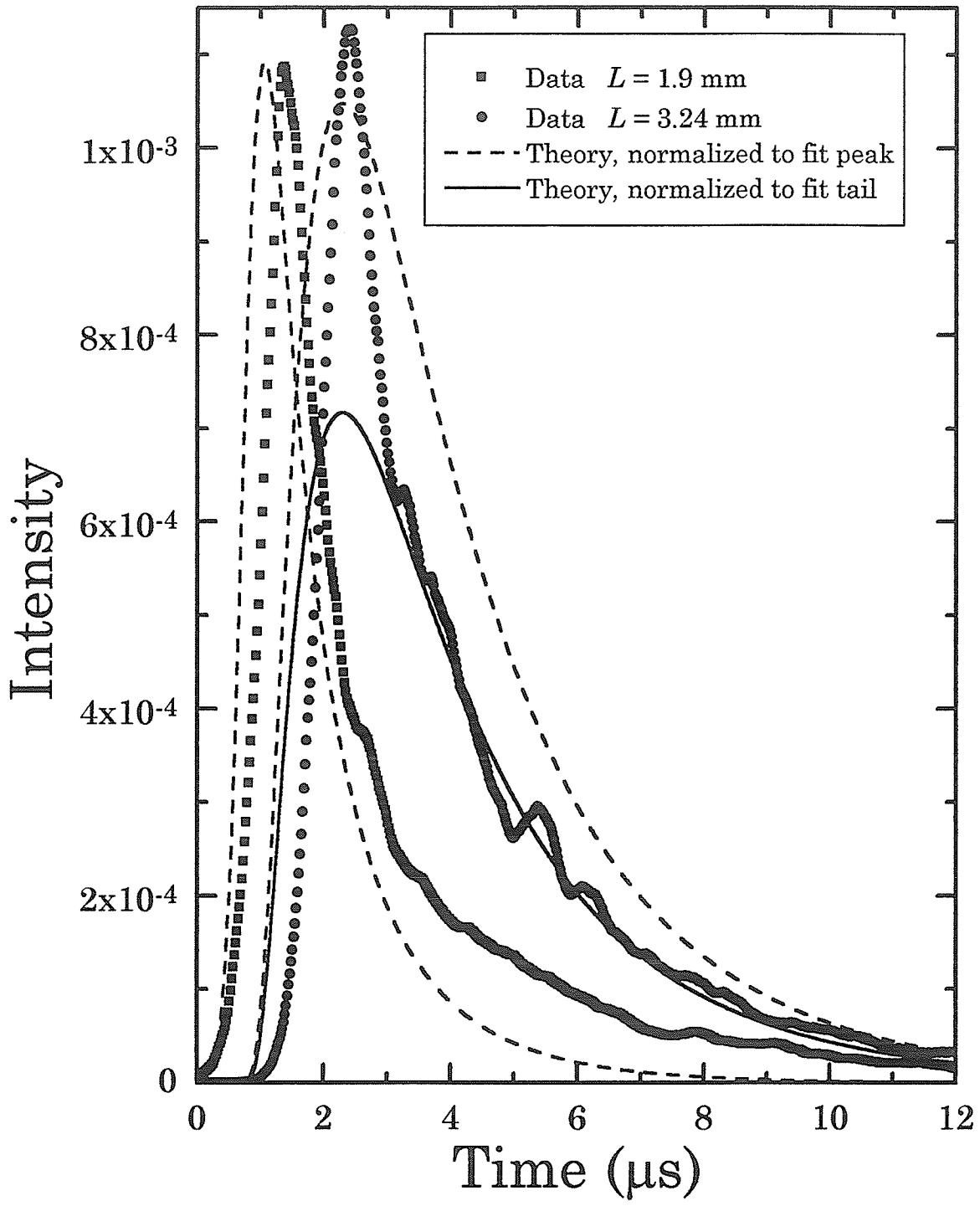

Figure 4.15. Comparison of transmitted intensity profiles (short input pulses) in the point source geometry with the predictions of diffusion theory using $D = 0.43$ mm^2/μs, $\tau_a = 12$ μs, and $l^* = 0.8$ mm.

The 3.24 mm sample, corresponding to a thickness to mean free path ratio of $L/l^* \approx 4$, appears to have a "critical" thickness where the breakdown of diffusion theory is beginning to manifest itself, but where it is not complete. To focus on this behaviour, we plot in Fig. 4.16, the plane-wave and point-source data, along with theory, for this sample. Again we emphasize that the solid lines in this figure show that diffusion theory can give a very good description of the data for this sample at times beyond the peak in the intensity profile, but that the theory becomes inadequate to describe the data at early times where only a few scatterings have occurred. We note that this behaviour also elucidates the origin of the apparently good agreement between theory and experiment for the initial decay of the frequency correlation function, since the frequency correlation function at small frequency shifts is primarily sensitive to the long-time tail in the time-domain profile. Thus the time domain data appear more sensitive to the departures from diffusion theory than occur when the number of scatterings is too few to fully randomize the phases of the scattered waves. From Fig. 4.16, the crossover to non-diffusive behaviour is observed for this sample at times in the 3.5 to 4 μs range, corresponding to about 7 or 8 scatterings.

The deviations from diffusion theory seen at early times in Fig. 4.16 are more pronounced for the point-source data than for the plane-wave data. These discrepancies are seen both in the amount by which solid curves fall below the observed peaks in the data, and in the extent to which the initial rise predicted by diffusion theory precedes the corresponding rise in the data. The explanation for this is that a wider distribution of path lengths is sampled in the plane-wave

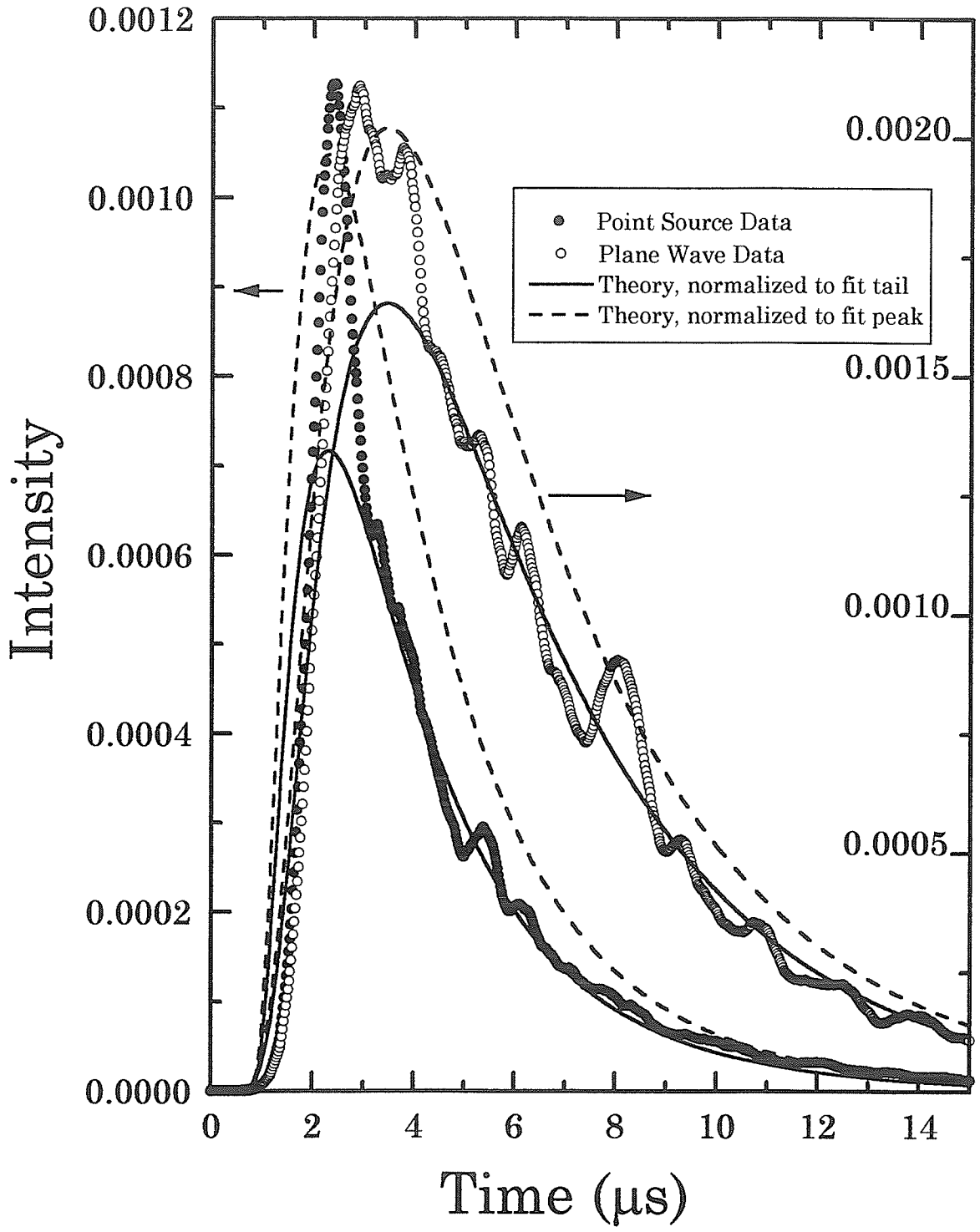

Figure 4.16. Comparison of point-source and plane wave data for $L = 3.24$ mm. Also shown are the predictions of diffusion theory for $D = 0.43$ mm^2/μs, $l^* = 0.8$ mm, $\tau_a = 12$ μs.

geometry than in the point-source geometry for samples of the same thickness. A representation of this is shown in Fig. 4.17

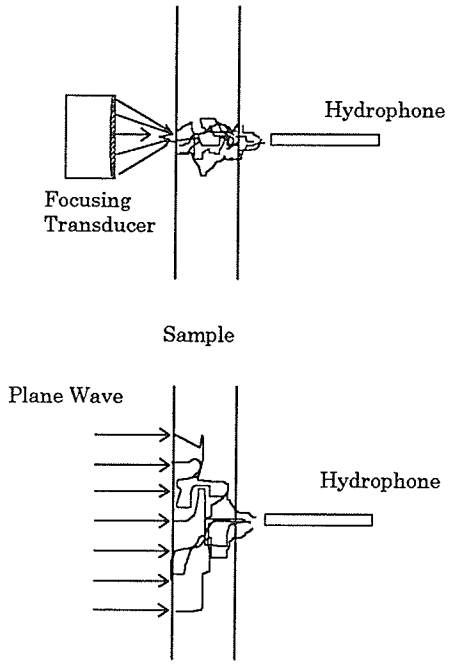

Figure 4.13. Distribution of pathlengths through sample for different input sources

which shows schematically why plane waves on average undergo more scattering events before emerging from the sample, for a given thickness, than do waves generated from a point source. This also suggests that diffusion theory will begin to break down in the point-source geometry for a larger value of L/l^* than in the plane-wave geometry.

We conclude that our data are represented by diffusion theory very well as long as the ratio of L/l^* is greater than a well defined limit. For a plane-wave source, this limit appears to be very close to the value for the 3.24 mm sample,

giving $L/l^* \approx 4$. For a point source, the limit appears to be somewhat larger, between about 4 and 7, as determined from the comparison of diffusion theory with our data on the 3 mm and 5 mm samples.

4.2 Spatial Correlation Study

4.2.1 Measurements and Analysis

To probe the spatial correlations of multiply scattered sound we measured the sound field transmitted through the sample, at a large number of closely spaced positions, in a linear traverse of the sample face. The input waveform was quasi–cw (continuous wave), which allowed all available paths to be sampled as the sound propagated through the sample, and ensured the input waveform had a well defined frequency. At each position, we recorded the detected signal over a 10 μs interval. Each record was digitized by the oscilloscope into 500 point records with 20 ns time spacing between points. Data were recorded at 801 positions, separated by 0.03 mm, in each traverse, or scan. The length of each scan was then 24 mm. We then 'inverted' the data into 500 time–bin files where each file corresponded to a record of detected field vs. position at a particular time in the original waveforms. Since we were saturating all available paths by using a continuous wave input pulse we expect the correlation functions calculated from each file to be identical. There is, however, a small amount of noise appearing in the individual field vs. position records functions and by averaging the correlation functions calculated from the 500 files together we are able to reduce the effects of noise in the resulting correlation function.

We collected data from samples of thickness $L = 15$ mm, and $L = 10$ mm. The majority of the data were taken on the 10 mm sample, where data were acquired

using input frequencies of 1.5, 2.5, and 3.5 MHz. In addition, at 2.5 MHz we acquired data from nine independent transverse scans of the sample face, each scan being made horizontally at a different height along the sample face. Each scan had the same number of positions and identical separation between positions. From these scans we calculate an average spatial correlation function, $\langle g_1(\Delta x)\rangle_{scans}$, allowing a more accurate determination of the correlation function to be made because of ensemble averaging. For the other input frequencies we acquired data from a single scan only. From the 15–mm thick sample we also acquired data from only a single scan, using an input frequency of 2.5 MHz.

In Fig. 4.18a we plot the detected field across the sample face at one specific time, for the 15–mm thick sample. It is also possible for us to extract amplitude and phase information from these scattered signals via simple manipulation of the field data as explained in detail in appendix 1. The results of doing this for the field data of Fig 4.18a are presented in Figs. 4.18b and 4.18c, respectively. The fluctuations seen in the field data of Fig. 4.18a and the amplitude data of Fig. 4.18b arise from the interference caused by sampling different bead distributions as we traverse the sample face. The width of the amplitude fluctuations correspond roughly to the size of the speckle, which can be seen to be slightly bigger than the sound wavelength (0.6 mm at 2.5 MHz). This is reasonable, because by moving the detector by a distance of order a wavelength of the sound, the lengths of the different paths the scattered sound waves must travel to reach the detector will also increase or decrease by a substantial fraction of a wavelength; thus the net interference at the

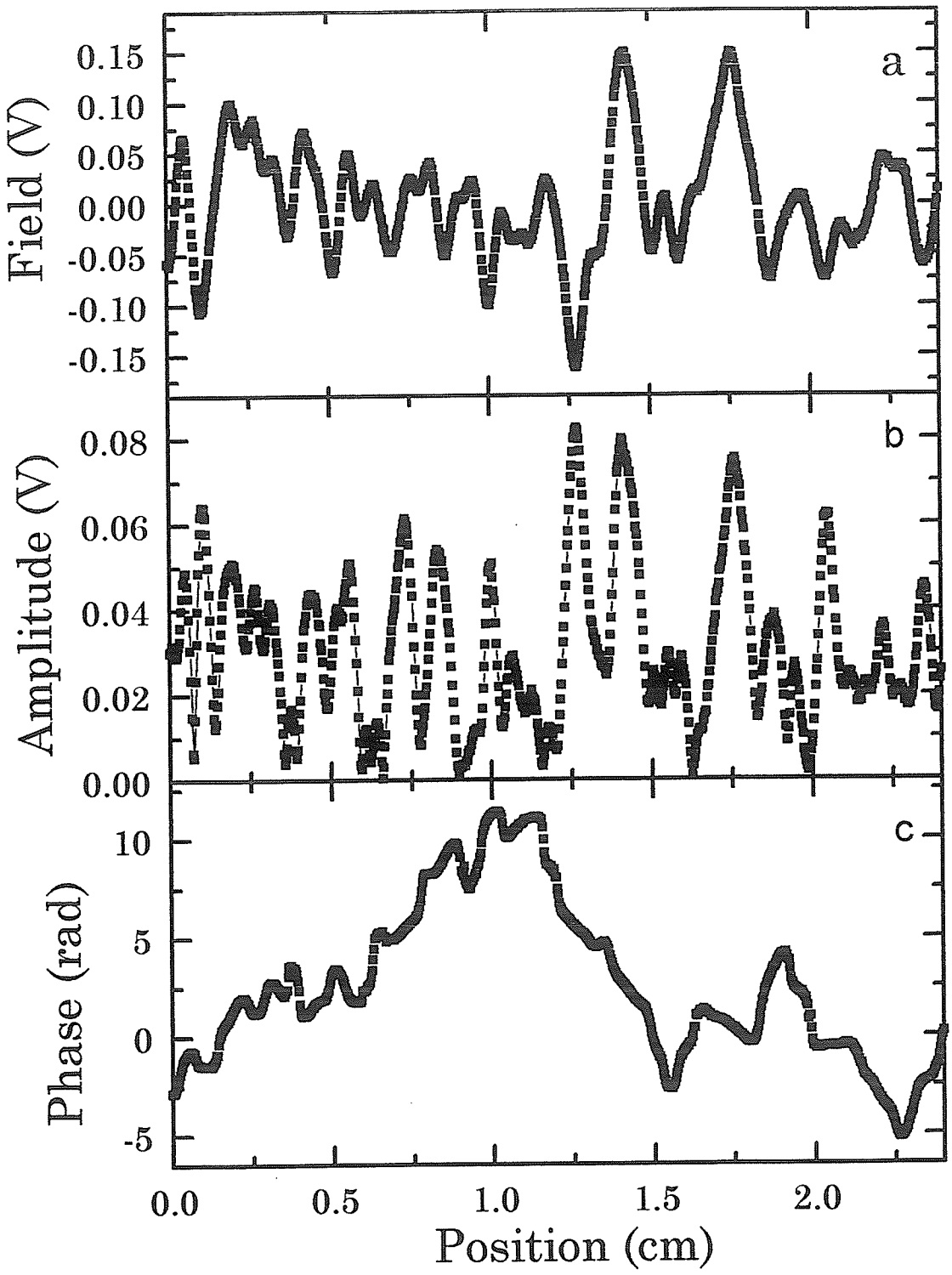

Figure 4.18. Transmitted field, amplitude and phase, in a linear grid of 801 speckles across the face of the sample. $L = 15$ mm.

detector will change from constructive to destructive, or vice versa. Figure 4.18c shows that the phase of the speckle pattern remains roughly constant over the size of each speckle, but changes abruptly between speckles. In addition, the average phase appears to increase slowly towards the centre of the speckle pattern possibly reflecting some long-range phase correlations in the sample. However more data is required to establish this and its investigation is beyond the scope of this thesis.

These qualitative observations can be made more rigorous if we calculate the spatial correlation function from the field vs. position, $S(x)$ data measured in the experiment. To obtain the field correlation function from $S(x)$ we employed the following equation.

$$\begin{aligned} g_1(\Delta x) &= \frac{1}{g_1(0)} \int S(x) S^*(x + \Delta x) \mathrm{d}x \\ &\approx \frac{1}{g_1(0)} \sum_{j=0}^{n-i-1} \frac{S(x_j) S^*(x_j + \Delta x_i)}{n - i}. \end{aligned} \tag{5}$$

In this equation, $g_1(0)$ is the value of the field correlation function at zero position offset, and n is the total number of data points in the spatial range from x_0 to x_n over which the correlation function is calculated. The interval $\Delta x = \Delta x_i = i\delta x$ is the spatial shift, where δx is the distance between adjacent points in the scan (0.03 mm). The next step is to average all the $g_1(\Delta x)$ corresponding to different times to reduce noise.

For comparison we also calculated the intensity correlation function from the amplitude vs. position data using

$$\frac{\langle I(x)I(x+\Delta x)\rangle}{I_{ave}^2} = \frac{1}{I_{ave}^2}\int I(x)I(x+\Delta x)\,dx \approx \frac{1}{I_{ave}^2}\sum_{j=0}^{n-i-1}\frac{I(x_j)I(x_j+\Delta x_i)}{n-i}, \tag{6}$$

where the intensity, $I(x)$, is the square of the amplitude data, and the normalization factor, I_{ave}^2, is the average value of $I(x)$ over the 810 point record length of a given file, i.e.

$$I_{ave}^2 = \left[\frac{1}{n}\sum_{i}^{n} I(x_i)\right]^2. \tag{7}$$

The measured intensity correlation function is simply related to the field correlation function by

$$\frac{\langle I(0)I(\Delta x)\rangle}{I_{ave}^2} = 1 + \beta g_2(\Delta x) \tag{8}$$

where β is a constant of order unity that is determined by the detector geometry [6], and $g_2(\Delta x)$ is related to $g_1(\Delta x)$ via the Siegert relation [5]

$$\left|g_1(\Delta x)^2\right| = g_2(\Delta x). \tag{9}$$

In Fig. 4.19 we compare intensity correlation functions calculated for the three different input wave frequencies used in the experiment. These data were acquired using the L = 10 mm cell. We expected the correlation function to decay faster with increasing frequency since, by the argument given above, a shorter wavelength of the sound would be expected to result in a smaller speckle size. This is, indeed, what we observe. Furthermore, the correlation function, $g_2(x)$ drops to 1/2

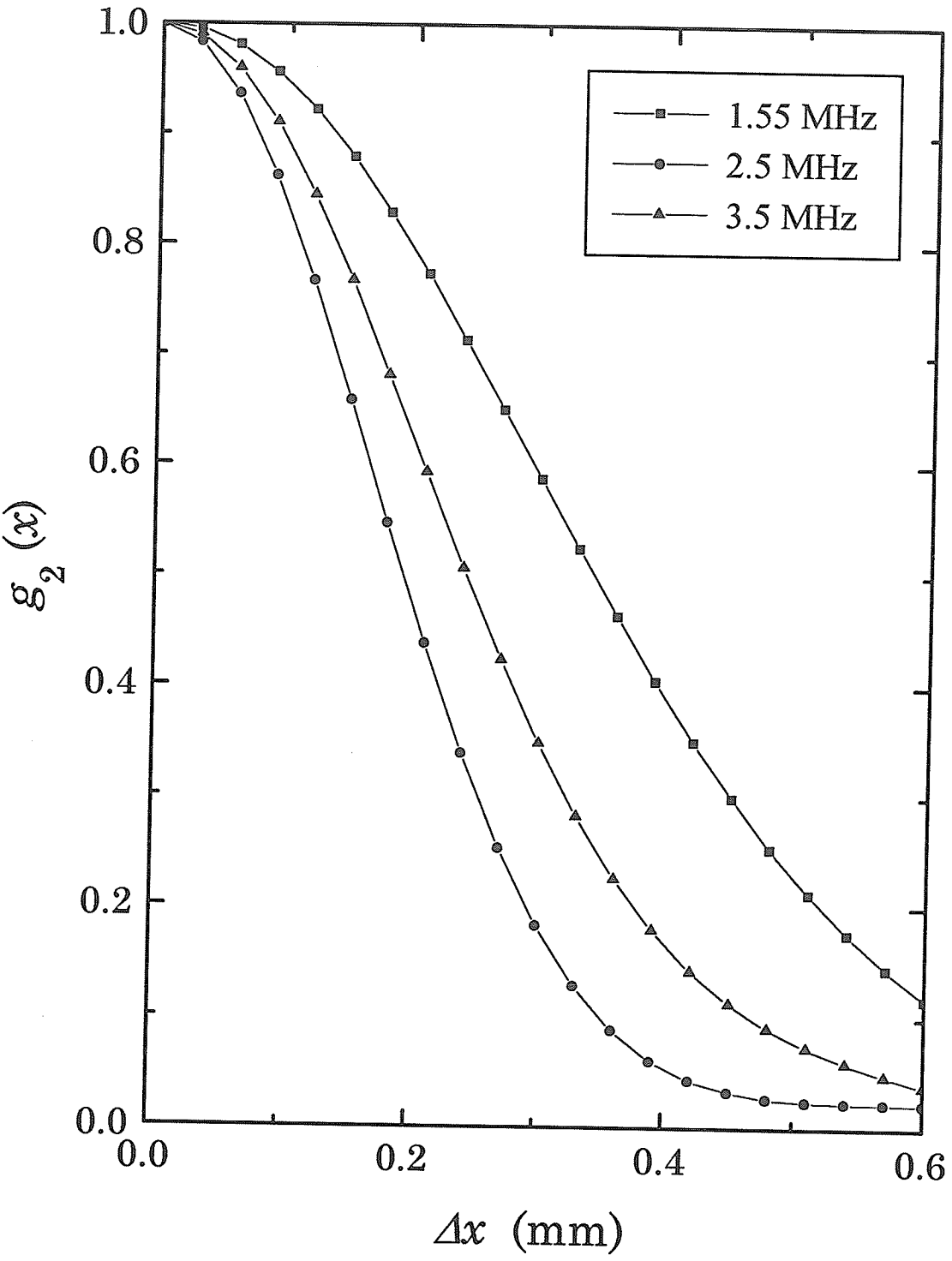

Figure 4.19. Intensity correlation function, $g_2(x)$, at 3 frequencies.

for the three frequencies when $\Delta x \sim 0.4\ \lambda$. This is consistent with the expectation that the average spatial extent of the speckles be approximately equal to the ultrasonic wavelength when the speckle pattern is observed in the near field, which at an input frequency of 2.5 MHz corresponds to a wavelength in water of ~ 0.6 mm.

We do not expect the correlation functions to show any dependence on the thickness of the sample, since it is the final scattering events that contribute most to the decay of the spatial correlation function. In Fig. 4.20 we present a comparison of the correlation functions from samples of different thickness. In this plot, scans from the L = 10 mm sample (hollow symbols) are plotted with the results from the single scan of the L = 15 mm cell (solid symbol). Although there is large scatter in the data for the different scans, the data for the two sample thicknesses are at least shown to be consistent with each other in this figure, as the 15 mm sample data overlaps one of the scans for the 10 mm sample. However, the independence of the correlation function on sample thickness is not clearly demonstrated, pointing to the need for better ensemble averaging to obtain a more definitive result.

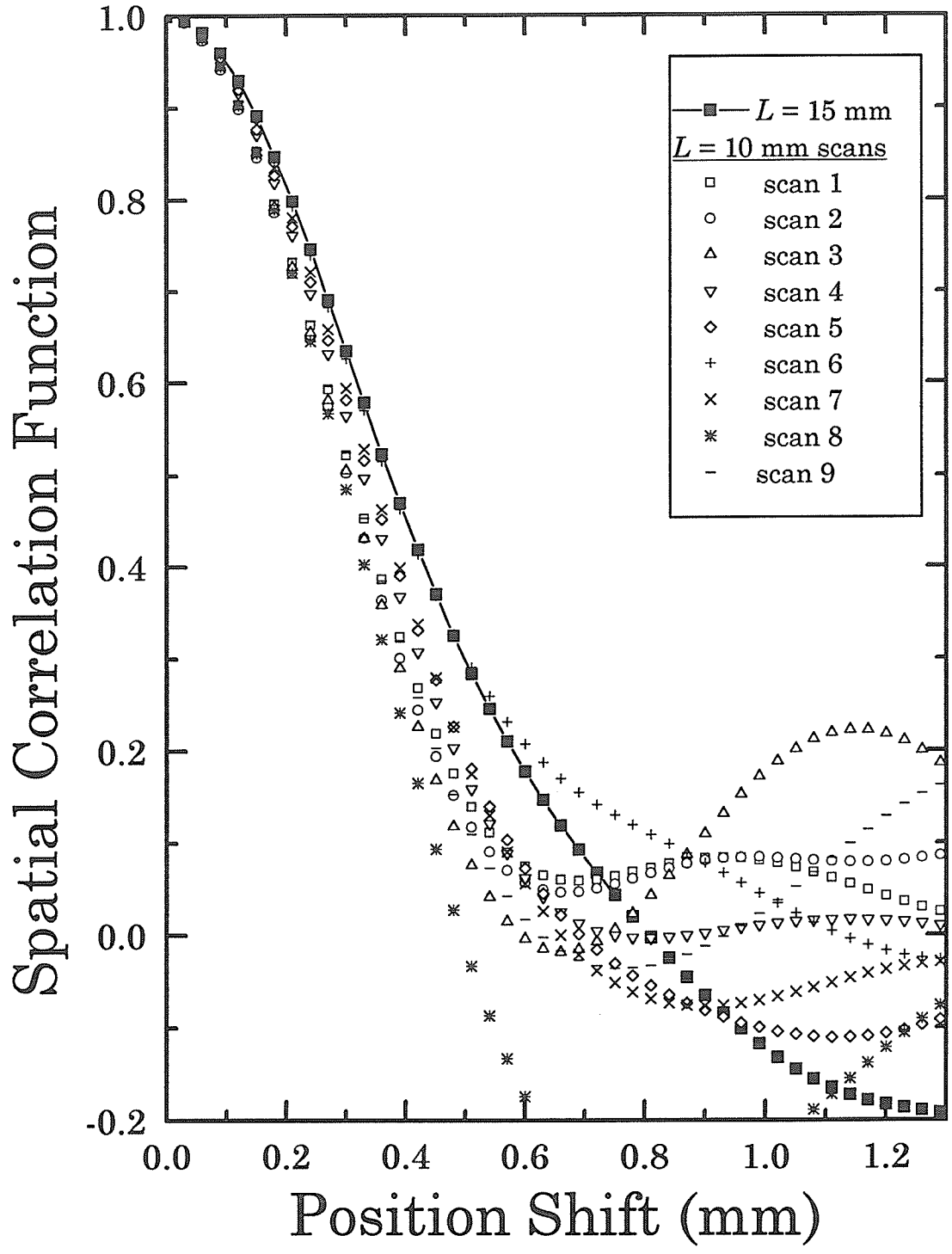

Figure 4.20. Comparison plot of correlation functions taken from two sample thicknesses. $L = 15$ mm data are plotted with the solid symbols while all nine $L = 10$ mm scans are plotted with open symbols.

We now turn to the largest collection of data, acquired from the L = 10 mm sample, using an input frequency of 2.5 MHz. The results of the nine transverse scans are plotted in Fig. 4.21, along with their average, $\langle g_1(\Delta x)\rangle_{scans}$. We notice large fluctuations in the data for position shifts larger than 0.8 mm, which mostly disappear in the averaged correlation function.

To interpret these data, we make use of the theoretical expression for the spatial correlation function whose derivation was outlined in the theory section (Chapter 2, Eq.(40)).

$$g_1(\Delta x) = 2\frac{J_1(K\,\Delta x)}{K\Delta x}, \tag{4}$$

where $K = \pi D/\lambda z$. This equation was derived for use in light scattering experiments where the coherent input beam is scattered from a rough circular surface. Although our experimental geometry is different, there is an approximate correspondence between this simple model and our experiment, as can be seen from Fig. 4.22 below.

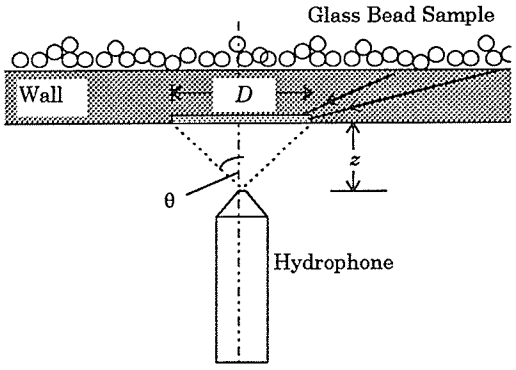

Figure 4.22 Detail of sound detection geometry in our experiment.

The scattered waves that determine the speckle pattern come from the last scattering events inside the sample, and therefore emerge (with random phases)

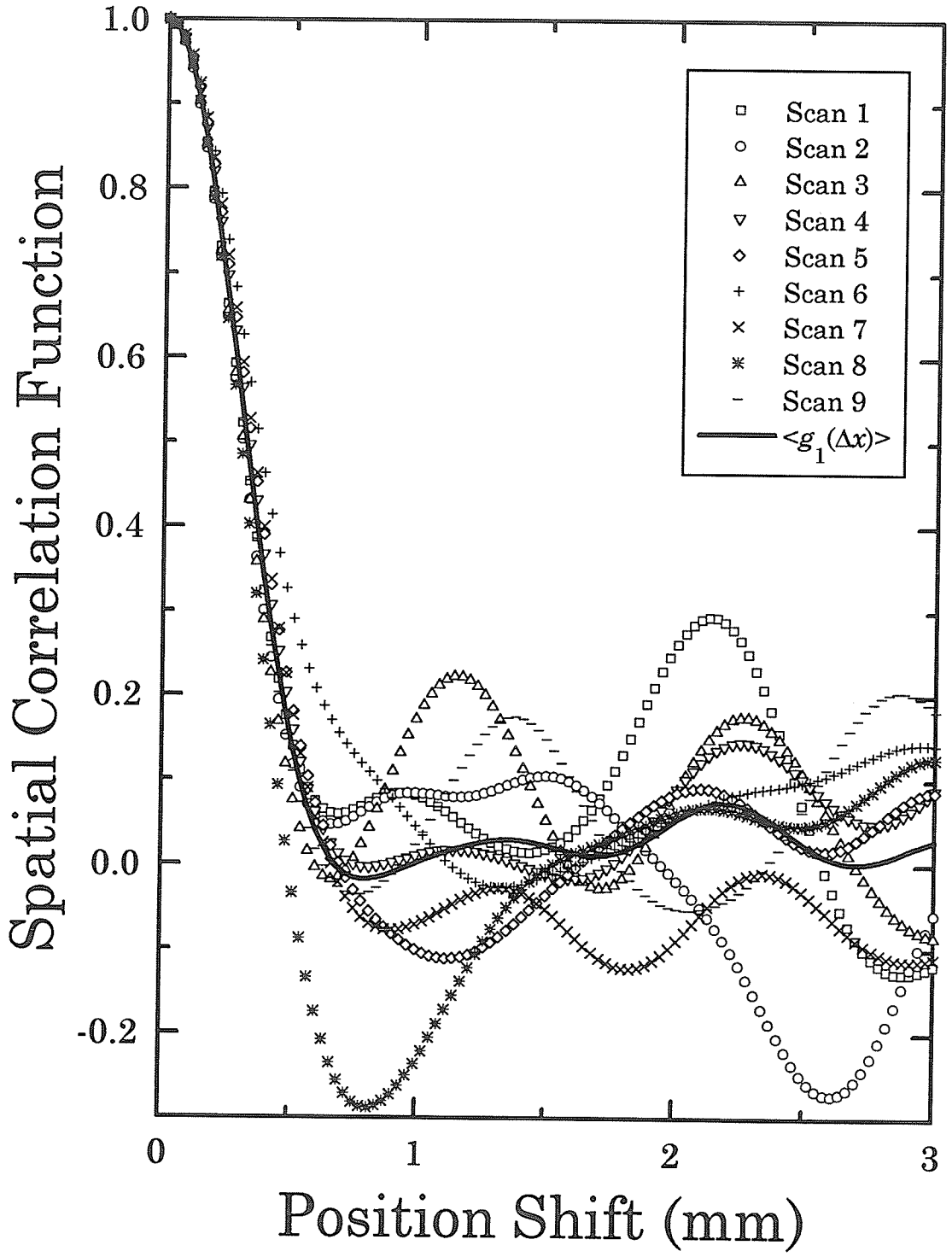

Figure 4.21. Correlation data from nine linear transverse scans of the sample, and their average. $L = 10.$ mm

from a region within approximately a mean free path of the interface between the randomly distributed glass beads and a thin polystyrene wall. The detector is a miniature hydrophone, whose circular tip has diameter 200 μm which is considerably less than a wavelength of the sound in water; as a result, the hydrophone's angular acceptance is determined by diffraction and extends to quite large angles of incidence. However, the actual range of angles over which sound is detected is smaller than this limit, because of the effects of refraction of the sound waves leaving the sample through the polystyrene wall. This is depicted in Fig. 4.22 where D is the diameter of a circular area on the sample wall, from which scattered sound is directed out to be detected by the hydrophone. In our experiment $D/z \approx 2$, since the maximum angle for sound leaving the sample is ~ 45 degrees, determined from Snell's law, using the phase velocities of the wall sample and water outside the sample [3]. For an input frequency of 2.5 MHz, we therefore, estimate values of K on the order of 10 mm^{-1}. We caution, however, that this theoretical approach is only an approximate model for our experiment, the main limitations being that the theory was developed for a far–field measurement while we detect in the near field, and that D is only a rough estimate of the area sampled by the hydrophone.

The results of fitting the averaged correlation function for the L = 10 mm sample to theory are plotted in Fig. 4.23. The main picture shows the initial decay of the correlation function, while the inset plot extends the x–axis to include larger position shifts. From this inset we see that the theory exhibits fluctuations comparable to the fluctuations found in the data, although the first minimum in the theory is much deeper than in the data. The resultant fit to the data is dominated

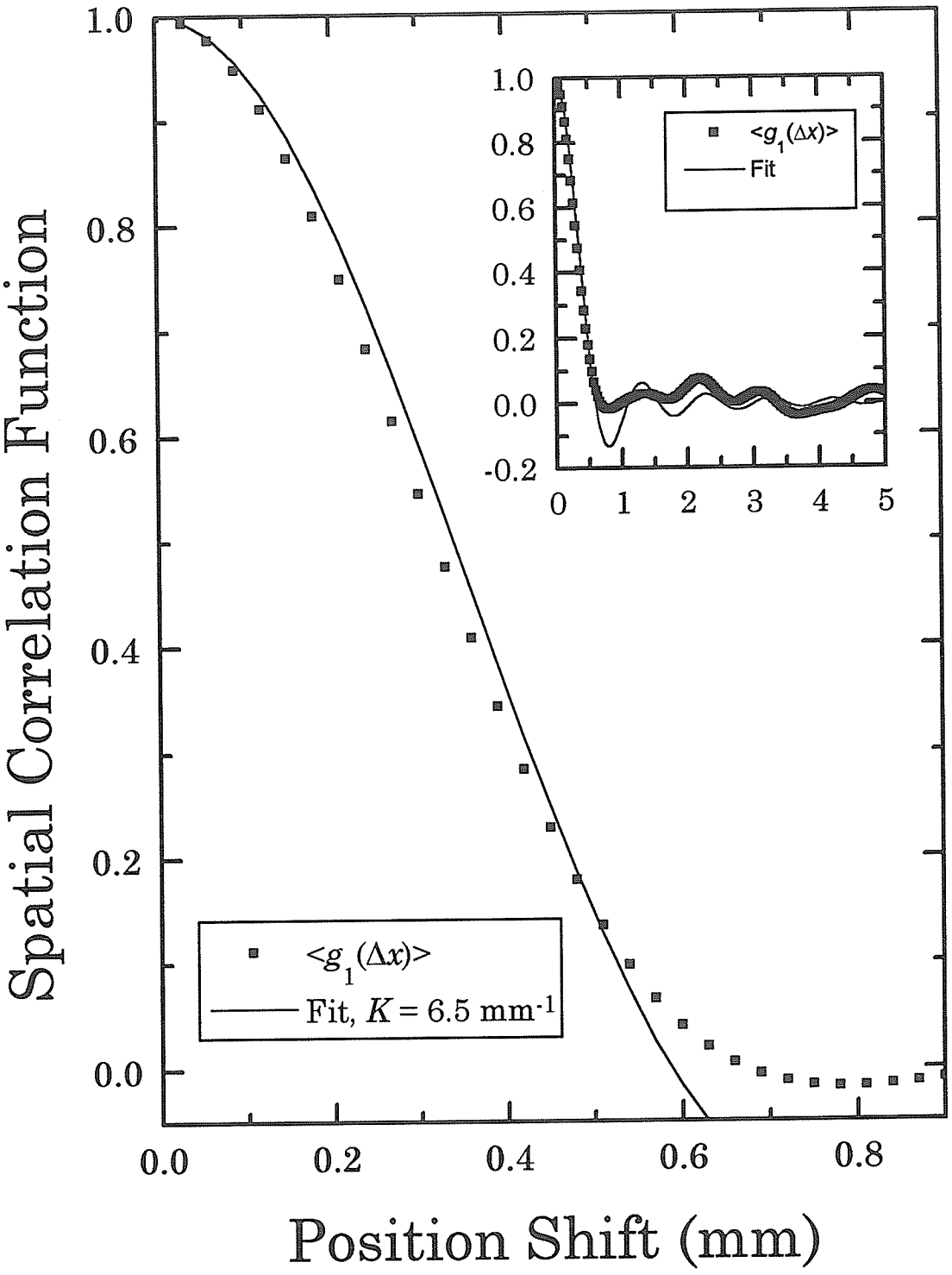

Figure 4.23. Result of fitting averaged correlation function to theory. Inset figure shows behavior of theory and data at larger frequency shifts. L = 10 mm, input frequency = 2.5 MHz.

by the initial decay of the correlation function, giving a reasonable description of the data and yielding a value of K of 6.5 mm^{-1}, which is roughly 60 % of our estimated value. In view of the approximations involved, this correspondence between experiment and theory is satisfactory.

We compare the field and intensity correlation functions of data taken from the L = 15 mm sample in Fig. 4.24. The field correlation function, $g_1(\Delta x)$, is found in the top panel, (Fig. 4.24a), and the intensity correlation function, $g_2(\Delta x)$ is shown in Fig. 4.24b. These figures also include the results of fitting the two correlation functions to their respective theoretical expressions. While neither fit appears to be very good, the lack of sufficient ensemble averaging limits the accuracy of the experimental results. Nevertheless the values found for K are consistent, giving values of $K \sim 5.5$ mm^{-1}, which also differs from our predicted value by roughly a factor of two. We use the two correlation functions to test the Siegert relation. This comparison is shown in Fig. 4.25, where the relationship is seen to hold.

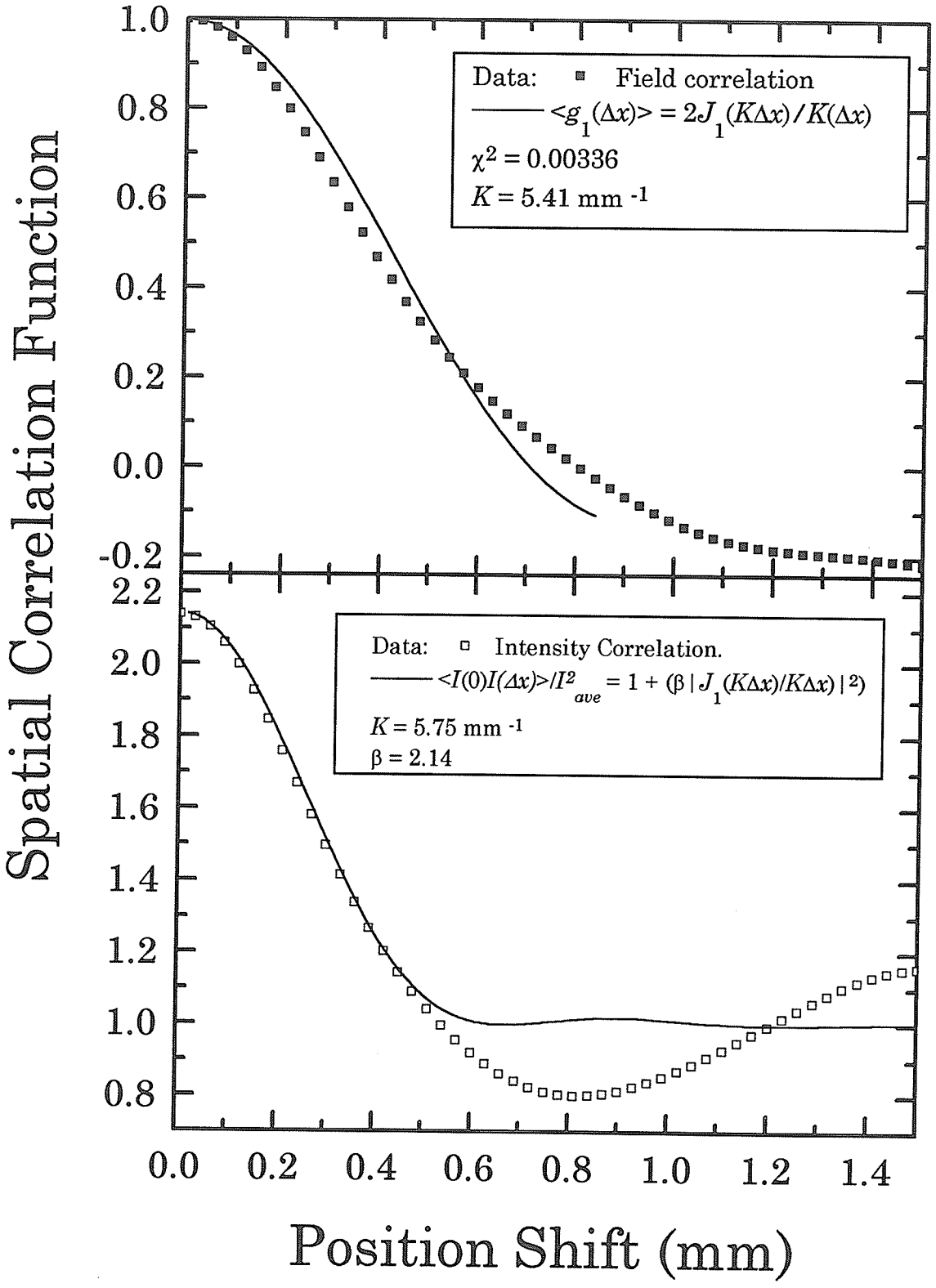

Figure 4.24. Comparison of field and intensity correlation functions, and theory. $L = 15$ mm, frequency = 2.5 MHz.

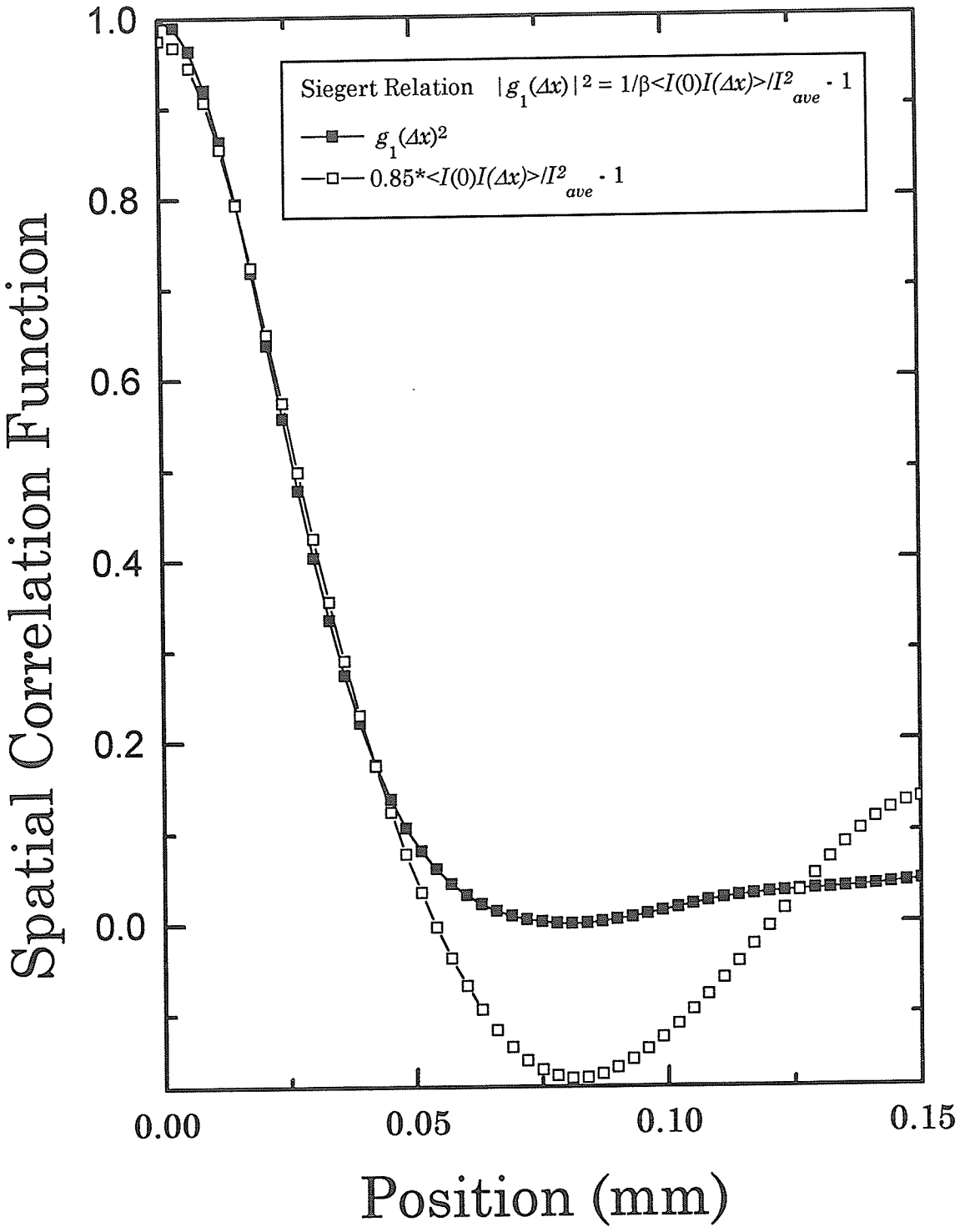

Figure 4.25. Test of Siegert relationship between field and intensity correlation functions. $L = 15$ mm

4.3 Temporal Autocorrelation Study

In the temporal autocorrelation study, we used ultrasound to study the dynamics of scattering particles moving in a fluidized bed. Ultrasound was scattered from a slurry of glass beads in motion in a fluidized bed and detected after the scattered signals had been transmitted through the slurry. The beads were set in motion by flowing a water–glycerol solution upwards through the fluidized bed, which raised the beads and countered the sedimenting effects of gravity on the beads. By varying the flow rate of this counterflowing solution we were able to vary the occupied volume fraction of beads within the bed allowing for data to be taken at a number of volume fractions. The reason this works is that the average sedimentation velocity of the beads is concentration dependent, due to hydrodynamic interactions between beads. At low occupied volume fraction, ϕ, the beads will sediment faster. We can therefore select a particular ϕ by selecting a flow speed that is equal to the sedimentation speed for the desired volume fraction. Another parameter that affects the bead dynamics is the viscosity of the counterflowing fluid. We were able to study this by changing the percentage of glycerol in the fluid, thereby changing its viscosity by more than an order of magnitude over the course of the experiment.

Data were acquired using three separate acquisition methods, as explained in the apparatus and procedure section. Correspondingly we present the results in three sections, each one focusing on a specific method. We were interested in

determining the mean-square particle displacements, $\langle \Delta r^2(\tau) \rangle$, as a function of time, and from the slope of a plot of $\langle \Delta r^2(\tau) \rangle$ vs. time, determine the variance in the velocity, $\langle \Delta V^2 \rangle$. To achieve this, the field correlation function, $g_1^{(t)}(\tau)$, was calculated from the data, and from this we could determine $\langle \Delta r^2(\tau) \rangle$.

4.3.1 Full Waveform Measurements (*fast-frame*)

In this method, data were collected for sound transmitted through the fluidized bed when the input waveform was a train of short pulses. We focused our attention on a several-μs-long portion of the scattered field after each incident pulse. By employing a segmented memory feature, called *fast-frame*, in our digitizing oscilloscope, we concatenated these sections into a single record. This allowed us to rapidly acquire data, in the form of a series of 'snapshots' of a portion of the scattered signal. The maximum number of snapshots we could concatenate into a single record was 910, with each snapshot containing 50 points.

In Fig 4.26, we show five such snapshots, or frames. The temporal width of each frame is 2 μs, representing the scattered field in the 2 μs that follows the triggering of the oscilloscope. The trigger of the oscilloscope was delayed with respect to the time at which the input pulse, of width ~ 6 μs, impinged on the sample by an amount of time that was long enough to allow the ballistic signal to pass through the system. This meant that each frame represented a portion of the scattered field, rather than a mixed signal containing some ballistic signal and some

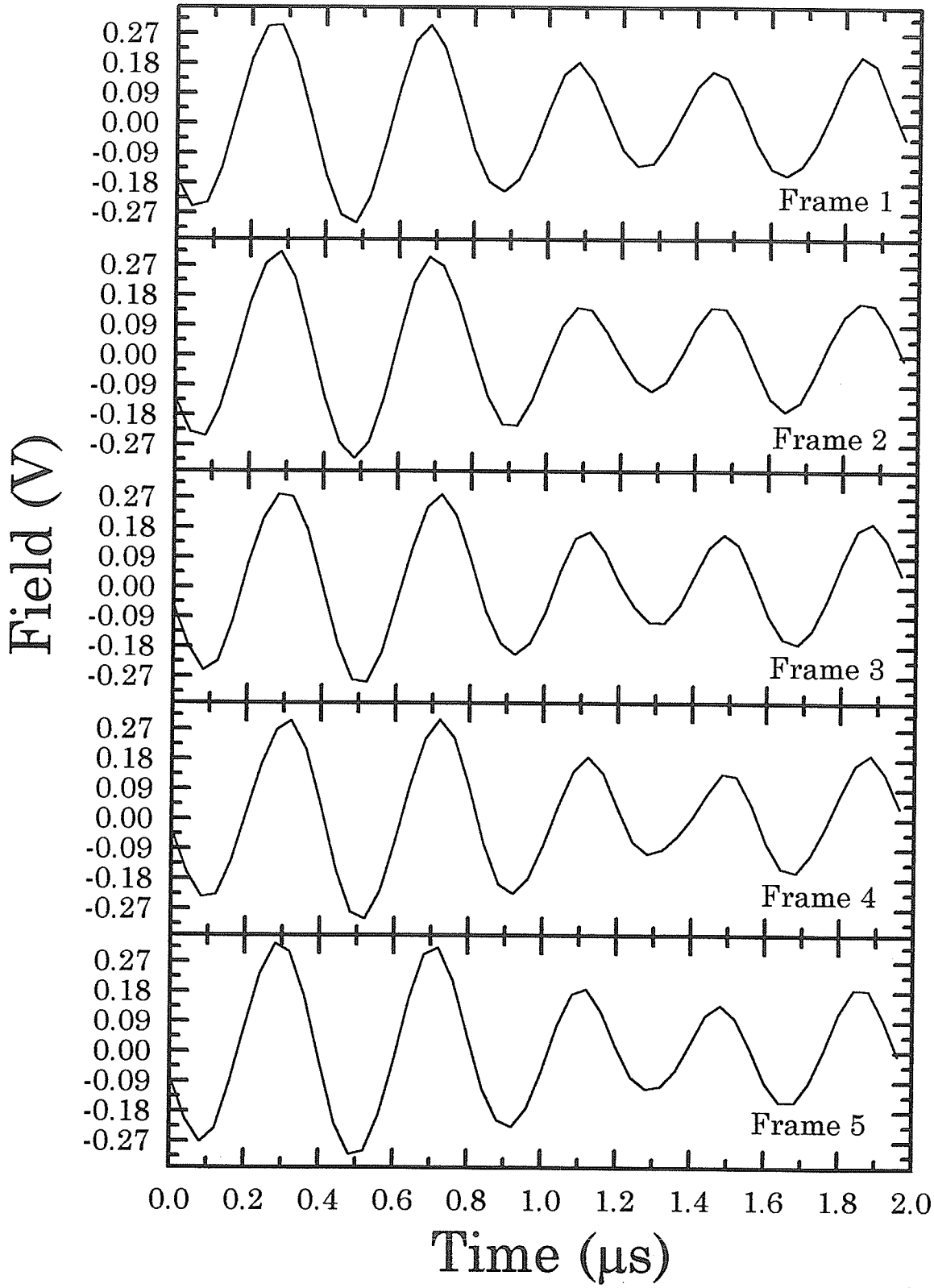

Figure 4.26. *Fast-frames* showing scattered fields from five sequential input pulses, separated by 13.97 ms. These data were taken with $\phi = 0.11$, $\eta = 198$ cP.

scattered signal. These data were recorded with an occupied volume fraction, or density of beads of $\phi = 0.11$, using, as a counterflowing fluid, a 90% glycerol solution which had a calculated viscosity of $\eta = 198$ cP. These five frames show the scattered signal in response to five sequential input pulses, with each pulse separated by 13.97 ms. Over these five frames we see very little variation in the scattered signal indicating that the 13.97 ms interval between frames is sufficiently short that small changes in the scattered field can be measured. In Fig. 4.27, we show five more frames from the same record; in this case however, the separation between frames is 20 input pulses, or 0.28 s. Now we see the variation between frames is more pronounced, particularly in frame 40, at ~1 μs, where the scattered signal has destructively interfered to the point where it is tiny.

One advantage of collecting data in this method is that we were able to extract, from these frames, snapshots of the amplitude and phase of the scattered signal, within the time window covered by each frame. This allows us to calculate both field and intensity correlation functions, in a method analogous to that discussed in the previous section on spatial correlations. It also opens up a novel possibility of using phase information to directly probe the particle dynamics, although this possibility is not pursued in this thesis. In Fig. 4.28, we show the amplitudes of the fields that were shown in Fig. 4.26. Again we see very little variation between frames. The amplitudes are somewhat flat over the time spanned by each frame, which is expected since the frame width of 2 μs is smaller than the pulse width of 6 μs, and it is the pulse width that sets the timescale for fluctuations in the field. In Fig. 4. 29, we show the amplitudes of the fields that were plotted in

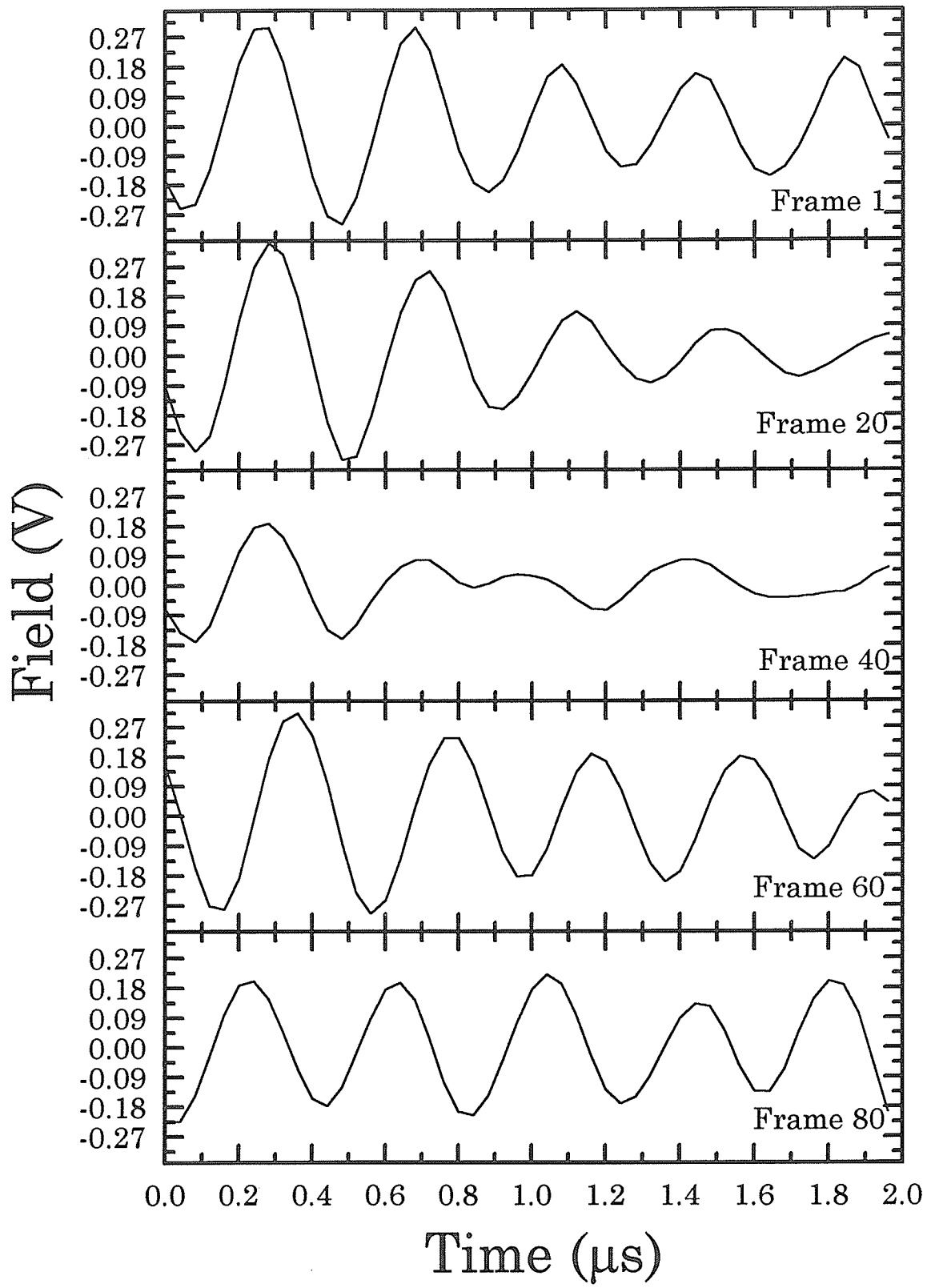

Figure 4.27. *Fast-frames* showing scattered fields from input pulses separated by 0.28s. These data were taken with $\phi = 0.11$, $\eta = 198$ cP.

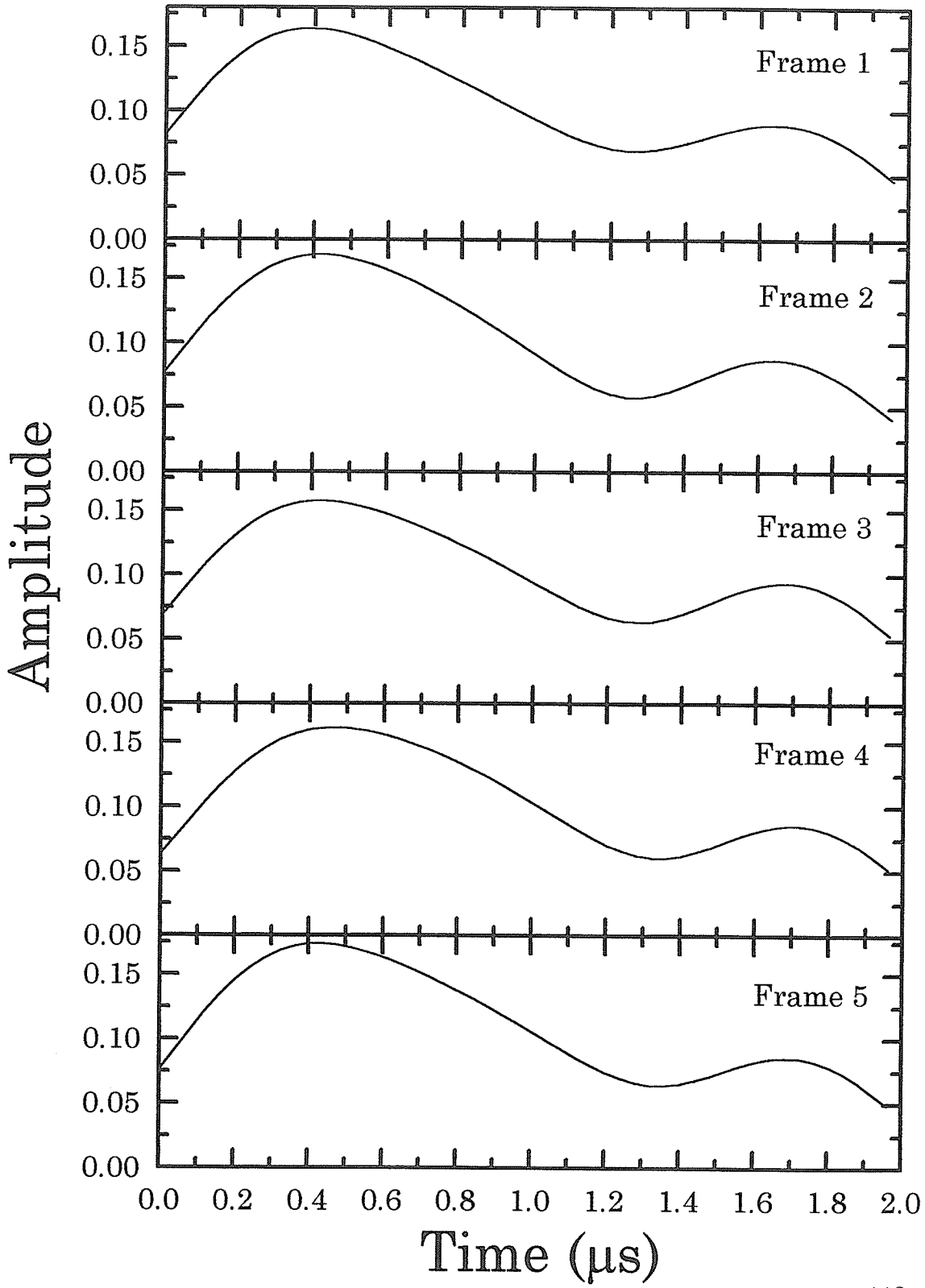

Figure 4.28. Amplitude of fields in five frames, separated by 13.97 ms. Fields corresponding to these amplitudes are shown in Figure 4.26.

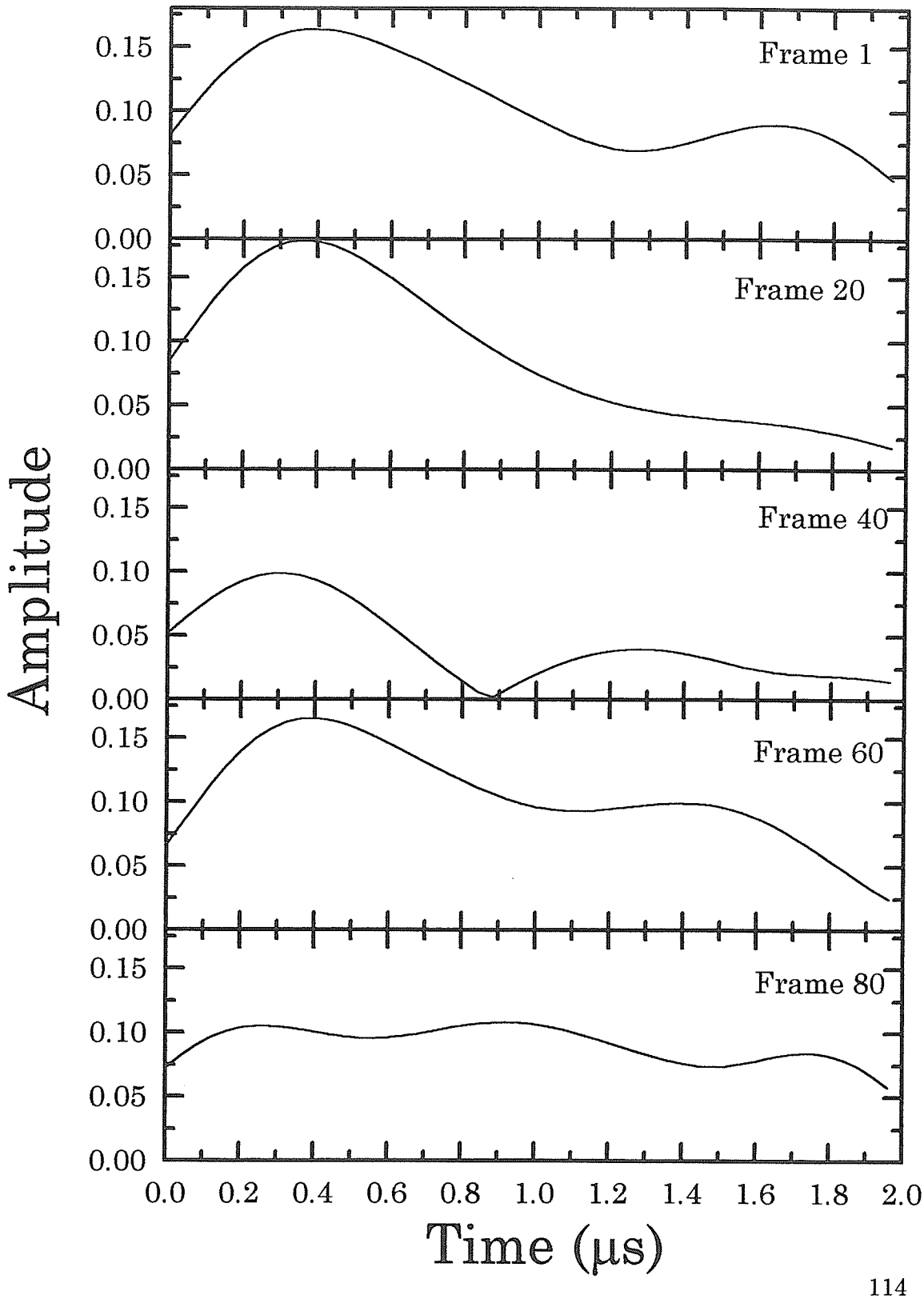

Figure 4.29. Amplitude of fields in five frames, separation of frames is 0.28s.

Fig. 4.27. We see a larger variation in amplitudes between the frames, indicating that the beads have become further displaced from their original positions, in the longer time interval between these frames.

The phase variation, for the same sequences of field frames, are shown in Figs. 4.30 and 4.31, and again we notice little variation between sequential frames (Fig. 4.30) but larger variations when the frames are separated by a longer time (Fig. 4.31).

The next step in analyzing these data is to extract the scattered field at a particular time in each frame, and construct a record consisting of the field values of all 910 frames at this chosen sampling time, $S(t)$. This is shown in Fig. 4.32, where we have chosen to examine the field at the three sampling times, 0.52, 1.0 and 1.52 μs. Evident in this plot are dramatic fluctuations in the field corresponding to the bead motion over 12.7 s. Plots corresponding to the amplitude, and phase records at these times are shown in Figs. 4.33 and 4.34. We see that the phase meanders about, getting further from its starting point as the record progresses. It is from the records of amplitude and field that we calculate the correlation functions. A summary plot with the phase, amplitude and field records, at the middle time, t = 1.0 μs, is shown in Fig. 4.35.

To determine the correlation functions from our data, we use equations similar to Eqs. (5) and (6) from the previous section on spatial correlation functions. For the field correlation function we use

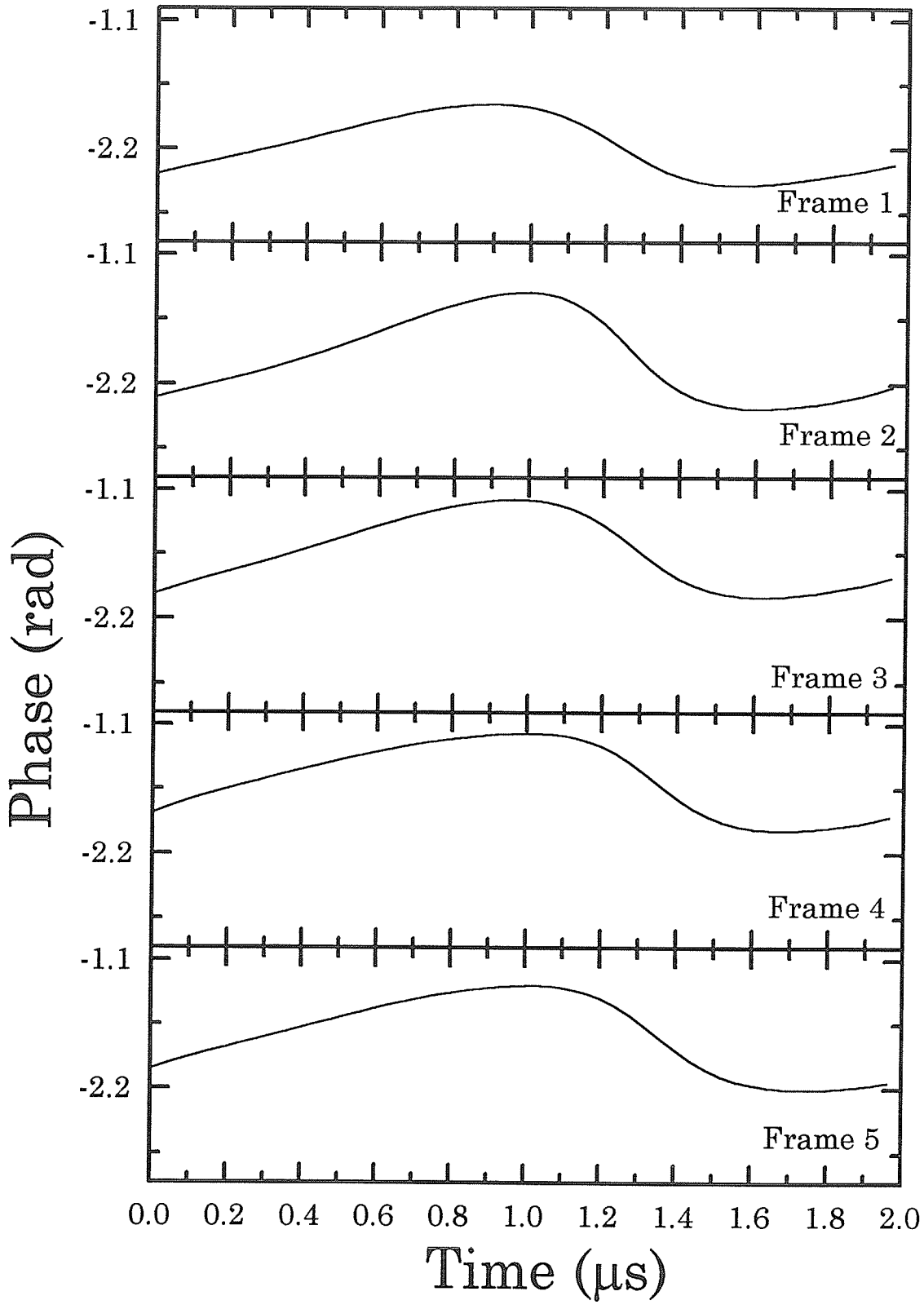

Figure 4.30. Phase of fields in five frames separated by 13.97 ms. Fields corresponding to these amplitudes are shown in Figure 4.26.

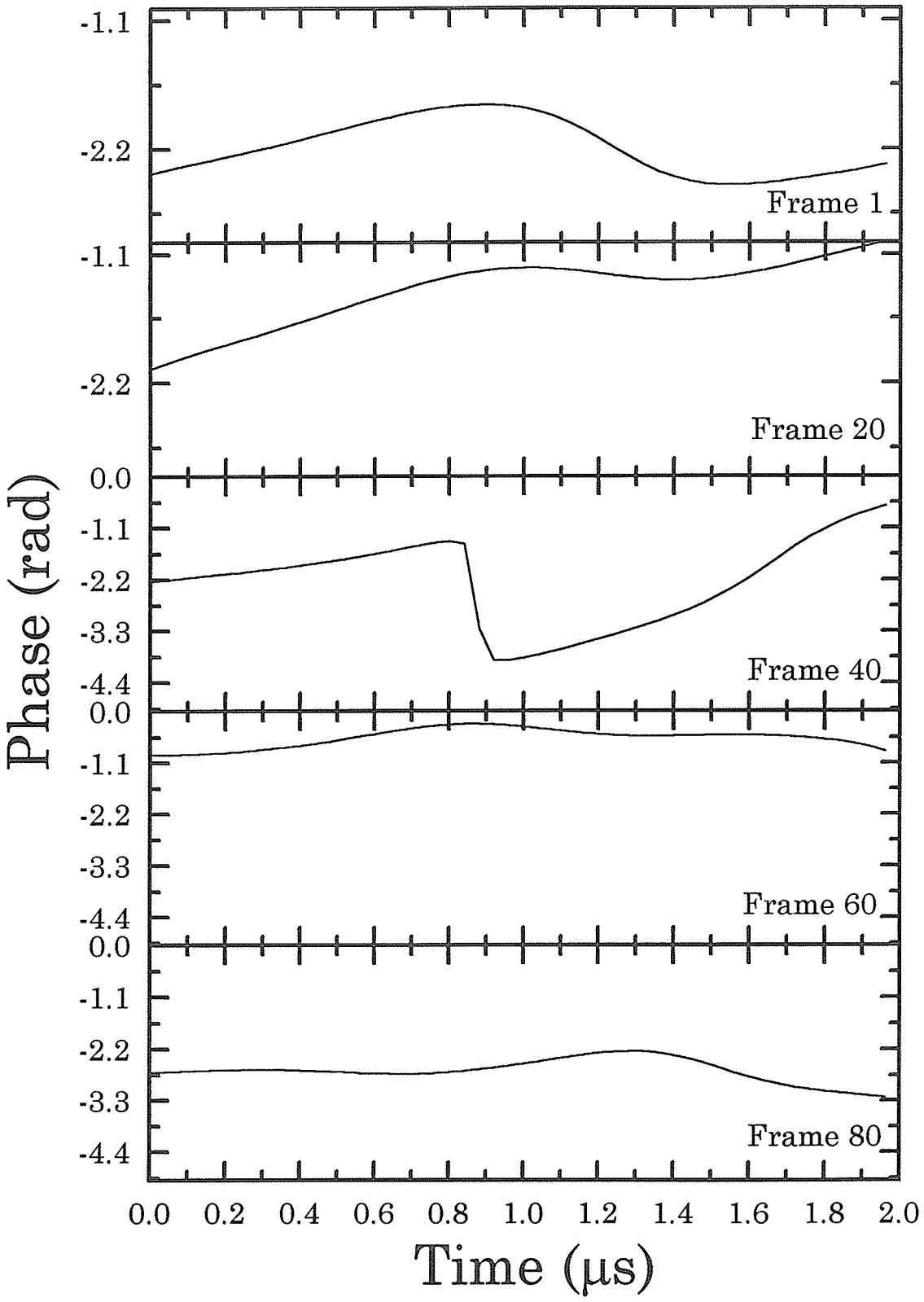

Figure 4.31. Phase of fields in five frames. Separation between frames is 0.28s.

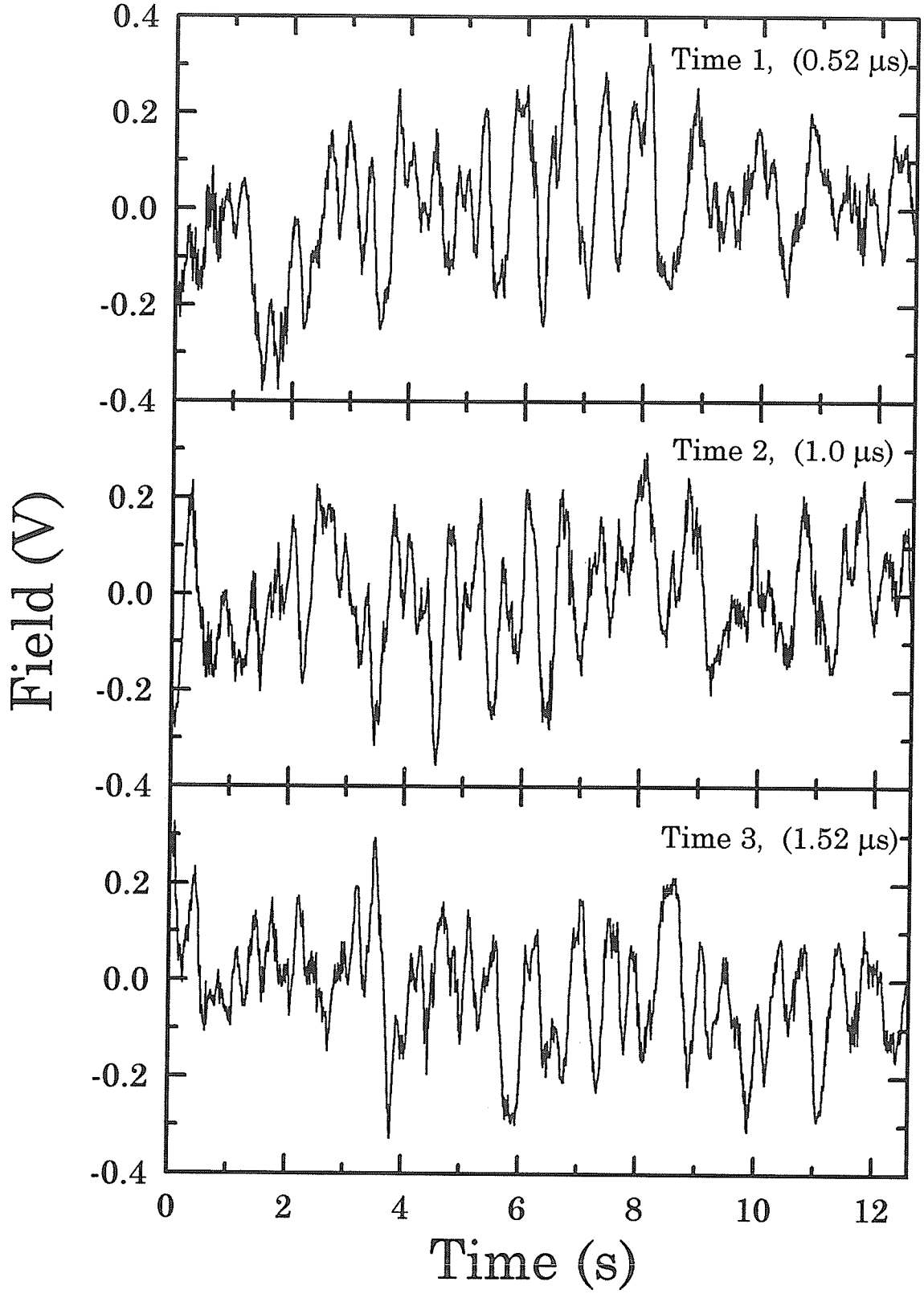

Figure 4.32. Evolution of field vs time, where each point represents the scattered field, at a particular time in the scattered signal.

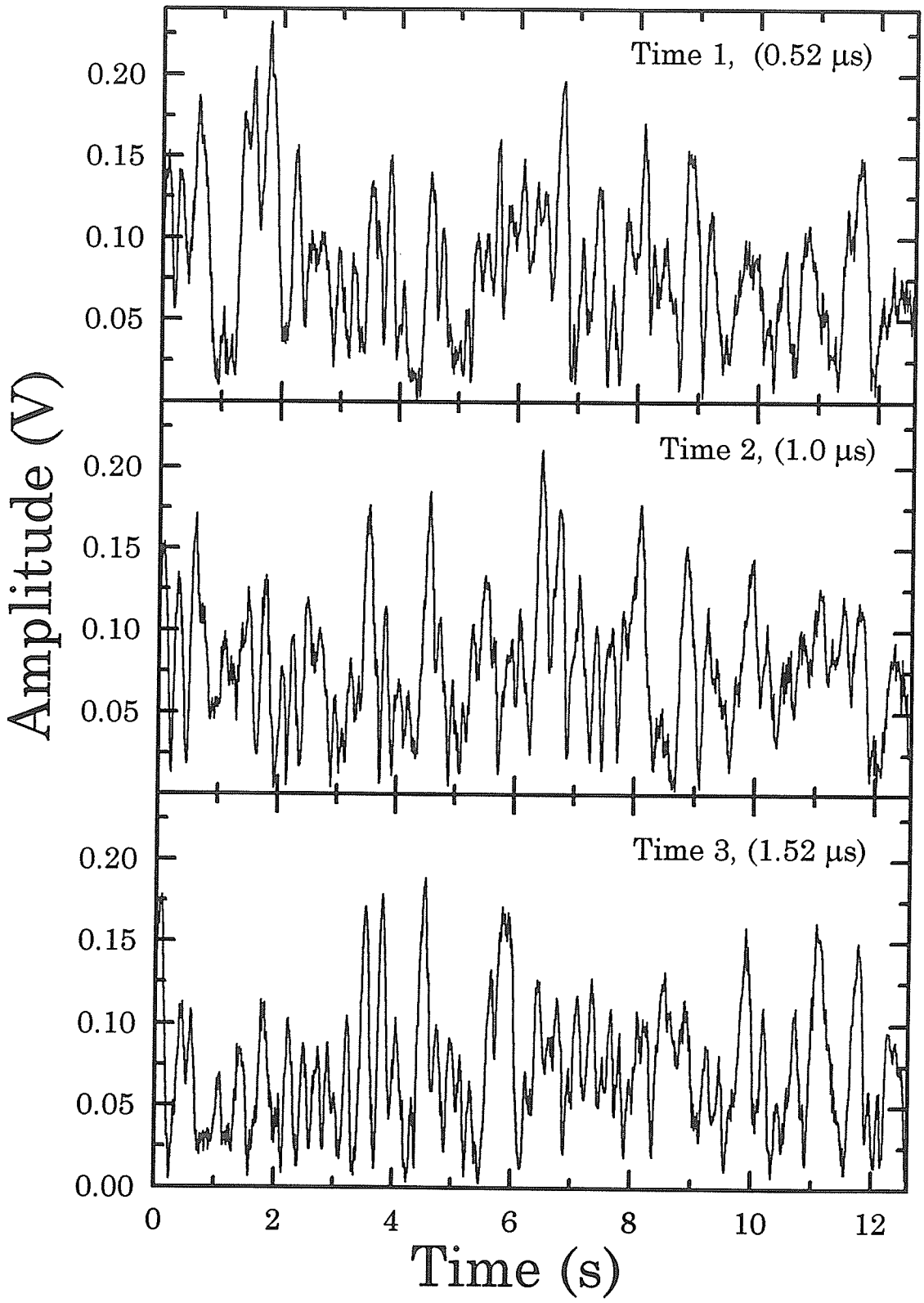

Figure 4.33. Evolution of amplitude vs time, where each point represents the scattered amplitude, at a particular time in the scattered signal.

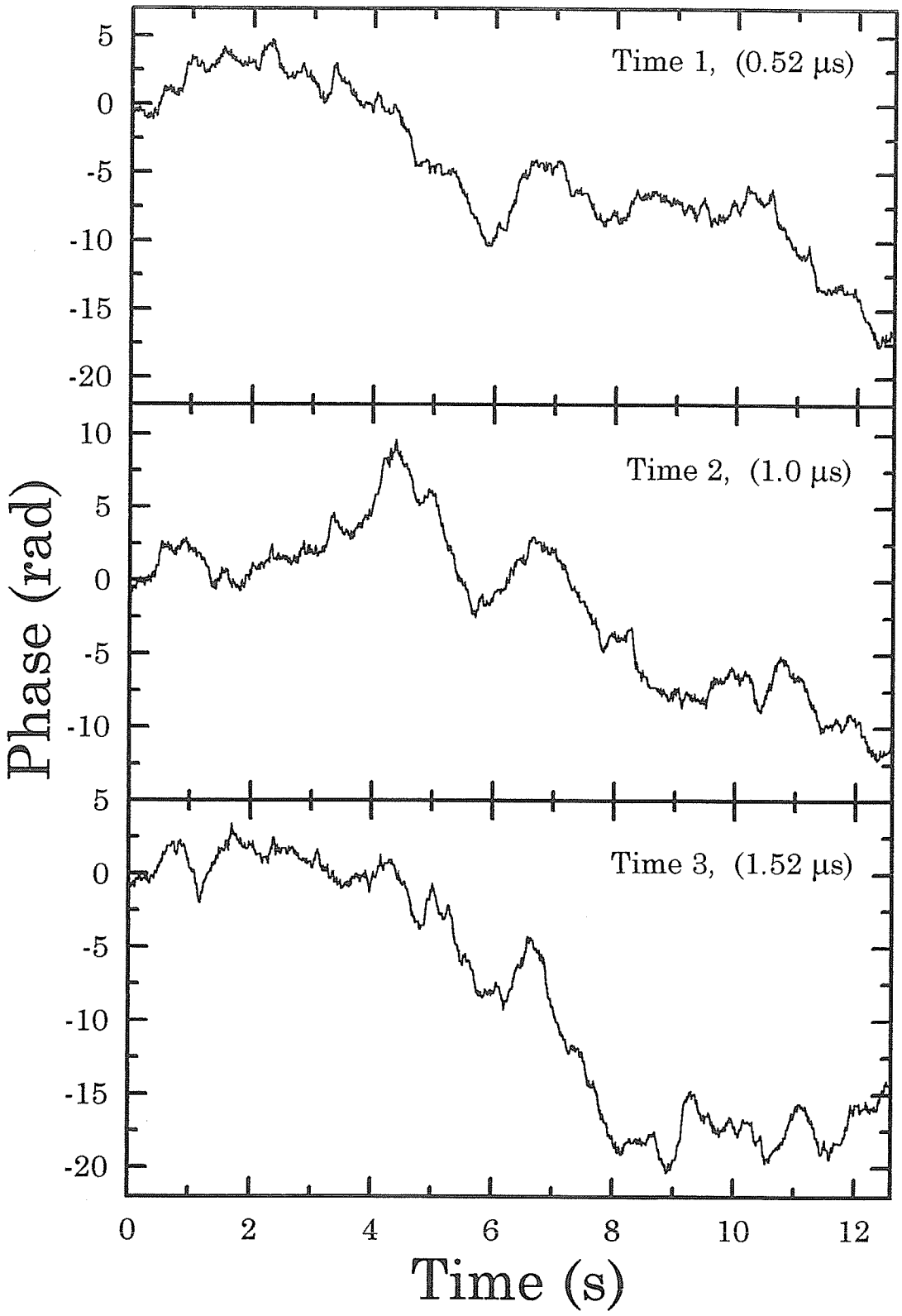

Figure 4.34. Evolution of phase vs time, where each point represents the scattered phase, at a particular time in the scattered signal.

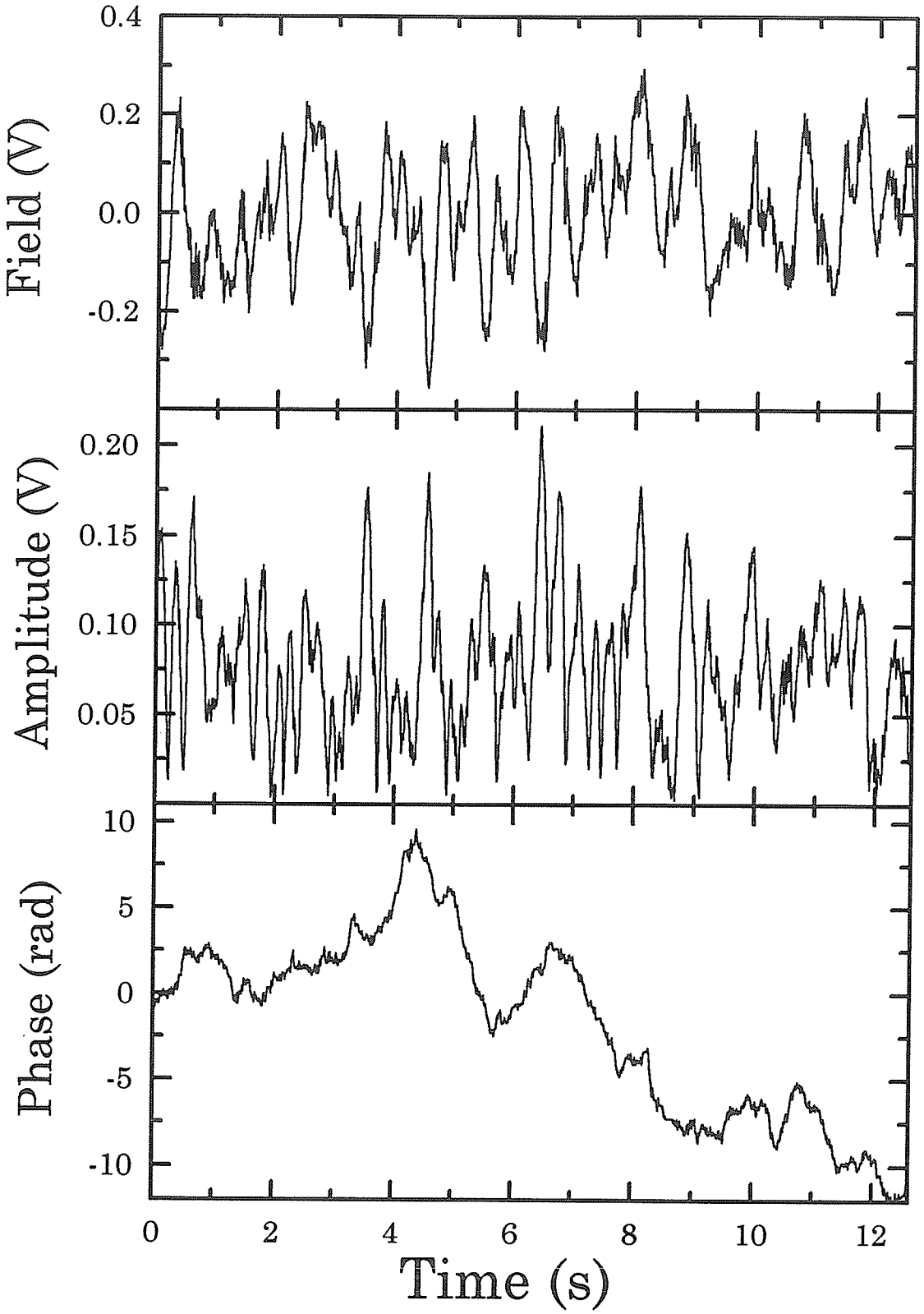

Figure 4.35. Evolution of field, amplitude, and phase vs time, where each point represents the scattered signal, at time, $t = 1.0$ μs in the scattered signal frames.

$$g_1(\tau) = \frac{1}{g_1(0)} \int S(t) S^*(t+\tau)\,dt \approx \frac{1}{g_1(0)} \sum_{j=0}^{m-i-1} \frac{S(t_j) S^*(t_j+\tau_i)}{m-i}, \tag{10}$$

where $S(t)$ represents the scattered field, m is the total number of data points and τ is the time shift, $\tau = \tau_i = i\Delta t$, with Δt being the time interval between adjacent data points, (in this case the repetition rate of the input pulses). We find the intensity correlation function using

$$g_2(\tau) = \frac{1}{I_{ave}^2} \int I(t) I(t+\tau)\,dt \approx \frac{1}{I_{ave}^2} \sum_{j=0}^{m-i-1} \frac{I(t_j) I(t_j+\tau_i)}{m-i}, \tag{11}$$

where the intensity, $I(t) = A(t)^2$, is the square of the amplitude data. We normalize by the factor, I_{ave}^2, which is the average value of $I^2(t)$, defined in Eq. (7).

In Fig. 4.36, we show these correlation functions with the intensity correlation in the top panel and the field correlation in the bottom panel. The variations between the correlation functions in each plot are attributable to noise fluctuations within each record and would be reduced if a number of independent correlation functions from each time were averaged together.

A test of the Siegert relationship, Eq. (9), between the intensity and field correlations, is demonstrated in Fig. 4.37, but the resolution of the correlation functions is limited by the number of data points in the decay of the correlation function. In order to examine faster particle dynamics, we need to acquire longer record lengths, with shorter sampling times between points in the record. In this

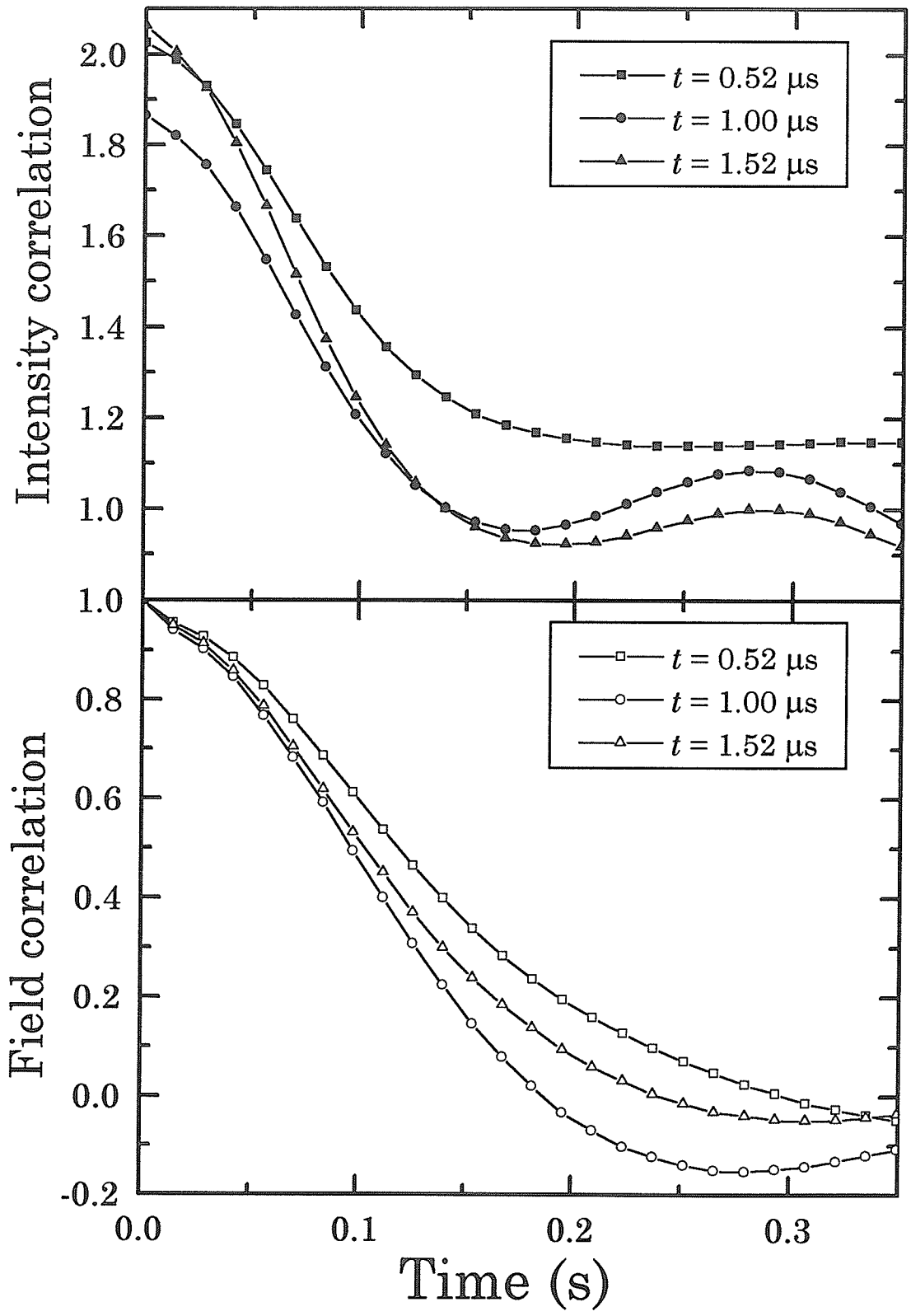

Figure 4.36. Field and intensity correlation functions, at three sampling times.

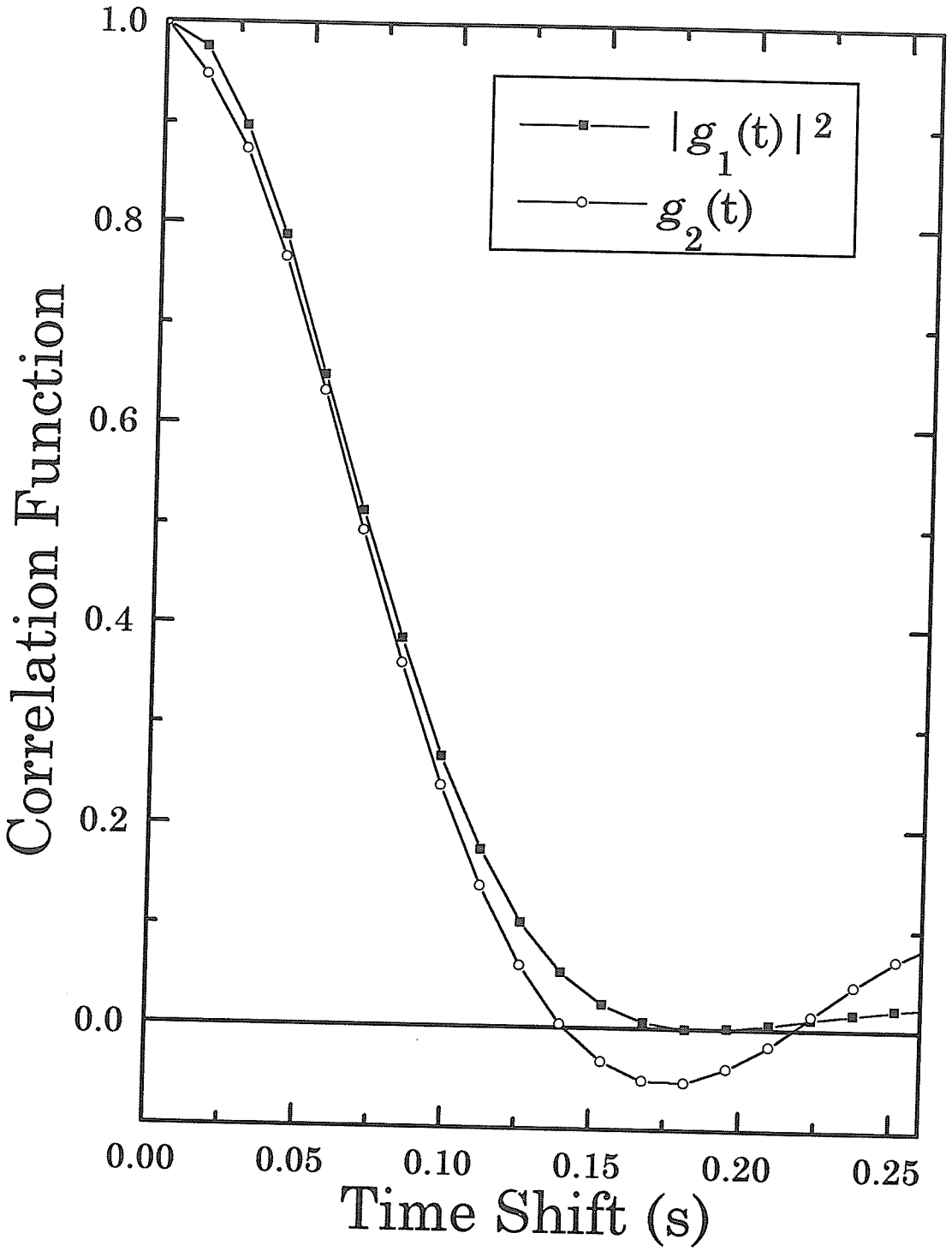

Figure 4.37. Test of relationship between the field and intensity correlation functions. The solid symbols refer to the square of the field correlation, while the hollow symbols are the intensity correlation function.

respect the fast–frame approach is limited in two ways: First the maximum number of frames that can be concatenated into a single record is too few to allow us to look at long record lengths, and secondly the maximum trigger rate of the oscilloscope determines how quickly we can sample between frames, and for fast dynamics this limit is too slow. One way of achieving shorter sampling times and longer record lengths with our existing experiment is to employ a boxcar integrator to sample the scattered signal at a single point in the diffusive time profile. This allows us to obtain long record lengths, of up to 50 000 points, which improves the accuracy with which the correlation function can be determined. The results of using the boxcar integrator are presented and discussed in the next section.

4.3.2 Boxcar Integrator

Within a system of a particular viscosity and volume fraction we could set the boxcar to collect transmitted data at some sampling time after an incident pulse had impinged upon the sample. By making this gate width smaller than the period of the field oscillations in the input pulse, we were able to examine the transmitted signal for sound that had traversed a small range of pathlengths, determined by the width of the input pulse. Concatenating the response of the boxcar to 50 000 incident pulses produced a record of the scattered sound field at the sampling time, which gave us a long record of the bead dynamics. In Fig. 4.38 we show the boxcar data recorded at three bead volume fractions in a 70% glycerol–water mixture which had a viscosity of $\eta = 25.7$ cP. A summary table of parameters relating to the data acquired using boxcar integrator can be found in Appendix 2.

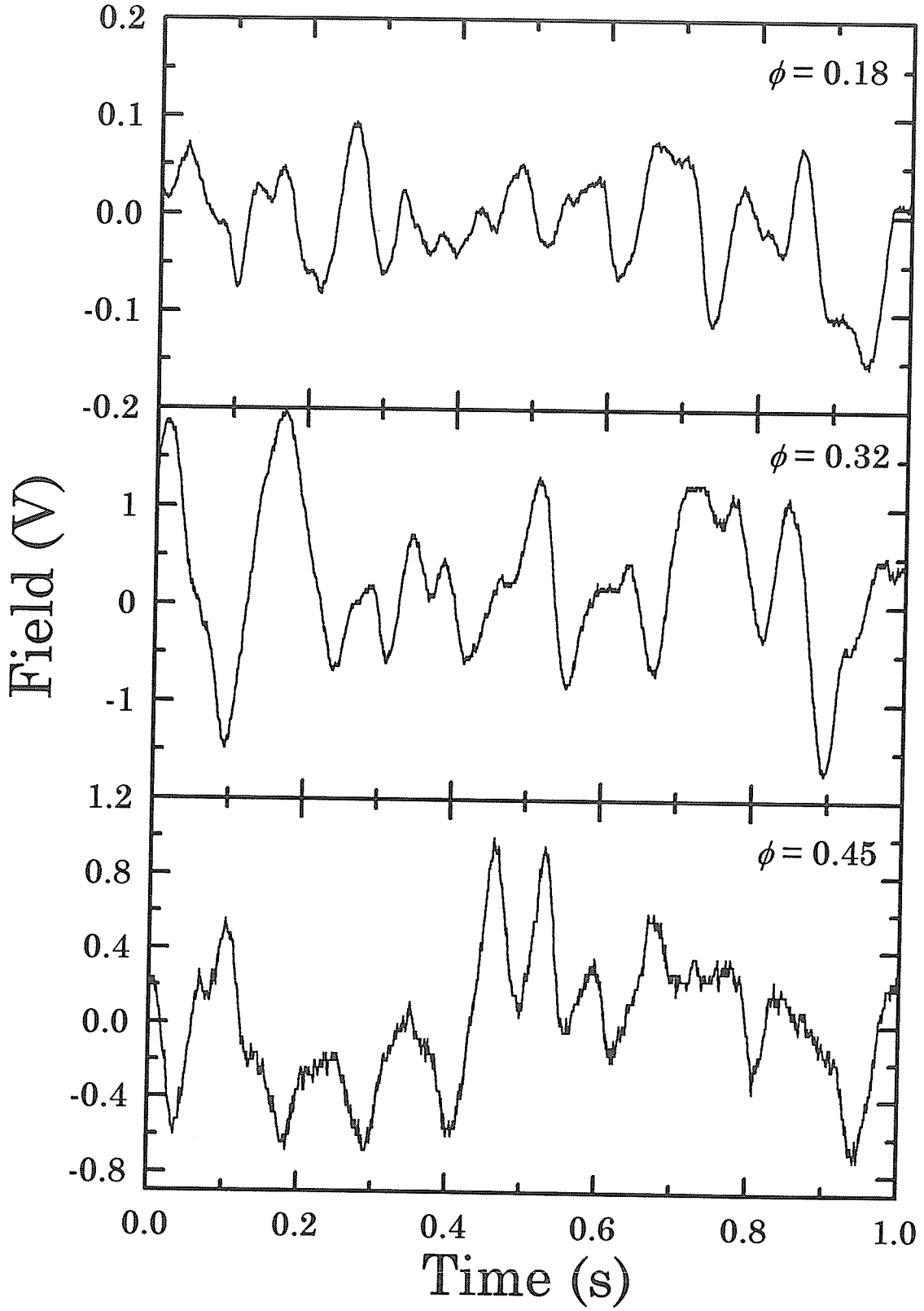

Figure 4.38. Boxcar output for three bead volume fractions ϕ. Data were recorded for a single viscosity. These plots represent a 1 second section of a total record of 50 seconds.

For these data, we used the following equation to calculate the temporal correlation function for the fields

$$g_1^{(t_s)}(\tau) = \frac{1}{g_1^{(t_s)}(0)} \int S(t) S^*(t+\tau)\,dt \approx \frac{1}{g_1^{(t_s)}(0)} \sum_{j=0}^{m-i-1} \frac{S(t_j) S^*(t_j+\tau_i)}{m-i}, \tag{12}$$

where m is the total number of data points and τ is the time shift, $\tau = \tau_i = i\Delta t$, with Δt the time interval between adjacent data points, and $t_s = s/v_E$ refers to the sampling time in the diffusion profile corresponding to a pathlength s for which the correlation function is measured.

Correlation functions calculated from the boxcar data that were shown in Fig. 4.38 are plotted in Fig. 4.39, which shows that the correlation function decays faster as the volume fraction decreases. This reflects the fact that a lower volume fraction is obtained by increasing the flow rate. For a quicker flow rate, the beads are moving faster, and the fluctuations in the field are more rapid, so that it takes less time for the beads to move far enough to cause the correlation function to decay.

We acquired data at different sampling times, each time occurring at a different point in the scattered field, measured with respect to the time at which the input pulse had entered the sample. In Fig 4.40 we show the time profile for sound transmitted through a volume fraction of $\phi = 0.18$, and viscosity, $\eta = 25.7$ cP. On this profile we indicate three times at which we sampled the scattered signal with the boxcar integrator. The correlation functions corresponding to the data collected from these three times are plotted in Fig. 4.41, which shows that the correlation

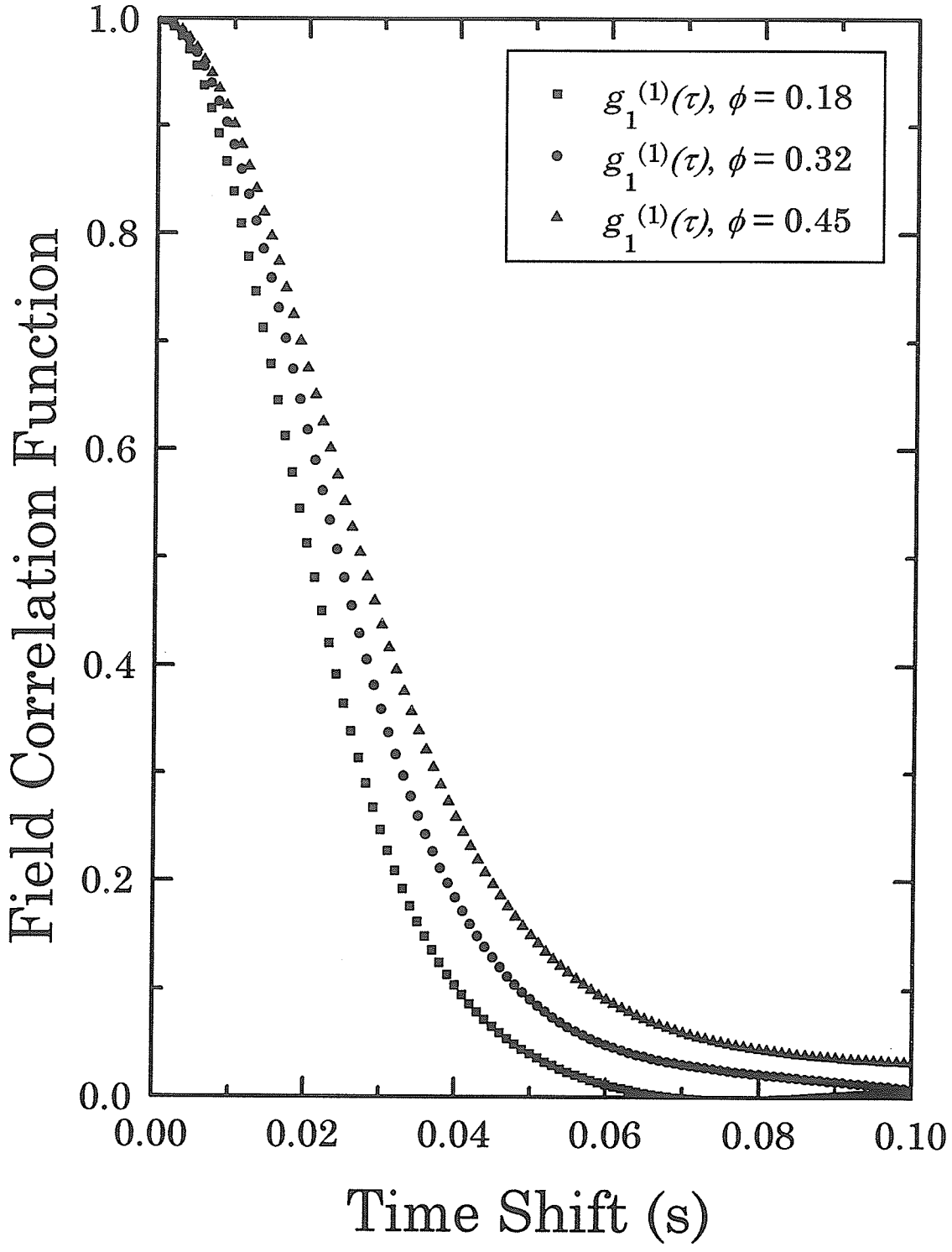

Figure 4.39. Temporal correlation functions, evaluated at same sampling time, at three bead volume fractions ϕ. Data were recorded at a single viscosity of $\eta = 25.7$ cP.

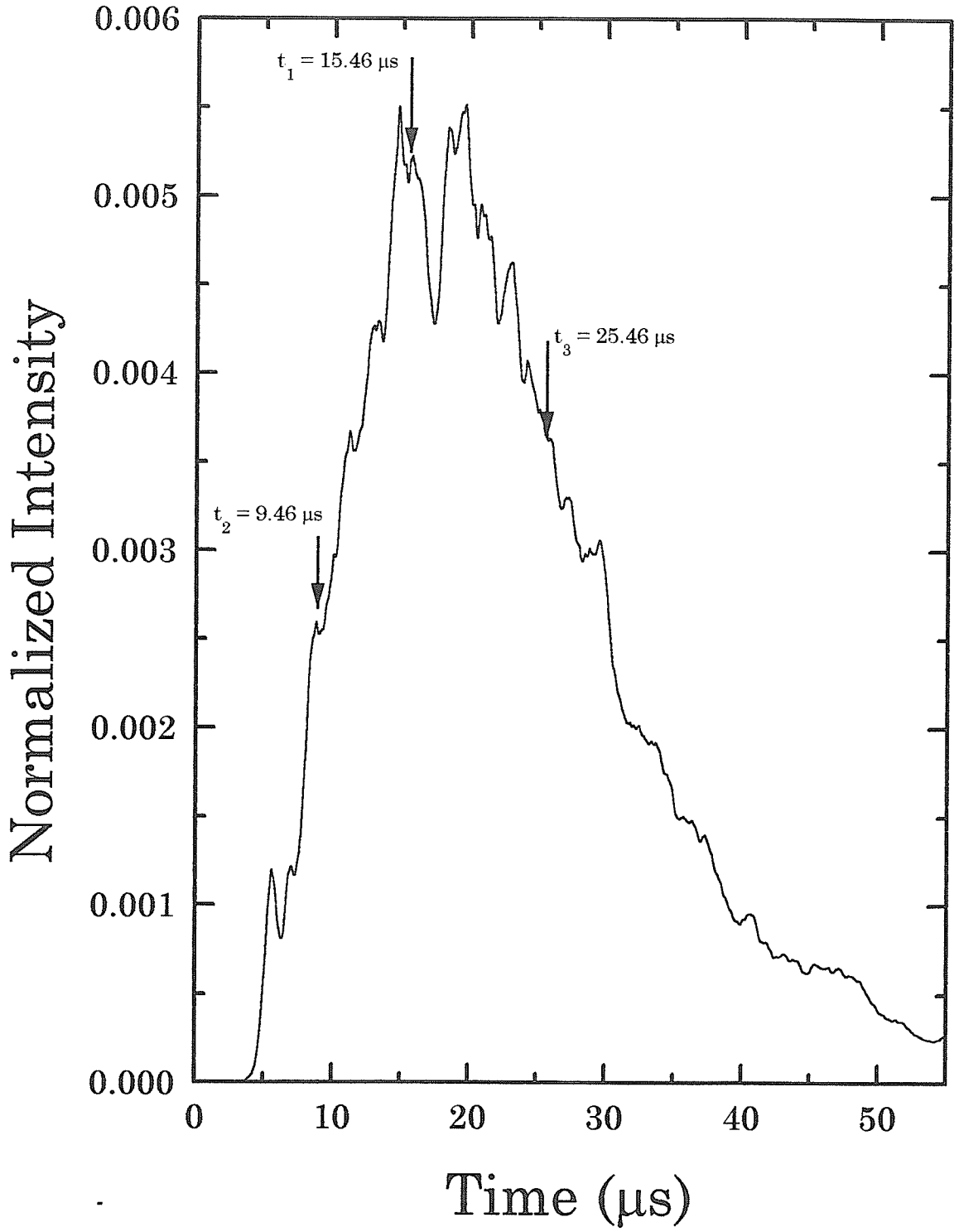

Figure 4.40. Sampling times in diffusion profile, at which boxcar data were acquired. $\phi = 0.18$, viscocity $\eta = 25.7$ cP.

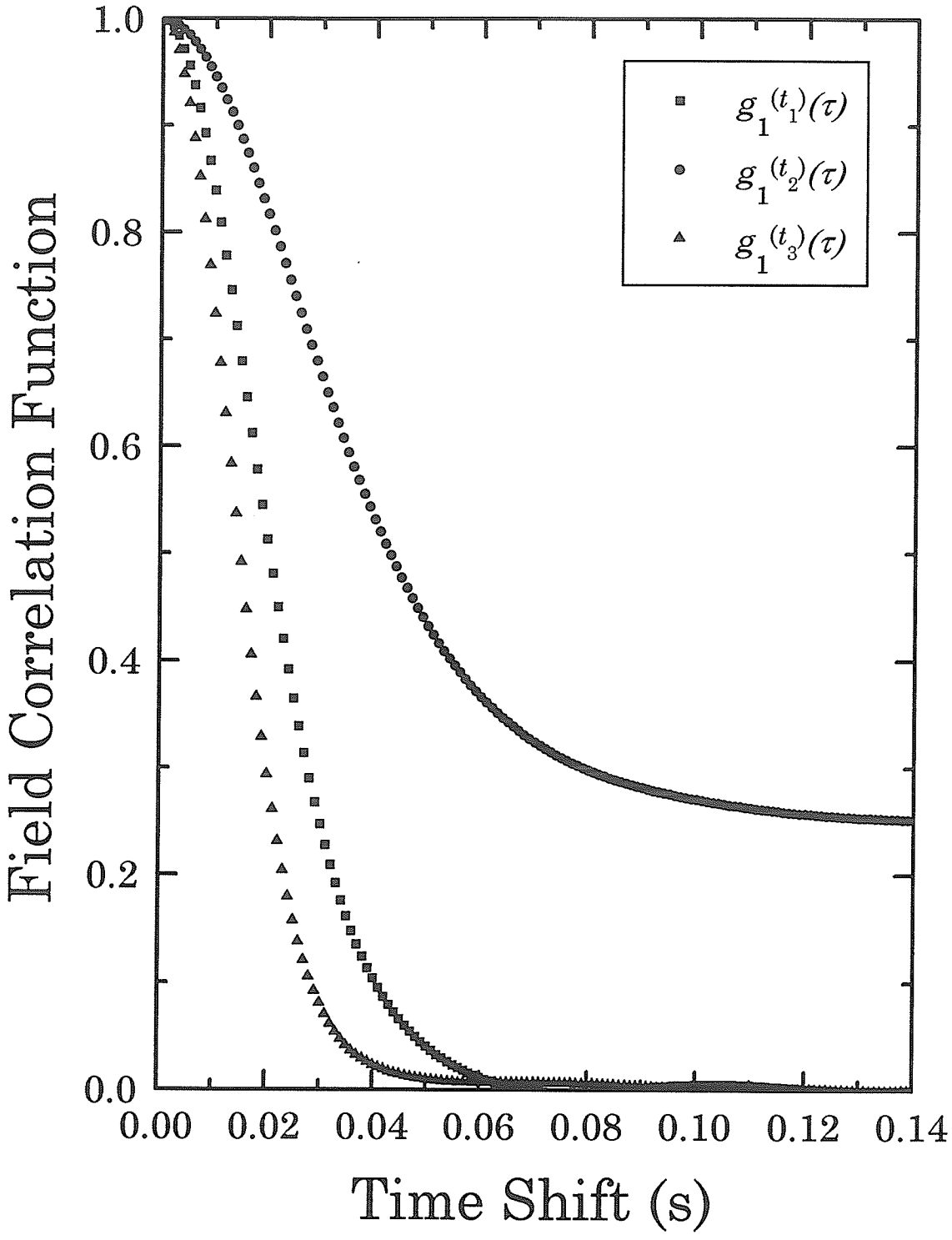

Figure 4.41. Temporal correlation functions for detected sound fields at 3 sampling times, t_1 = 15.46 μs, t_2 = 9.46 μs, and t_3 =25.46 μs . ϕ = 0.18, η = 25.7 cP.

functions decay more rapidly for later sampling times. This happens because the pathlengths represented by these times are longer and thus the beads need move a shorter distance before the sum over the pathlength of the phase shifts, contributed by each scattering event, causes the correlation function to decay to the same value. At long sampling times the correlation function has increased sensitivity for measuring small displacements of the beads, while for early times we can measure larger bead displacements before the correlation function decays to its noise background. We also see that the correlation function from the earliest sampling time, $g_1^{(t_2)}(\tau)$, levels off at a value of 0.25. This is caused by a constant background superimposed on the scattered signal that arises from sampling at such an early time in the diffusion profile that the ballistic, unscattered signal is also present. In the case of the fast–frame acquisition method it is possible to remove the ballistic from the scattered signal (as done in the frequency correlation study) but this is not feasible for the boxcar data. In general it is better to delay the acquisition time until this ballistic signal has passed through the system.

As previously explained, data were acquired for three viscosities of suspending mixture. In Fig. 4.42, we plot correlation functions from data collected at comparable sampling times in the three mixtures and demonstrate that the correlation function is strongly viscosity dependent. The most viscous, most absorbing, mixture decays much more slowly than the less viscous mixtures.

When data were taken from a system using a 90% glycerol solution, the transmitted signal was very noisy (Fig. 4.43) causing a spurious, initial, drop in the

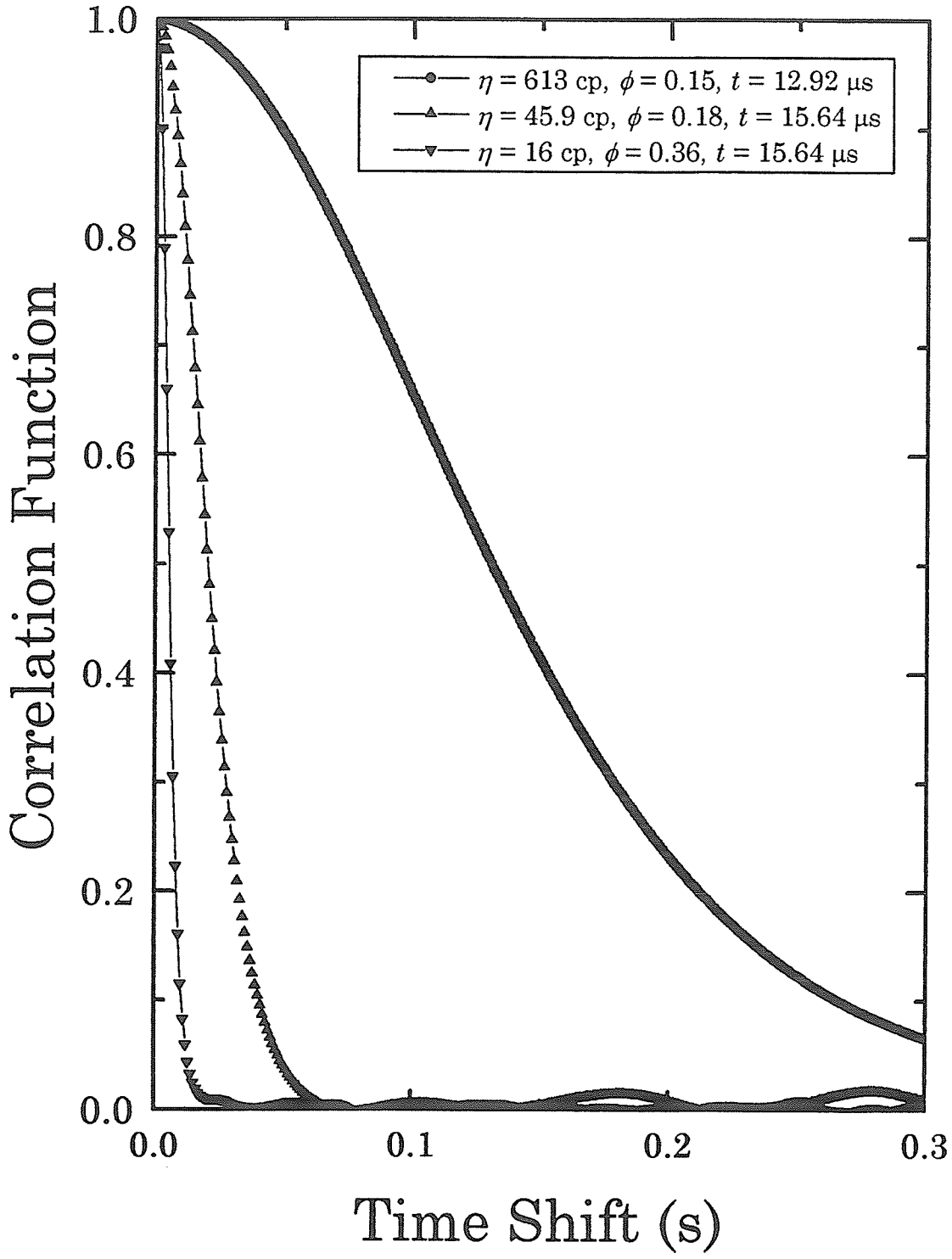

Figure 4.42. Temporal correlation functions, for three different viscosities, and bead volume fractions, at similar sampling times.

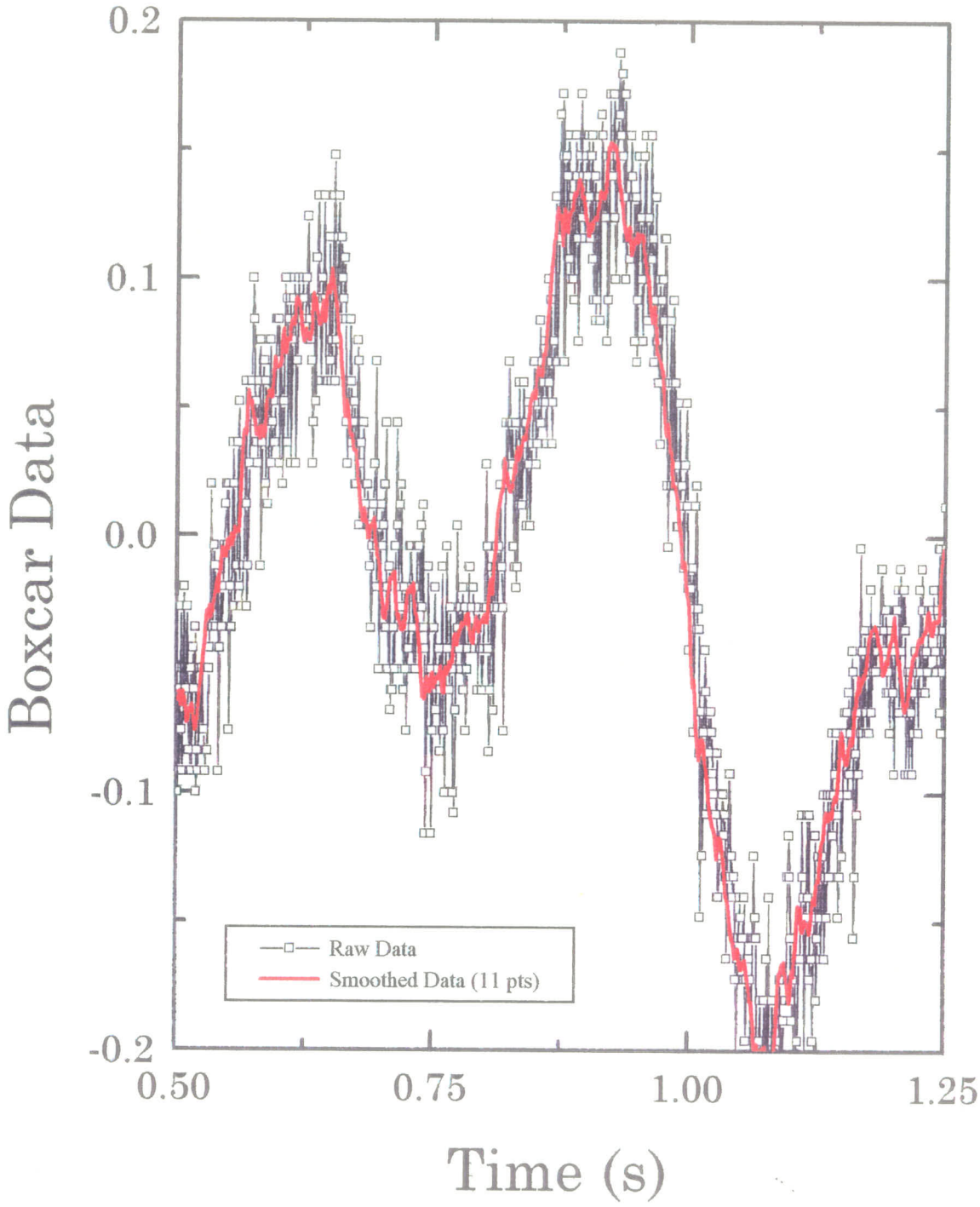

Figure 4.43. Noisy data from boxcar integrator. Also shown is a a curve resulting from averaging 11 adjacent points in the data. $\phi = 0.11$, $\eta = 198$ cP.

correlation function before it began to decay smoothly, as shown in Fig. 4.44. To remove this drop from the correlation function we employed the two methods as illustrated in Fig. 4.45. The first method used adjacent averaging to smooth the boxcar data. The results of using this averaging process have already been shown in Fig. 4.43, where the average was calculated over 11 points. The correlation function resulting from this averaged signal is represented by the open circles shown in Fig. 4.45, and we see that, while the sudden jump has been removed, there is little effect on the later part of the correlation record. This can be seen in the inset plot of Fig. 4.45 where the original data is plotted along with the correlation functions that have been found using the two methods. The limitation of the first method comes from determining the number of points over which to perform the adjacent averaging: if we choose too few, the signal is still noisy, while choosing too many points causes information to be lost. The second method attempts to remove this uncertainty. In this method we extrapolated the correlation function back to its vertical axis intercept, and then renormalized the data by this intercept. The extrapolation is achieved by fitting the first few points of the decay of the correlation function to a decaying exponential of the form $y = Ae^{-b\tau^2}$. This fitting process is also shown in Fig. 4.45 where the original data are plotted using the open square symbols, the fit is the straight line, and the renormalized correlation function is represented by the dashed line. The inset plot shows that the two methods are equivalent, and since it is easier to perform the adjacent averaging over a small number of points this is the method used for our analysis of these noisy data.

To determine quantitative results regarding the bead displacements, we use

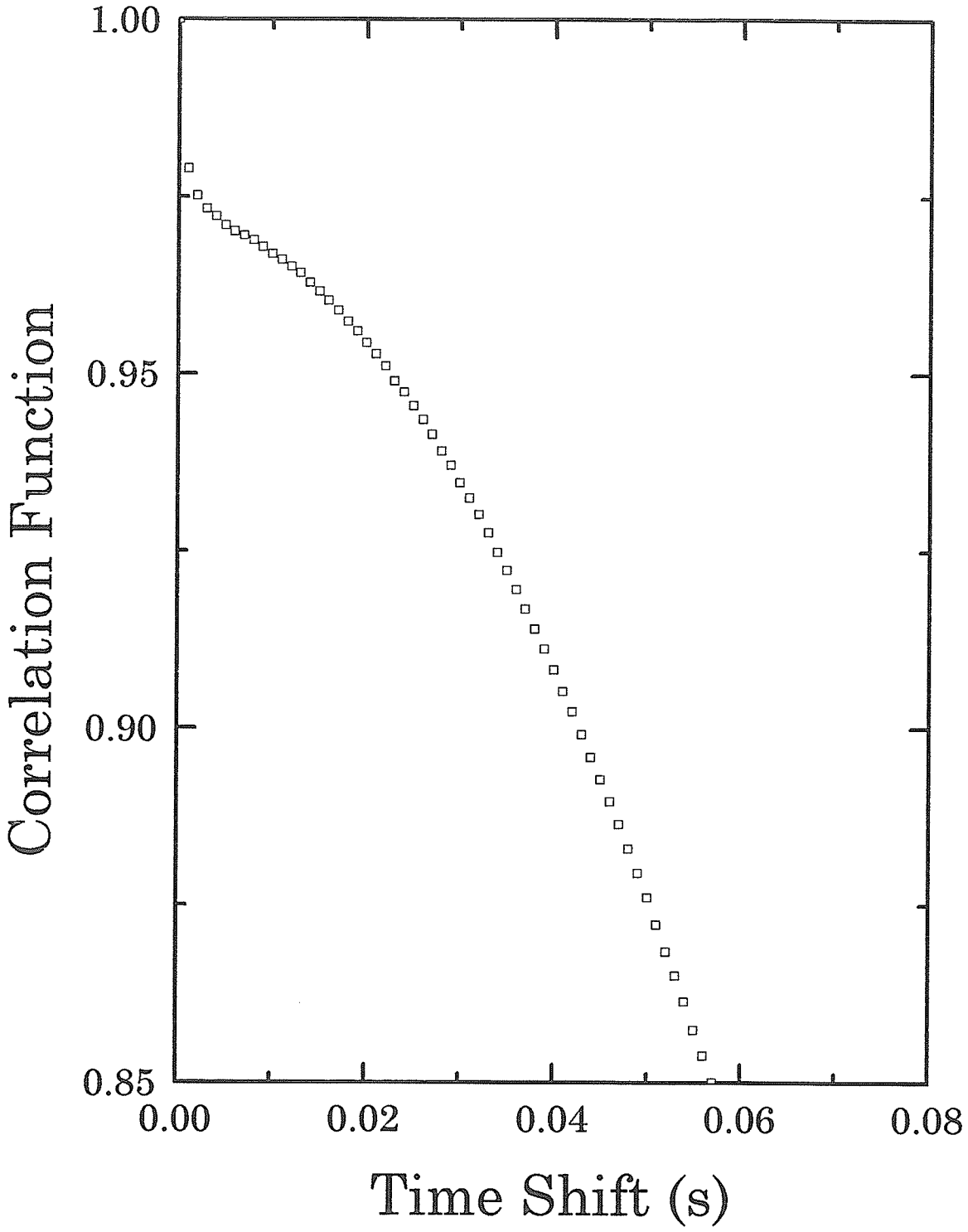

Figure 4.44. Correlation function calculated from noisy data.
The first points exhibit a sudden drop from unity before decaying smoothly.
$\phi = 0.11$, $\eta = 198$ cP.

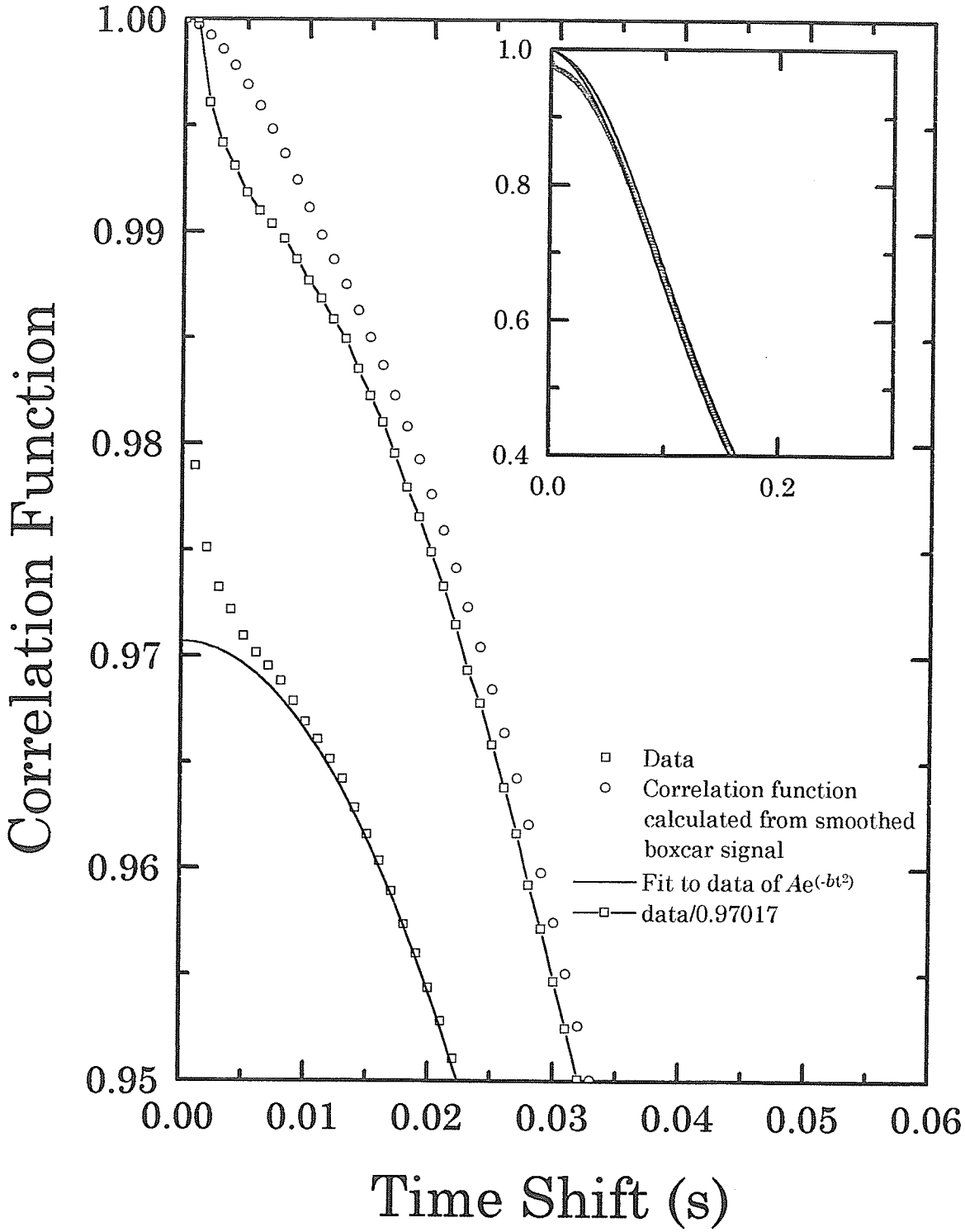

Figure 4.45. Removal of sudden drop from correlation function caused by noise in data. The main plot highlights the sudden drop, and also shows the methods used in its removal. The window shows the effect, over a larger range, on the correlation function of removing the drop, using the two methods.

$$g_1(\tau) = \exp\left(-\frac{s}{3l^*}k_0^2\left\langle \Delta r^2(\tau)\right\rangle\right) \tag{13}$$

to interpret the measured temporal field correlation functions. This can be written in terms of measured quantities in our experiment using $s = v_E t_s$, where v_E is the energy velocity of the sound transmitted through the sample, t_s is the sampling time at which the field is measured in the diffusion profile, $l^* = 3D/v_E$, and $k_0 = 2\pi f / v_p$. Thus the mean square displacement is given by

$$\begin{aligned}\left\langle \Delta r^2(\tau)\right\rangle &= -\frac{v_p^2}{v_E^2}\frac{9D}{4\pi^2 f^2 t_s}\ln\left[g_1(\tau)\right] \\ &\approx -\frac{v_p^2}{v_g^2}\frac{9D}{4\pi^2 f^2 t_s}\ln\left[g_1(\tau)\right].\end{aligned} \tag{14}$$

The second equation makes use of the approximation $v_g \approx v_E$ [3] which has been shown experimentally to be a good approximation for sound propagation through randomly packed suspensions of glass beads in water. Eq. (14) expresses the correlation function in terms of quantities for diffusing sound that can be directly measured experimentally.

We therefore need to obtain values for v_p, v_g, and D for each viscosity and volume fraction. To measure these parameters, we first analyze the ballistic, or unscattered component of the signal transmitted through the sample, which allows a value of the group velocity to be determined [1]. In Fig. 4.46a we show a ballistic waveform that is the result of averaging 100 independent transmitted waveforms (see the frequency correlation analysis for an explanation of this). For the cell thickness used in our experiment the ballistic signal is rather small, and provides a

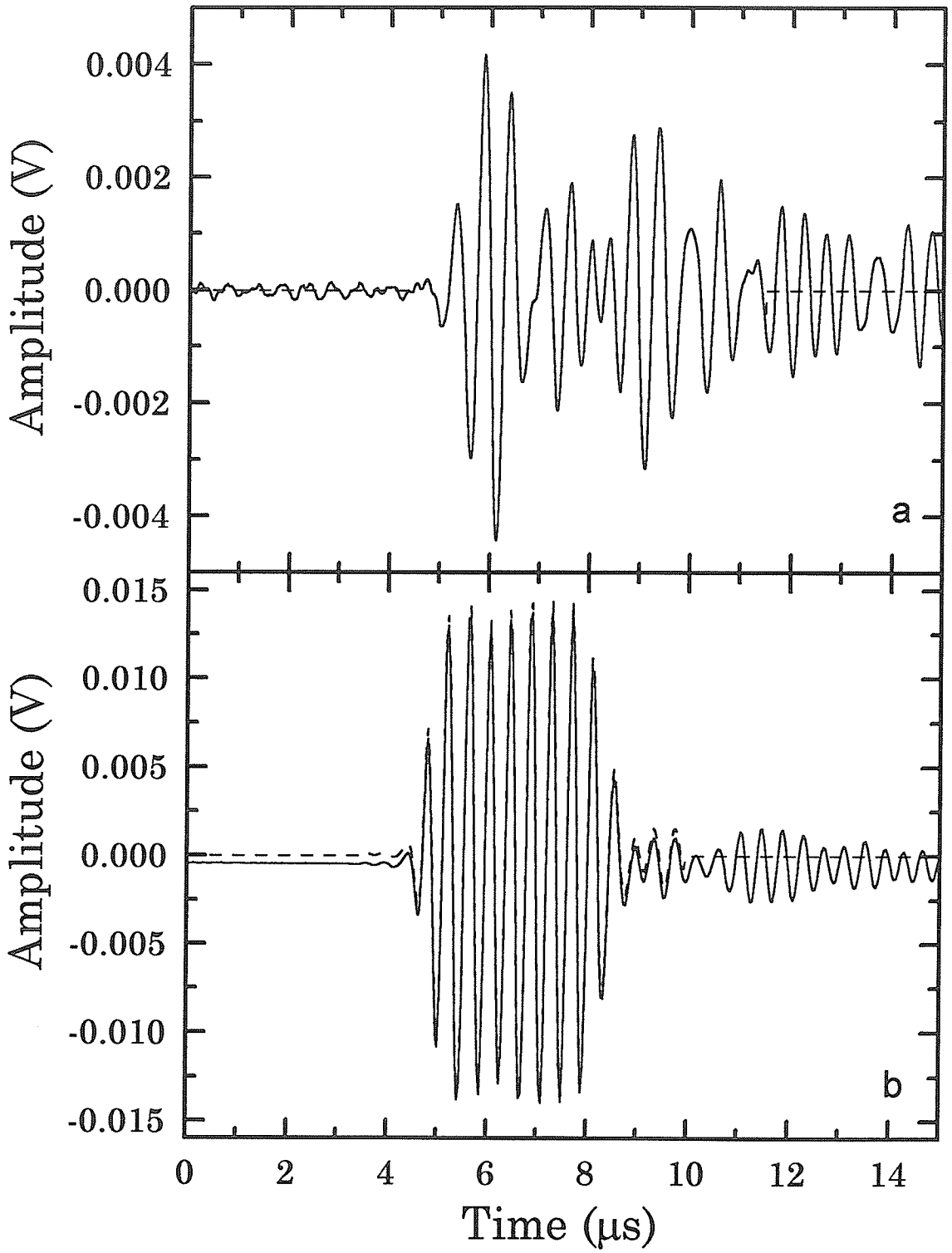

Figure 4.46. Plot showing amount of zero padding used before filtering signals used in calculation of the group velocity. The dashed lines represent the padded signal. Panel a shows the ballistic signal, panel b shows the reference signal.

particularly demanding example of the technique used in ref. [1] for measuring the group velocity in strongly scattering media. We also show, in Fig 4.46b, a signal obtained by detecting the input pulse transmitted through the fluidized bed filled only with the glycerol–water mixture. This reference signal is a representation of the original input signal used in the experiment. By calculating the slight time difference between the middle of the reference signal and the middle of the ballistic signal, we can determine the group velocity [1], since this time difference arises due to the extra transit time required for the signal to traverse the beads. Much of the ballistic signal in Fig. 4.46a appears to be dominated by low frequency components of the pulse, a result of the strong frequency dependence of the scattering mean free path in this system. It also appears that a large amount of scattered signal has survived the averaging process. To determine v_g from the centre of the signals, it is crucial to digitally filter each signal to remove the low frequency component. We apply a Gaussian bandpass filter to each signal to limit its frequency content to a range of frequencies around the central frequency of the input signal. We find this central frequency by locating the peak of the Fourier transform of each signal, as shown in Fig. 4.47. Before the transforms were calculated, the temporal extent of each signal was limited to approximately the width of the input pulse which removes the scattered signal that survived the averaging process. The truncated records are indicated by the dashed lines in Figs. 4.46 (a,b). From Fig. 4.47, we note the dominant frequency of the input signal is around 2.35 MHz. This plot also includes Fourier transforms of the filtered reference and ballistic signals, which are shown in the time domain in Fig. 4.48. The central frequency used in the bandpass

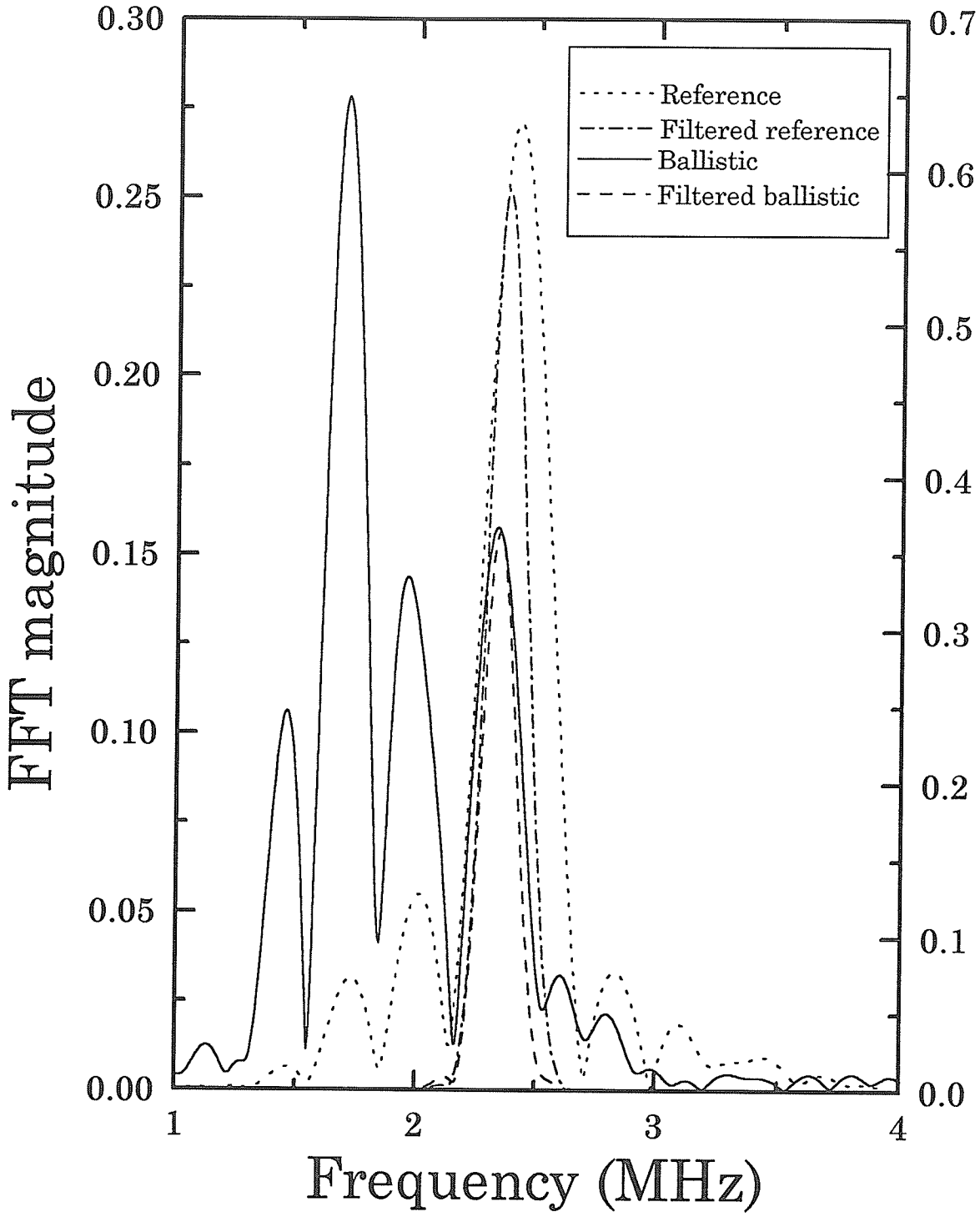

Figure 4.47. FFTs of filtered and unfiltered reference and ballistic signals. Filtering was done for a central frequency of 2.35 MHz and bandwidth = 0.2 MHz. Left axis refers to the ballsitic signals

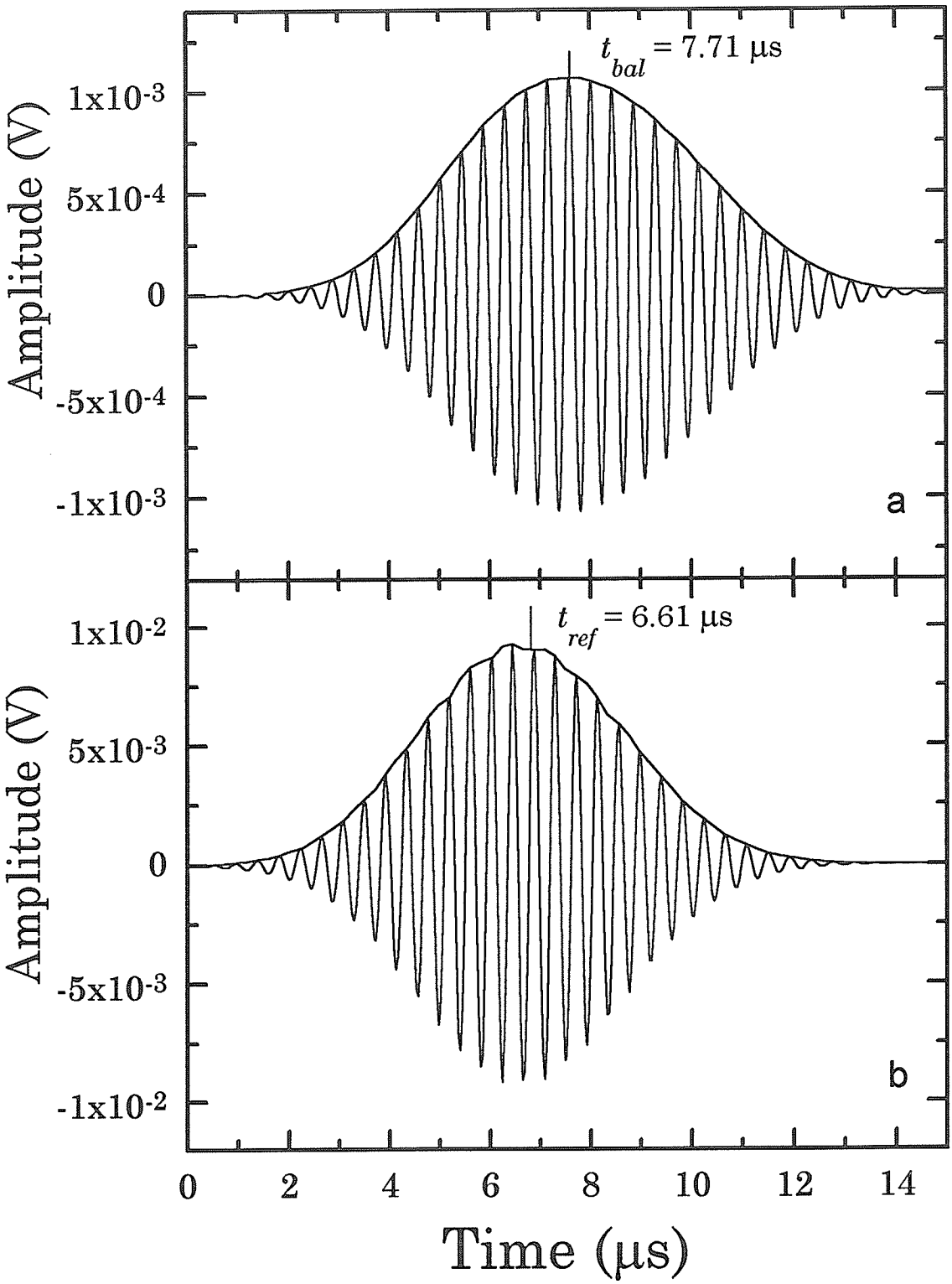

Figure 4.48. Timing diagrams used to measure the group velocity , v_g .
Panel a, shows the ballistic wave, panel b, the reference wave. The original signals were digitally filtered at a centre frequency of 2.35 MHz and bandwidth = 0.2 MHz.

filter was 2.35 MHz, and the bandwidth was 0.2 MHz. The time at the middle of each signal is marked on the graph. From the difference between these times, we can calculate the group velocity, since the time to go through the beads, t_{Beads}, must equal the time taken to go through the water-glycerol mixture, t_{w-G}, plus the measured time difference, Δt, that is

$$t_{Beads} = t_{w-G} + \Delta t. \tag{15}$$

Now $t_{Beads} = L/v_g$, where L is the sample thickness, and $t_{w-G} = L/v_{w-G}$ where v_{w-G} is the velocity of the sound in the water–glycerol mixture. Thus we calculate the group velocity from these relations and Eq. (15), using

$$v_g = \frac{L}{\frac{L}{v_{w-G}} + \Delta t}. \tag{16}$$

The water–glycerol velocity, v_{w-G}, is measured in a similar fashion except in this case the time difference arises between the centre of the pulse through the cell containing the mixture and a pulse through the water tank with no cell in place. We then use the following equations to determine v_{w-G}

$$t_{sample_{H_2O}} + \Delta t = t_{sample_{mixture}} \tag{17}$$

where $t_{sample_{H_2O}}$ refers to the time taken for sound to travel through a region of water equal to the total thickness, L_{Bed}, of the fluidized bed, and $t_{sample_{mixture}}$ refers to the transit time of sound through the sample filled with the mixture. Now $t_{sample_{mixture}} = t_{cell_{mixture}} + t_{walls}$, where $t_{cell_{mixture}}$ is the time taken for sound to travel

through the thickness, L, of the sample enclosed by the walls, and t_{walls} is the time taken for transit through the walls of total thickness d. Therefore

$$\begin{aligned} t_{sample_{H_2O}} + \Delta t &= t_{cell_{mixture}} + t_{walls} \\ \therefore\ t_{cell_{mixture}} &= t_{sample_{H_2O}} - \Delta t - t_{walls} \end{aligned} \tag{18}$$

which we rewrite using $t_{cell_{mixture}} = L/v_{w-G}$, $t_{walls} = d/v_{plastic}$, and $t_{sample_{H_2O}} = L_{Bed}/v_{H_2O}$

$$\frac{L_{Bed}}{v_{H_2O}} - \frac{d}{v_{plastic}} + \Delta t = \frac{L}{v_{w-G}} \tag{19}$$

and rearrange to isolate v_{w-G}

$$\begin{aligned} \frac{L_{Bed}}{v_{H_2O}} - \frac{d}{v_{plastic}} + \Delta t &= \frac{L}{v_{w-G}} \\ v_{w-G} &= \frac{L}{\frac{L_{Bed}}{v_{H_2O}} - \frac{d}{v_{plastic}} + \Delta t}. \end{aligned} \tag{20}$$

Measured values of v_{w-G} in the experiment ranged from 1.88 mm/μs for the 90% glycerol solution to 1.74 mm/μs for a 60% solution, while measured values of v_g ranged from 1.80 mm/μs for a 90% solution and volume fraction of 0.11 to 1.3 mm/μs for a 70% solution at volume fraction of 0.45.

In order to measure the phase velocity one finds the time difference between points in the equivalent oscillation in the two signals used to calculate v_g and uses this time difference in Eq. (6). This method, however, is limited by the ability to pick out the equivalent oscillations in the signals when the medium is dispersive requiring results from more than one sample thickness to unambiguously pinpoint

v_p. Since we had only a single thickness available in this experiment, we resorted to a theoretical determination of the phase velocity. The method used for this was developed by Page *et al.*[1], where the dispersion curve for sound propagation in a suspension of solid spheres is calculated. The calculation is made using known values for the longitudinal and transverse velocities of sound in the solid, as well as the longitudinal velocity of sound in the fluid. These velocities and the densities of the solid and fluid have either been measured or are known for the constituents of our scattering medium. In Fig. 4.49, we show the calculated phase velocity as a function of frequency for three volume fractions of beads. Here the frequency is expressed in dimensionless units $k_w a$, where $k_w a = 2\pi f / v_{w-G}$ is the sound wave vector in the fluid and a is the bead radius. The phase velocities corresponding to the central frequency in the pulse are obtained directly from this plot. This theoretical model can also be used to calculate group velocities, and these calculations can provide an indirect check on the accuracy of the theory, since we have measured the group velocities. The calculation requires that the derivative of the dispersion curve, $d\omega/dk$, be evaluated to obtain the group velocity. This has been done for our volume fractions, as shown in Fig. 4.50. From theses curves we obtain theoretical group velocities ranging from 1.33 mm/μs for $\phi = 0.45$ to 1.64 mm/μs for $\phi = 0.18$, with both calculations done for a 70% solution of glycerol. These values compare well with the measured group velocities, indicating that the values calculated for the phase velocities are also valid.

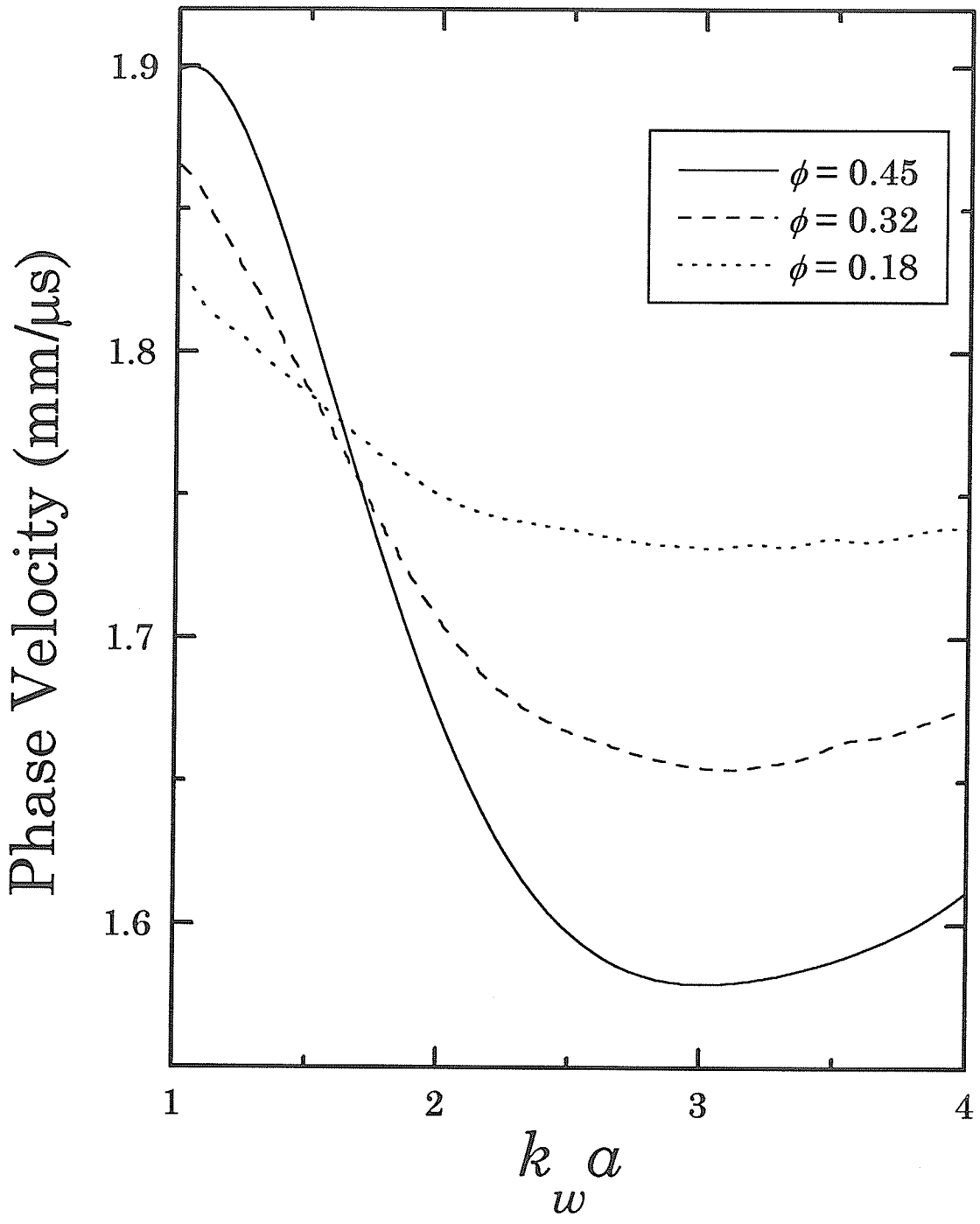

Figure. 4.49. Phase velocity for a suspension of glass beads in a mixture of 70% glycerol and 30% water for volume fractions ϕ of 0.45, 0.32 and 0.18.

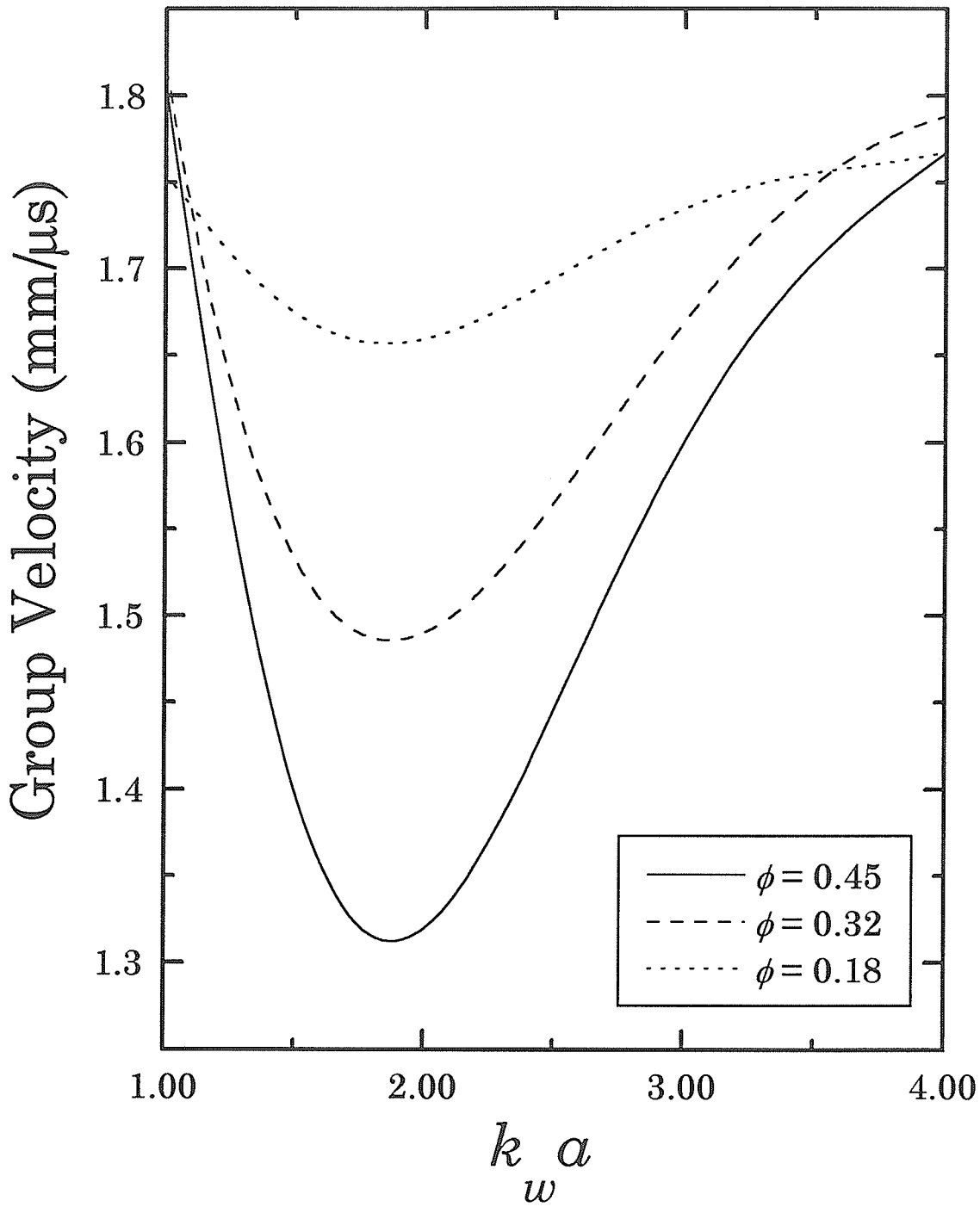

Figure 4.50. Calculations of the group velocity of a suspension of glass beads in a mixture of 70% glycerol and 30% water for volume fractions ϕ of 0.45, 0.32 and 0.18.

To obtain the diffusion coefficient, D, we fit the measured diffusive profile to theoretical expressions derived for the flux, $J(t)$, of ultrasound diffusing through a slab–like sample of scatterers. These equations were first presented in section 2.1.2, and are;

$$J(t) = \frac{e^{-r^2/4Dt}\, e^{-t/\tau_a}}{2\pi L^2 t} \sum_{n=1}^{\infty} A_n\, e^{-D\beta_n^2 t/L^2}, \tag{21}$$

with

$$A_n = \frac{\beta_n\left[\beta_n K \sin\beta_n - \cos\beta_n\right]\left[\sin(\beta_n z_0/L) + \beta_n K \cos(\beta_n z_0/L)\right]}{\beta_n^2 K^2 + 2K + 1}. \tag{22}$$

The dimensionless constant K is found from

$$K = \frac{2l^*}{3L}\frac{1+R}{1-R}. \tag{23}$$

and the values of β_n are the zeros of

$$\tan\beta = \frac{2\beta K}{\beta^2 K^2 - 1}. \tag{24}$$

We show, in Fig. 4.51, typical data for the diffusion profile for sound through the fluidized bed at a volume fraction of $\phi = 0.18$. Also on this plot is the best fit to the data, yielding a value for D of 0.63 mm^2/μs. Results for other volume fractions and water–glycerol mixtures can be found in appendix 2.

We use the determined parameters, the correlation function data, and Eq. (14) to obtain the mean square bead displacements as a function of time, $\left\langle \Delta r^2(\tau) \right\rangle$. We expect that data collected at different sampling times within a given occupied

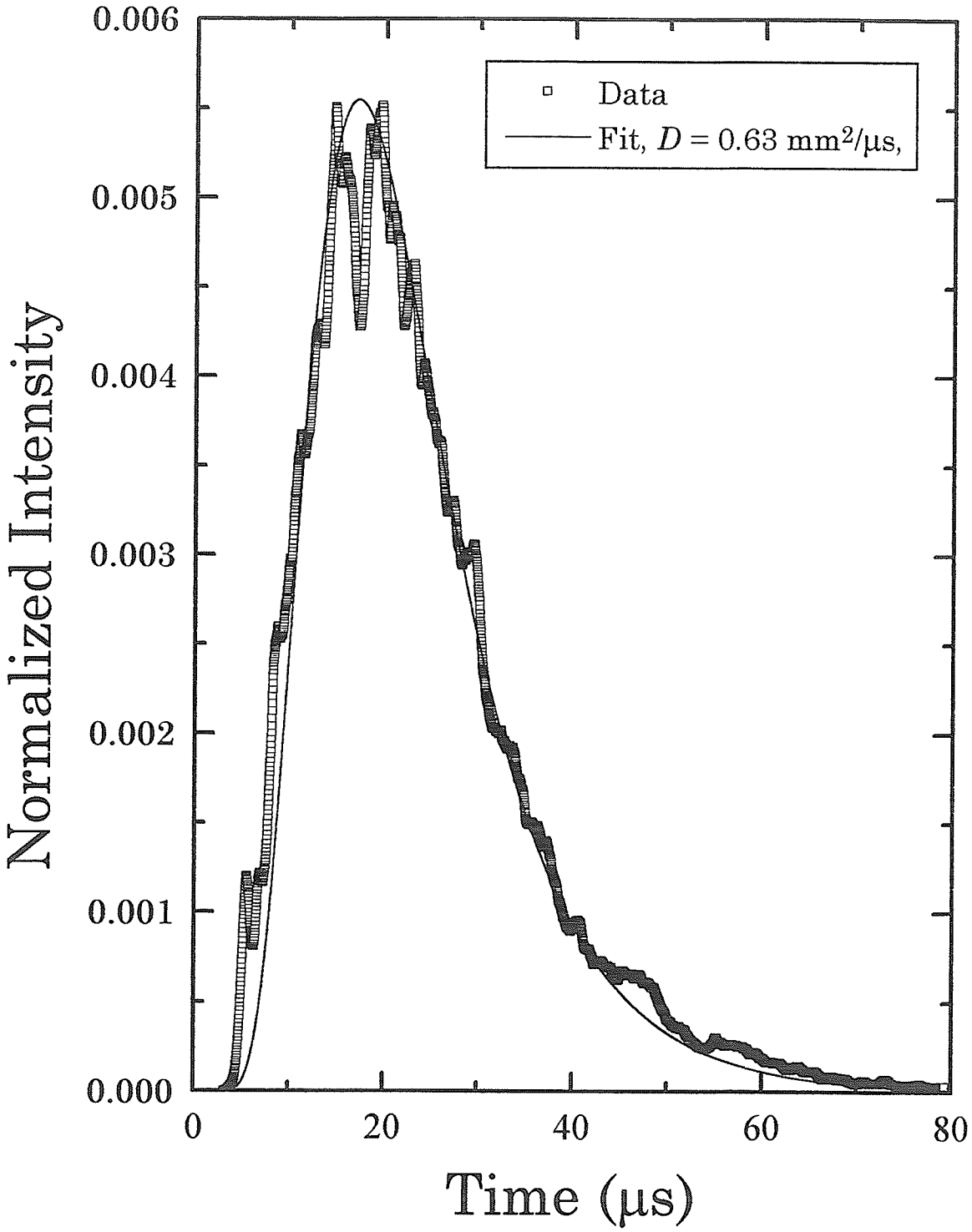

Figure 4.51. Example of data, and fit to data, used to determine the diffusion constant. $\phi = 0.18$, $\eta = 25.7$ Cp.

volume fraction will yield identical graphs of $\langle \Delta r^2(\tau) \rangle$ vs. time since the pathlength dependence seen in the correlation function (Fig. 4.41) should be removed when the particle displacements are calculated. This is verified in Fig. 4.52, where we show $\langle \Delta r^2(\tau) \rangle$ vs. time for data taken at two sampling times at the volume fraction ϕ = 0.18. We see that data measured at different sampling times give the same results for $\langle \Delta r^2(\tau) \rangle$, convincingly demonstrating that the dependence of the correlation function on pathlength is correctly derived in the model (Eq. (14)). Overlaid on the curves of Fig. 4.52 is a straight line indicating quadratic, or τ^2, behavior. We note that, at this density, the data exhibit this time dependence up to some point beyond which the data 'roll over' into background. The observed τ^2 dependence indicates that the behavior results from deterministic motion. This we attribute to convective flows in the fluidized bed. To interpret this further we determine the variance in particle velocity in a similar fashion to that of Xue *et al.* [6] where $\langle \Delta r^2(\tau) \rangle$ is given by

$$\langle \Delta r^2(\tau) \rangle = \langle \Delta V^2 \rangle \tau^2,$$

The dependence of the particle displacements on volume fraction is shown in Fig. 4.53, where we plot $\langle \Delta r^2(\tau) \rangle$ vs. time for three volume fractions. These curves were obtained from the correlation functions shown in Fig. 4.39. We find small variations between the three curves. The velocity variance is obtained by fitting a quadratic equation to these data and finding the slope of the fit that most resembles the data.

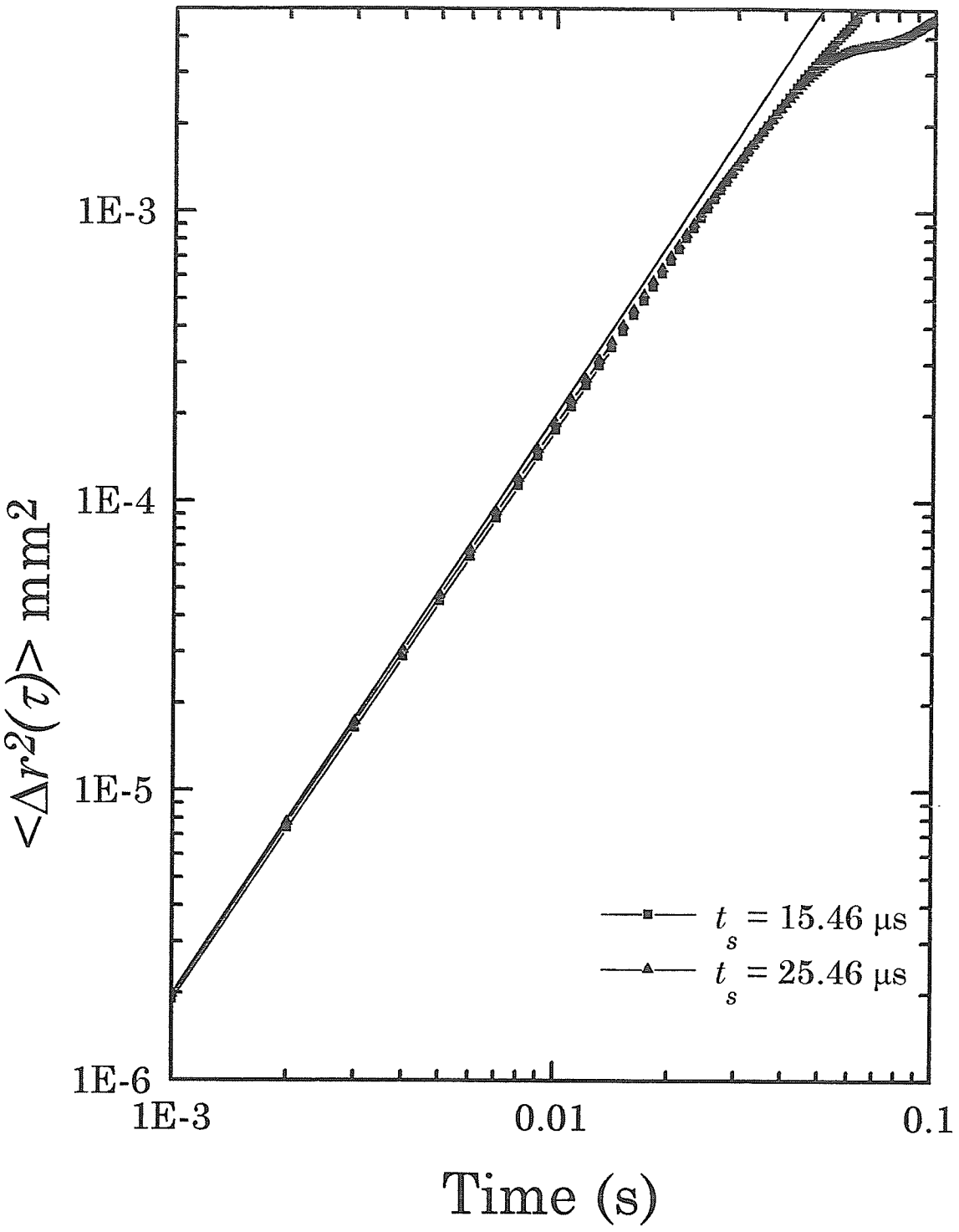

Figure 4.52. Comparison of mean square displacements at two sampling times. $\phi = 0.32$, $\eta = 25.7$ cP.

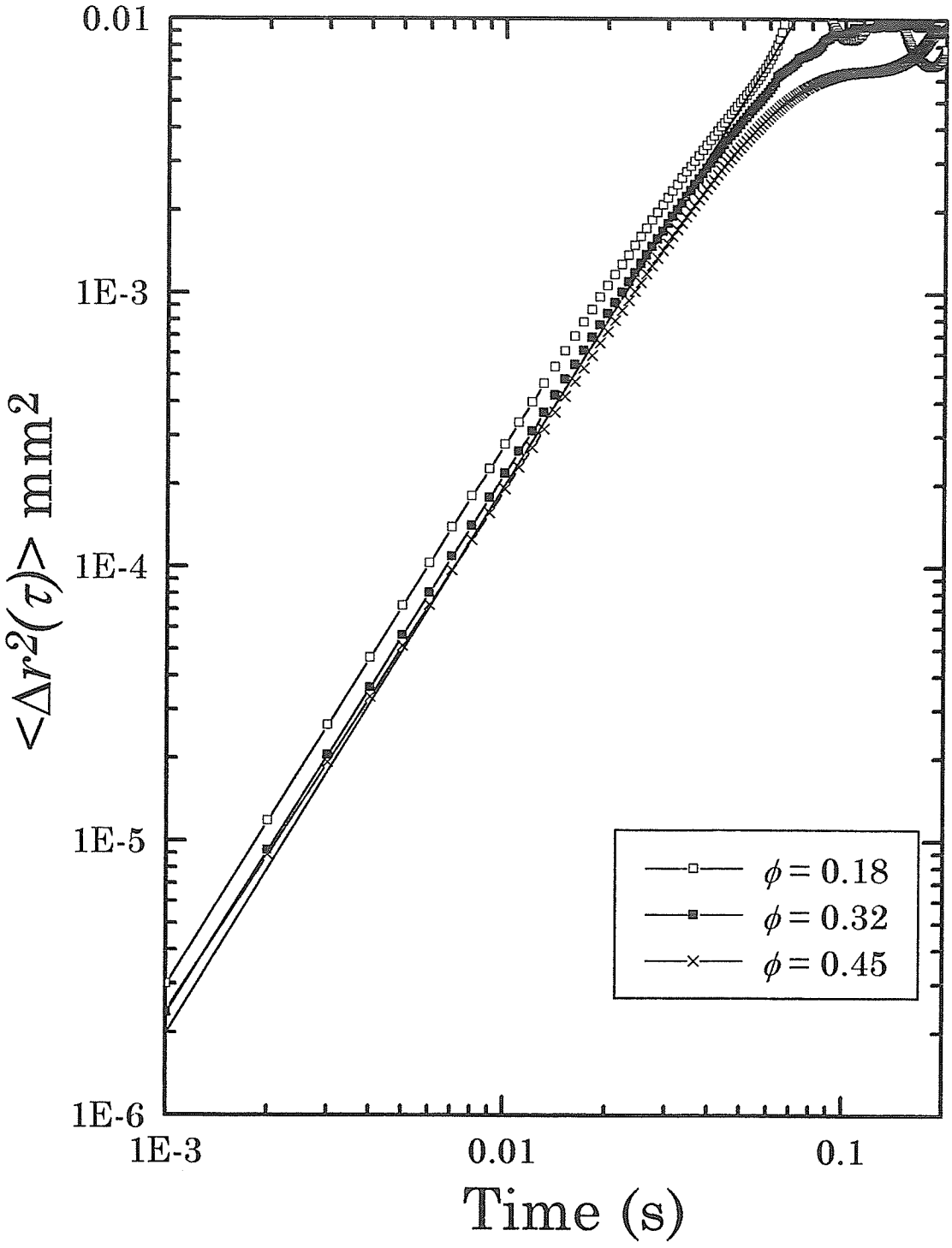

Figure 4.53. Comparison of mean square displacements at three volume fractions, and a single viscosity of $\eta = 25.7$ Cp.

In Table 1 we summarize the results for the velocity variance found in this manner, and include comparisons of this variance with the flow velocity of our medium and the calculated Stokes velocity, V_0, of the scattering particles.

ϕ	V_{flow} mm/s	$\sqrt{\langle \Delta V^2 \rangle}$ mm/s	$\sqrt{\langle \Delta V^2 \rangle}/V_0$	$\sqrt{\langle \Delta V^2 \rangle}/V_{flow}$
0.18	_	1.64	0.23	_
0.32	4.5	1.45	0.21	0.32
0.45	3.8	1.35	0.19	0.36

Table 1. Variance in velocity for a viscosity of 25.7 cP, and sedimentation velocity of 7.0 mm/s, the variance in velocity is ~1/5 the sedimentation velocity and ~1/3 the flow velocity.

There appears to be little dependence on volume fraction in both the flow velocity and the velocity variance. This raises the possibility that our distribution of beads was not as monodisperse as previously believed, or that the viscosity of the solution was changing with time as the experiment progressed. The lack of variation in the variance over the range of volume fractions studied is particularly surprising in view of the results of Xue *et al.*, who find a strong dependence on volume fraction for a suspension of smaller, 15.5 μm diameter, polystyrene spheres

The viscosity dependence of $\langle \Delta r^2(\tau) \rangle$ is shown in Fig 4.54, where we see that the bead motion is strongly influenced by the viscosity, with the least viscous solution causing the largest initial bead displacements. We have also plotted curves proportional to τ^2 in Fig. 4.54 and we see the mean square bead displacements vary

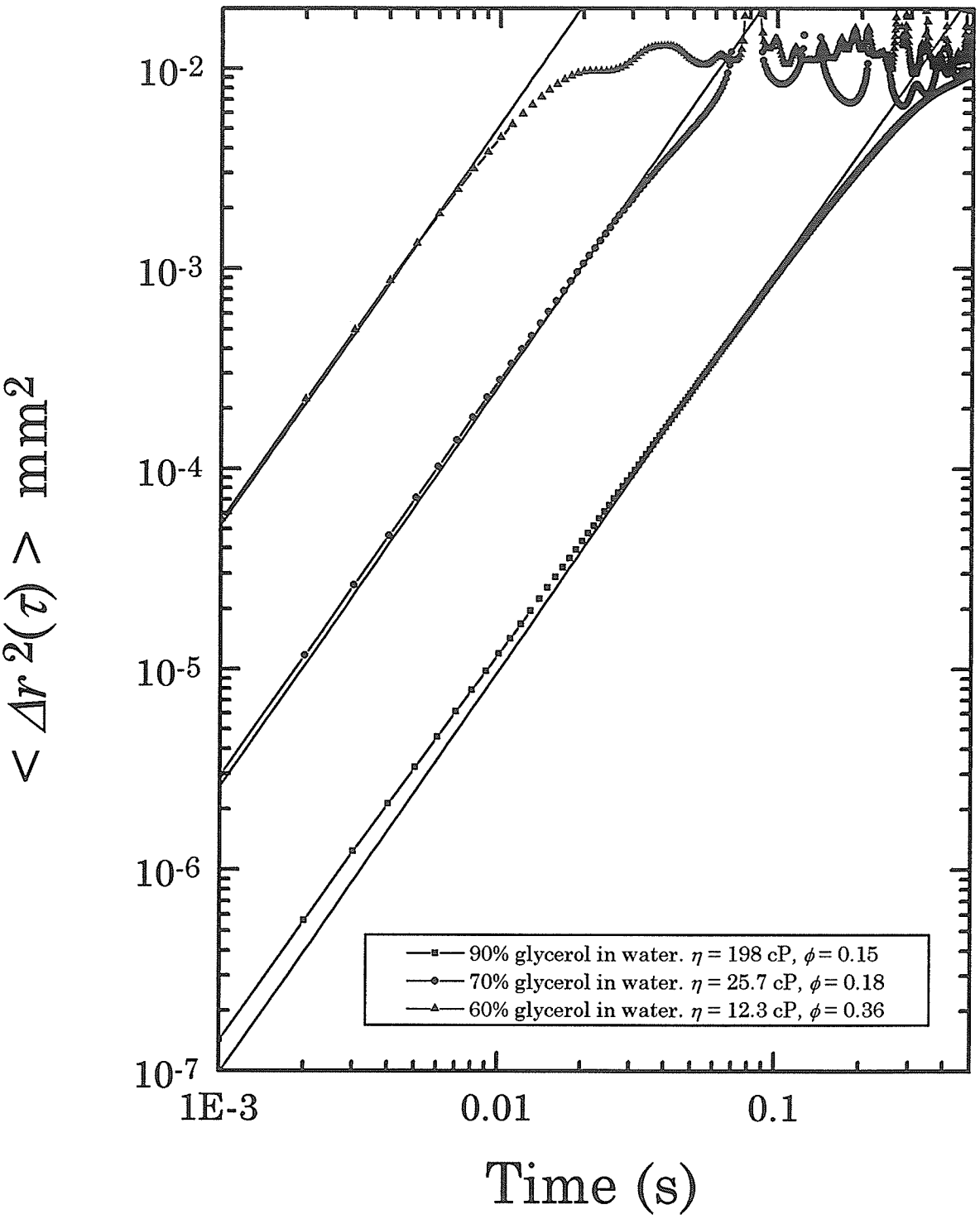

Figure 4.54. Comparison of the mean square displacement of the glass beads with different viscosity solvents.

approximately as τ^2 for all three viscosities. We have also fit these data to quadratic expressions to extract the velocity variance and in Table 2 we present these results.

η cP	$\sqrt{\langle \Delta V^2 \rangle}$ mm/s
198	0.3
25.7	1.62
12.3	7.11

Table 2. Dependence on viscosity of the velocity variance at a volume fraction of $\phi = 0.2$.

Since the fluid flow is strongly influenced by the viscosity and a higher viscosity causes slower bead dynamics, we expect all velocities to scale with η^{-1}, and in Fig. 4.55, we see that within experimental uncertainty this is indeed the case.

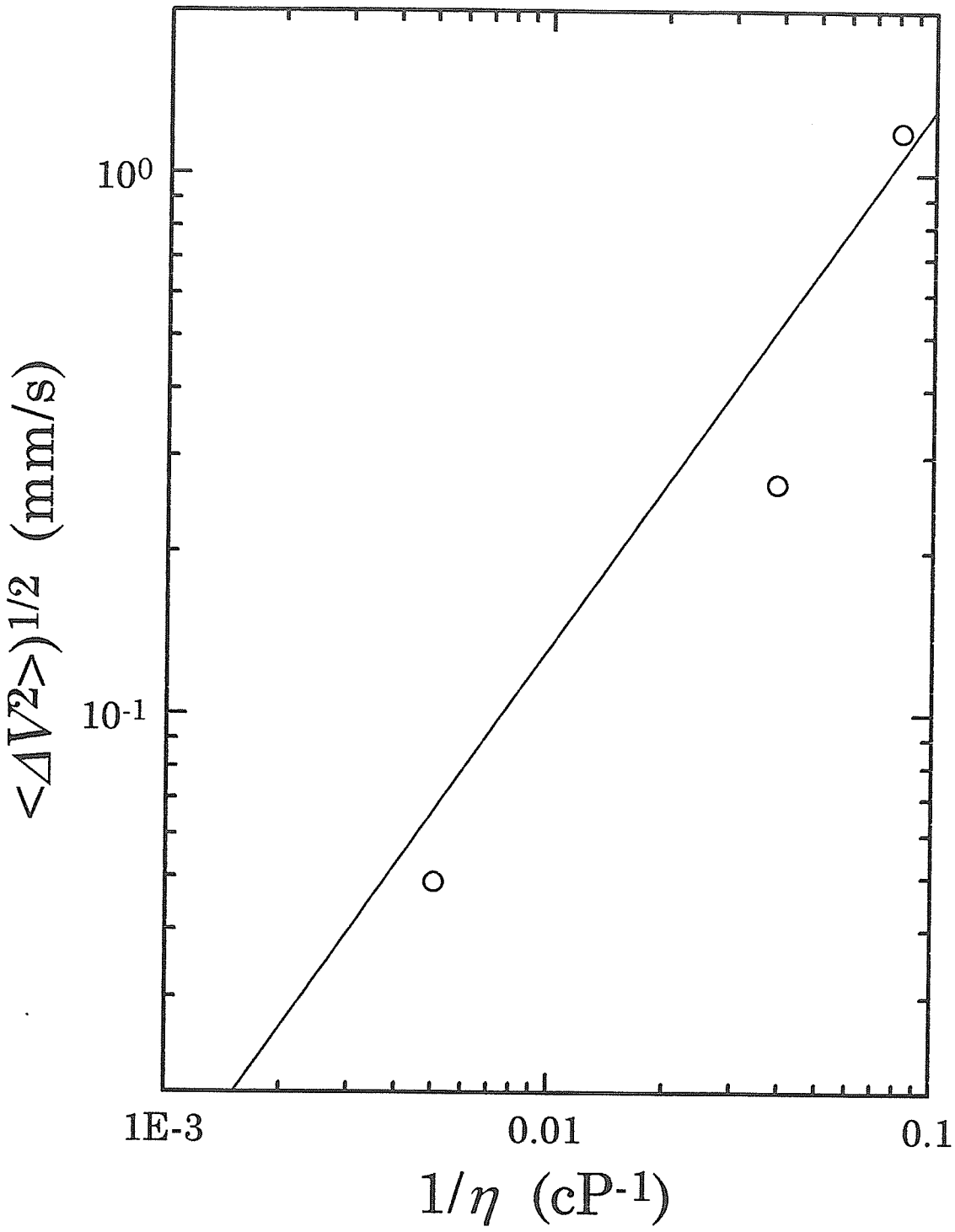

Figure 4.55. Dependence of the variance in the velocity on viscosity. The lines are straight-line fits to the data.

4.3.3 Continuous Input Wave (cw)

This method was used to investigate the possibility of measuring fast particle dynamics, meaning that we could extend the approach to low viscosity solutions. The input waveform extended over a large enough time to be considered continuous. We acquired data from a system using a solution of 80% glycerol in water and a volume fraction of beads of $\phi = 0.4$. Due to memory limitations of our oscilloscope we could only detect the scattered signal for 50,000 point record-lengths. The oscilloscope, sampled at a rate of 2.5 MS/s, so that the amount of time over which we could examine bead motion in any single record is 0.02s. We show five records of the amplitude fluctuations in Fig. 4.56, and note that there is only about one large fluctuation within each record. This means that the beads were moving too slowly to properly demonstrate this method. Nevertheless, we attempted to calculate the intensity autocorrelation function from 12 separate records, using Eq.(10). The result of this calculation, for a typical record, is shown in Fig. 4.57, where we see that the correlation function decays to below zero and then turns up dramatically. Although it is clear from the plot that the dynamics were too slow for this sample to obtain very meaningful data, this preliminary experiment does indeed demonstrate the feasibility of the technique in principal.

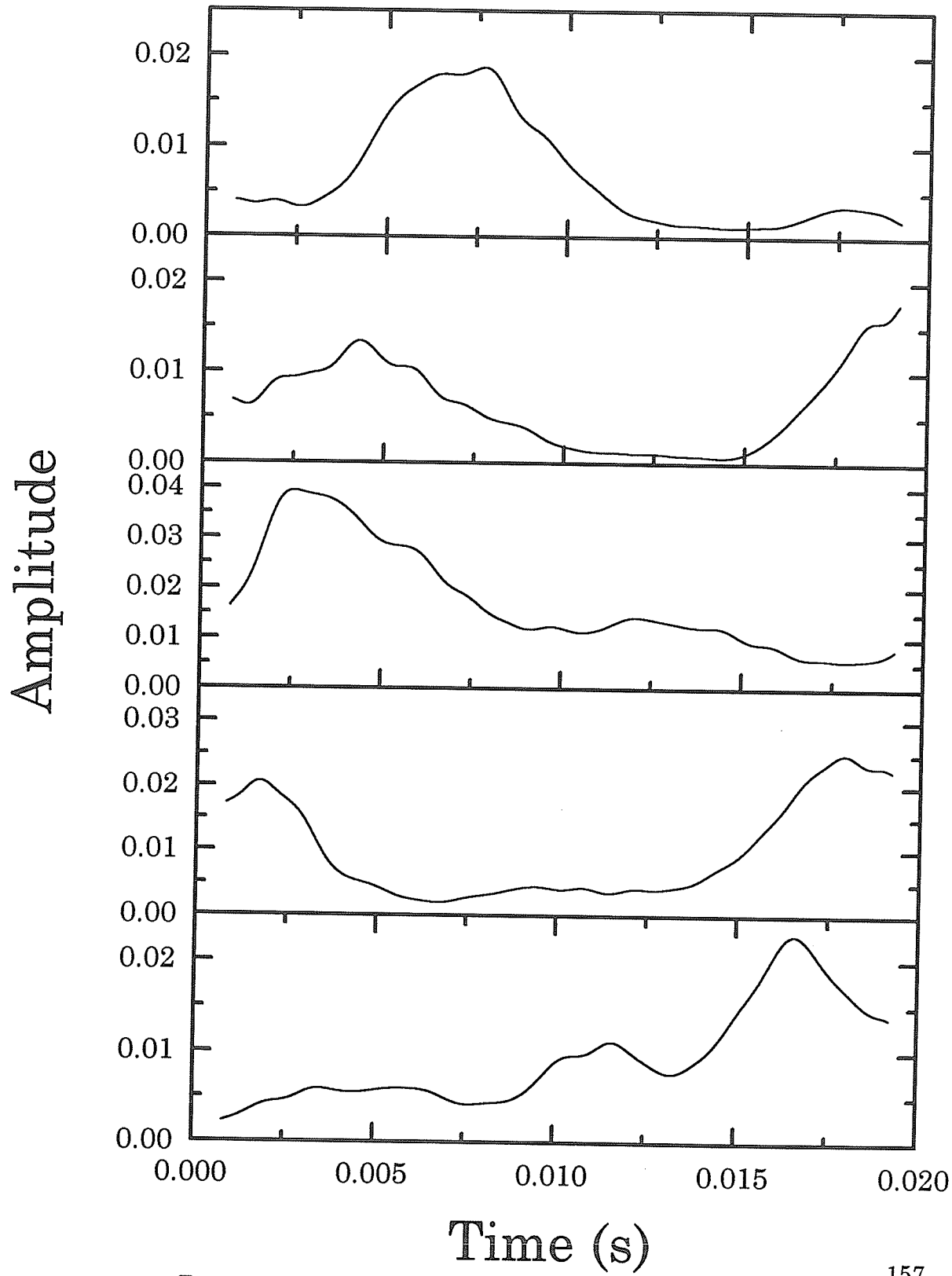

Figure 4.56. Continuous wave data. (80% glycerol in water; $\phi = 0.4$)

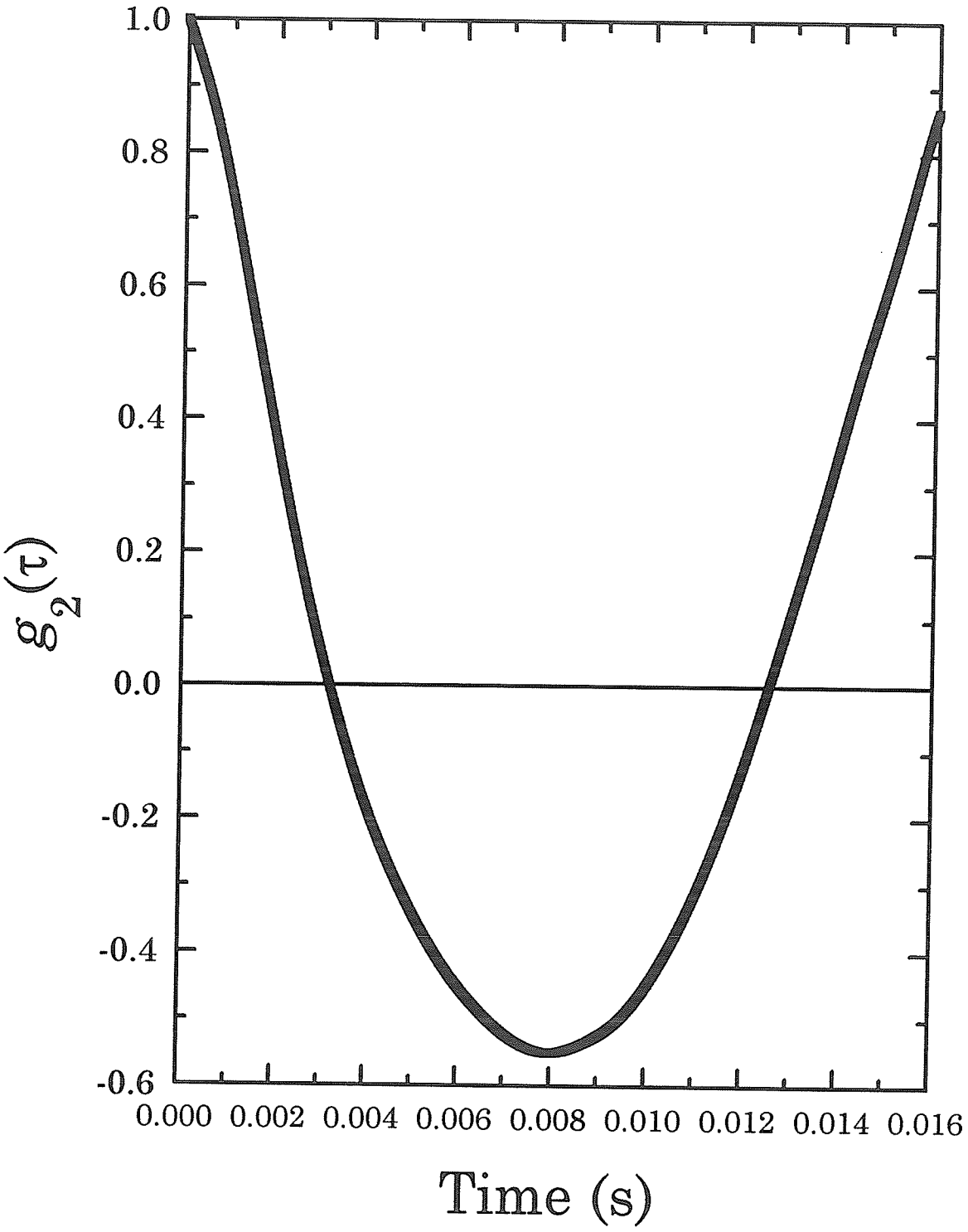

Figure 4.57. Intensity correlation function measured using continuous waves. (80% glycerol in water; $\phi = 0.4$)

4.3.4 Comparison of Acquisition Methods

A comparison of results from two acquisition methods is discussed here. We compare data acquired using the pulsed input wave (*fast–frame*) method, with data acquired using the boxcar integrator method. In both cases we used a counterflowing solution of 90% glycerol. The comparison is shown in Fig. 4.58, and we see the particle displacement curves obtained by each method are consistent with each other at larger time shifts, although there is some divergence at early times. The greater resolution available through the use of the boxcar integrator method is clearly seen in this plot.

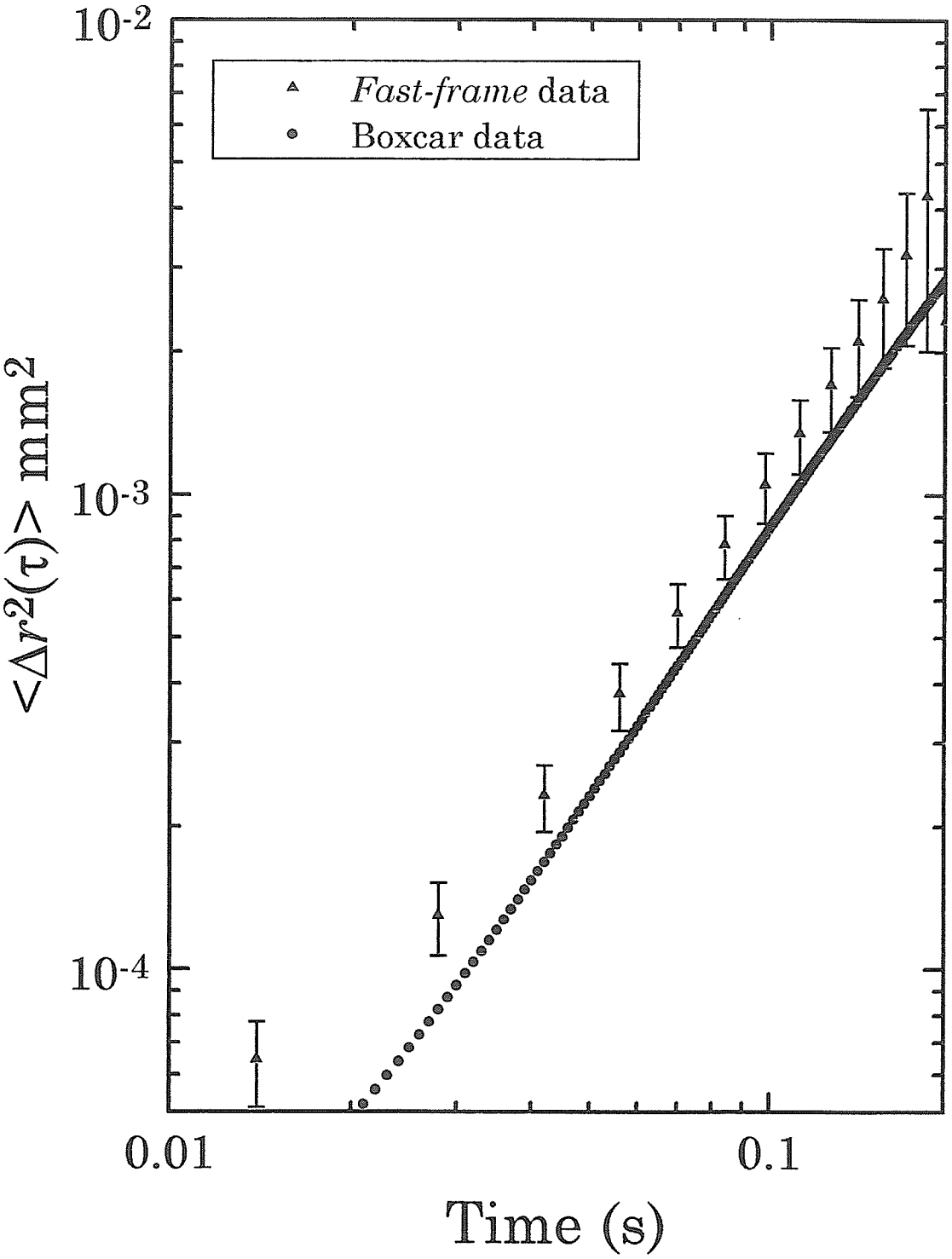

Figure 4.58. Comparison results when particle displacments are measured using different methods. $\phi = 0.11$, $\eta = 198$ cP.

4.4 References

[1] J.H. Page, P. Sheng, H.P. Schriemer, I. Jones, X. Jing, and D.A. Weitz, *Science*, **271** (1996), 634.

[2] J.H. Page, H.P. Schriemer, A.E. Bailey, and D.A. Weitz, *Phys. Rev. E* **52**, (1995), 3106.

[3] H.P. Schriemer, Ph.D. Thesis, (In preparation)

[4] H.P. Schriemer, J.H. Page, P. Sheng, X. Jing, and D.A. Weitz, *"Frequency Dependent Diffusive Transport of Acoustic Waves"* (To be published)

[5] J.X. Zhu, D.J. Pine, and D.A. Weitz, *Phys. Rev. A* **44**, (1991) 3948.

[6] X. Qui, X.L. Wu, J.Z. Xue, D.J. Pine, D.A. Weitz, and P.M. Chaikin, *Phys. Rev. Lett.* **65**, (1990), 516.

5. CONCLUSIONS

We have measured frequency, spatial and temporal correlation functions of ultrasound transmitted through multiply scattering media of glass beads immersed in a liquid. When analyzed using the diffusion approximation, each type of correlation function yields unique information about the scattering media. From frequency correlations, where we autocorrelate frequency fluctuations of the transmitted sound in a single speckle, we obtain the coefficient of diffusion for sound, D, and the absorption time τ_a. From the spatial correlation functions, measured by autocorrelating the fluctuations in transmitted sound as a function of position across the face of the samples, we obtain the speckle size of sound energy emerging from the scattering media. The temporal correlation functions, calculated by autocorrelating sound transmitted through a slurry of moving scatterers as a function of time, yields information about the dynamics of the scatterers. This information includes the mean square displacement of the scatterers as a function of time, $\left\langle \Delta r^2(\tau) \right\rangle$, and the variance in scatterer velocity, $\left\langle \Delta V^2 \right\rangle$.

5.1 Frequency Correlation Study

Frequency correlation functions of multiply scattered sound were found for plane–wave input pulses and for input pulses focused to a point on the scattering media which consisted of 1.0 mm diameter glass beads randomly close packed in water. In each case correlation functions were measured for a range of sample

thicknesses ($2.5 \leq L/l_s \leq 33$, where L is the sample thickness and l_s is the scattering mean free path), and determined over a variety of frequency ranges within the bandwidth of the input pulse.

The temporal duration of the transmitted signal is a function of sample thickness, since there are a greater number of scattering events available in a thick sample, causing more attenuation in the transmitted signal emerging from thick samples than from thin samples. Nevertheless the transmitted signals from all sample thicknesses undergo rapid fluctuations in phase and amplitude due to the interference of waves traveling different scattering paths. In samples that are thin (where the thickness, L, is not much greater than the transport mean free path, l^*) it is crucial to remove the ballistic signal (that has traversed the sample without being scattered) before calculating the correlation functions.

The transmitted signal from thick samples has more rapid frequency fluctuations, causing the correlation function to decay faster for thicker samples than for thin samples.

The correlation functions calculated for frequency ranges 1–2 MHz, 2–3 MHz, 3–4 MHz and 1.2–3.8 MHz were shown to decay more rapidly for the lower frequency range indicating a frequency dependence in the sound diffusion coefficient, D, and the absorption time τ_a.

Diffusion theory describes the data very well for all but the thinnest sample at all frequency ranges. In the thinnest sample, the pulse propagation is dominated by the ballistic component and we find that this sample thickness is below the lower

limit of applicability of the diffusion approximation. This break down between diffusion theory and experiment is shown to occur at some sharp cutoff as the sample thickness is reduced. We find this cutoff to be $L/l^* \sim 4$ for point–source and $L/l^* \sim 7$ for a plane wave input.

Diffusion theory appears to break down in the point-source geometry for a larger value of L than in the plane-wave geometry. This is because a greater distribution of paths is sampled in the plane-wave geometry than in the point-source geometry, for samples of a given thickness, so that plane waves suffer a greater number of scattering events before emerging from the sample than do waves generated by a point-source.

We conclude that the frequency correlation data are represented by diffusion theory very well as long as the sample thickness is greater than a well-defined limit. However, for our current data we find that the analysis of frequency correlation functions using the diffusion approximation is not as successful as the corresponding analysis of the intensity profile in the time domain in unambiguously determining the diffusion parameters D and τ_a.

5.2 Spatial Correlation Study

Spatial correlation functions were measured using plane–wave sound transmitted through samples of two different thickness, and for input waveforms of three different frequencies. The samples consisted of 1.0 mm diameter glass beads packed in water. The transmitted signal, as a function of position, exhibited fluctuations in amplitude and phase with the width of the amplitude fluctuations

corresponding to the size of the speckle. The phase of the speckle pattern remained roughly constant over the size of each speckle, but changed abruptly between speckles.

The correlation function was expected to decay faster with increasing frequency since a shorter wavelength of the sound had been expected to result in a smaller speckle size. This frequency dependence was observed.

We showed the speckle to have spatial extent on the order of the wavelength of the input signal. However we observed little dependence on frequency in the speckle size.

These experimental results are important for assessing the reliability of our detection technique, using a hydrophone for making absolute measurements of the transmitted intensity, where even a small variation in phase across the diameter of the hydrophone would cause the magnitude of the signal to be slightly underestimated.

Although the experiments were able to determine the speckle size reliably, the data were not sufficiently sensitive to investigate the small long-range correlation effects in speckle pattern predicted by Feng.

5.3 Temporal Correlation Study

We have demonstrated the feasibility of a new acoustic technique for measuring the dynamics of strongly scattering materials. This technique, called Diffusing Acoustic Wave Spectroscopy (DAWS), gives information about the relative motion of the scattering particles by measuring the temporal fluctuations of multiply scattered sound. Analysis of the autocorrelation function of these temporal fluctuations using the diffusion approximation enables us to obtain information about the dynamics of the scattering particles. We have developed three methods for making these measurements, allowing us to make the first acoustic measurements of the time dependence of the mean square displacements of glass beads moving in a fluidized bed. Because each particle need only move a small fraction of a wavelength for its motion to be detected, this technique allows the particle dynamics to be measured with excellent sensitivity (three orders of magnitude less than the size of the individual scattering particles).

The first and second measurement techniques use a short pulse (~4 μs) as an incident signal. These two methods allow us to take advantage of the higher power and better signal to noise characteristics of pulsed experiments. In pulsed Diffusing Acoustic Wave Spectroscopy, we measure the fluctuations at a specific time in the diffusive time profile corresponding to a specific path length by sampling the signal at consecutive repetitions of the input pulse. One advantage of this approach is that the sensitivity to the motion of the scatterers can be adjusted by selecting the path

length. A second advantage is that the analysis of the correlation function is simpler than in the more traditional continuous–wave methods.

In the first of these two methods, we measure a portion of the scattered signal after each input pulse. The temporal resolution of the method is limited by the ability of our equipment to acquire the scattered waveforms after consecutive repetitions of the input pulse, limiting the technique to relatively slow particle dynamics. (The fastest repetition rate we were able to achieve was about 10 ms.) Because this technique allows us to sample a section of the full scattered waveform we were able to measure both the phase and amplitude of the scattered signals, opening up the possibility of exploring new ways to use this phase information to achieve enhanced sensitivity in the future.

The second of the pulse methods allows us to probe much more rapid dynamics. This method uses a boxcar integrator to sample the scattered signal at a single 30 ns time interval in the diffusive time profile, which extends over several tens of microseconds. This increases the rate at which data can be acquired for successive repetitions of the input pulse, allowing us to measure temporal fluctuations of the scattered sound with a temporal resolution that approaches the limit imposed by the time taken for sound to diffuse through the sample (typically 50 to 100 μs in the current experiments).

The third method of measurement that we have developed is useful for obtaining information from systems with faster particle dynamics. The input waveform is a quasi–continuous wave (cw), having a pulse width of 200 ms which is much greater than the time taken for sound to diffuse through the sample. Because

of the motion of the scatterers the amplitude and phase of the scattered signal fluctuates in time throughout the duration of the pulse, allowing the motion of the particles to be detected on timescales approaching the ultrasonic period (typically several tenths of a microsecond).

We have used these techniques to study the dynamics of 0.5–mm–diameter glass beads in a fluidized bed where the sedimentation of the beads is countered by flowing a water/glycerol mixture vertically through the system. This system is ideal for beginning to study the hydrodynamic properties of slurries. By analyzing the measured temporal correlation functions using the diffusion approximation to account for the transport of sound through the sample, we have measured the time dependence of the mean square displacements of the beads. We find that the mean square displacement varies quadratically with time, indicating that the bead motion is not a stochastic process but results from inhomogeneous, deterministic, convective flow. The magnitude of the τ^2 contribution provides a measure of the velocity variance. We have investigated the dependence of the velocity variance on occupied volume fraction of the beads and on the viscosity of the suspending fluid. While the square root of the velocity variance depends inversely on the viscosity, as expected, we find a surprisingly weak dependence on volume fraction, motivating further research to investigate this behavior.

6. APPENDICES

6.1 Appendix 1. Extracting amplitudes and phases from transmitted fields

Consider a transmitted signal, which we represent by $S(t) = A\cos(\omega t + \phi)$. We multiply this by a sinusoidal reference signal, $R_s(t) = \sin\omega t$, where $\omega = 2\pi f$, and f is the central frequency of the original input pulse.

$$\begin{aligned} S(t)R_s(t) &= A\cos(\omega t + \phi)\sin\omega t \\ &= A[\cos\omega t\cos\phi - \sin\omega t\sin\phi]\sin\omega t \\ &= A[\cos\omega t\sin\omega t\cos\phi - \sin^2\omega t\sin\phi] \\ &= A\left[\frac{1}{2}\sin 2\omega t\cos\phi - \frac{1}{2}(1-\cos 2\omega t)\sin\phi\right] \\ &= -\frac{A}{2}\sin\phi + \frac{A}{2}\sin 2\omega t\cos\phi + \frac{A}{2}\cos 2\omega t\sin\phi \end{aligned} \tag{1}$$

Similarly, we multiply $S(t)$, by a cosine reference signal, $R_c(t)$:

$$\begin{aligned} S(t)R_c(t) &= A\cos(\omega t + \phi)\cos\omega t \\ &= A[\cos\omega t\cos\phi - \sin\omega t\sin\phi]\cos\omega t \\ &= A[\cos^2\omega t\cos\phi - \sin\omega t\cos\omega t\sin\phi] \\ &= A\left[\frac{1}{2}(\cos 2\omega t + 1)\cos\phi - \frac{1}{2}\sin 2\omega t\sin\phi\right] \\ &= \frac{A}{2}\cos\phi + \frac{A}{2}\cos 2\omega t\cos\phi - \frac{A}{2}\sin 2\omega t\sin\phi. \end{aligned} \tag{2}$$

We next digitally filter Eqs. (1) and (2), with a low pass filter to remove signals at $2\omega t$, so that the resulting signals include only the zero frequency components:

$$\begin{aligned} \text{cosine term} &= \frac{A}{2}\cos\phi \equiv C \\ \text{sine term} &= \frac{A}{2}\sin\phi \equiv S \end{aligned} \tag{3}$$

where we have used C and S to denote the cosine and sine terms. We now simply combine the two terms to extract the phase and amplitude:

$$\phi = \tan^{-1}\left(\frac{-S}{C}\right), \tag{4}$$

for the phase, and

$$\begin{aligned} C^2 + S^2 &= \frac{1}{4}A^2\left(\cos^2\phi + \sin^2\phi\right) \\ \therefore\ A &= 2\sqrt{C^2 + S^2}, \end{aligned} \tag{5}$$

for the amplitude.

6.2 Appendix 2. Summary of temporal correlation data

This table summarizes the parameters determined for use in extracting the root mean square displacements in the temporal correlation study

Glycerol %	Density of mixture g/cm^3	Flowrate cm/s	**Volume fraction (Bead density)**	Time in diffusion profile μs	**Viscosity cP.**	Velocity in mixture (cell) mm/μs	Group velocity in beads mm/μs	Phase velocity in beads mm/μs	D $mm^2/\mu s$	τ_d μs	Scaling factor $\times 10^{-3}$ mm^2
90	1.23		0.11	12.92	198	1.87	1.80	1.73	0.73	8.6	1.90
				22.92							1.07
90	1.23		0.15	13.77	198	1.88	1.53*	1.88*	0.75	7.89	3.03
				7.77							5.85
				23.77							1.91
90			0.28	13.77	198	1.88	1.34*	1.88*	0.59	6.54	3.08
70	1.18		0.18	15.46	25.7	1.81	1.64*	1.74*	0.63	26.16	1.85
				9.46			1.56				3.02
				25.46							1.12
70	1.18	.45	0.32	15.46	25.7	1.81	1.50*	1.68*	0.61	27.49	1.51
				9.46			1.64				2.47
				25.46							0.92
70	1.18	.38	0.45	15.46	25.7	1.81	1.33*	1.63*	0.48	18.05	1.76
				9.46			1..3				2.87
				25.46							1.07
60	1.16	1.05	0.36	15.46	12.3	1.74	1.38* 1.56	1.65*	0.70*	20*	1.78

* DENOTES CALCULATED VALUE

7. BIBLIOGRAPHY

H.S. Carslaw and J.C. Jaeger, *Conduction of Heat in Solids,* 2ed. Clarendon Press, Oxford, (1959), 373

J. M. Drake and A.Z. Genack, *Phys. Rev. Lett.* **55**, (1985), 2696.

S. Feng, in *Scattering and Localization of Classical Waves in Random Media,* edited by Ping Sheng. (World Scientific, Singapore, 1990).

S. Feng, C. Kane, P. Lee, and A. D. Stone, *Phys. Rev. Lett.* **61**, (1988), 834.

A.Z. Genack, in *Scattering and Localization of Classical Waves in Random Media,* edited by Ping Sheng. (World Scientific, Singapore, 1990).

J.W. Goodman, *J. Opt. Soc. Am.*, **66**, (1976), 1135.

J.W. Goodman, in *Laser Speckle and Related Phenomena,* edited by J. C. Dainty . Springer Verlag, Berlin, **9**, (1975), pp 9 –35.

A. Ishimaru, *Wave Propagation and scattering in Random Media* (Academic, New York, 1978) **V.1**.

E. Kogan, M. Kaveh, *Phys. Rev. B* **45**, (1992-II), 1049.

G. Maret and P.E. Wolf, *Z. Phys. B* **65**, (1989), 409.

J.H. Page, H.P. Schriemer, A.E. Bailey, and D.A. Weitz, *Phys. Rev. E* **52**, (1995), 3106.

J.H. Page, P. Sheng, H.P. Schriemer, I. Jones, X. Jing, and D.A. Weitz, *Science,* **271** (1996), 634.

D.J. Pine, D.A. Weitz, P.M. Chaikin, and E. Herbolzheimer, *Phys. Rev. Lett.* **60**, (1988), 1134.

D.J. Pine, D.A. Weitz, G. Maret, P.E. Wolf, E. Herbolzheimer, and P.M. Chaikin, in *Scattering and Localization of Classical Waves in Random Media,* edited by Ping Sheng. (World Scientific, Singapore, 1990).

R. Pnini and B. Shapiro, *Phys. Rev.* **B39**, (1989) 6986.

X. Qui, X.L. Wu, J.Z. Xue, D.J. Pine, D.A. Weitz, and P.M. Chaikin, *Phys. Rev. Lett.* **65**, (1990), 516.

F. Reif, *Fundamentals of Statistical and Thermal Physics.* (McGraw Hill, 1965), 486.

H.P. Schriemer, Ph.D. Thesis, (In preparation)

H.P. Schriemer, J.H. Page, P. Sheng, X. Jing, and D.A. Weitz, *"Frequency Dependent Diffusive Transport of Acoustic Waves"* (To be published)

B. Shapiro, *Phys. Rev. Lett.* **57**, (1986), 2168.

J.W. Strutt (Lord Rayleigh), *Phil. Mag.* **10**, (1880) 73.

X.L. Wu, D.J. Pine, P.M. Chaikin, J.S. Huang, and D.A. Weitz, *J. Opt. Soc. Am. B* **7** (1990), 15.

X. Zhu, D.J. Pine, and D.A. Weitz, *Phys. Rev. A* 44, (1991) 3948.

D.G. Zill, *Differential Equations with Boundary-Value Problems,* (PWS-Kent, Boston, 1989) **2**, 142.